Texture Evolution in Warm Rolled Low-Carbon Steels

By

Miguel Sánchez Araiza

A Thesis Submitted to the Faculty of Graduate Studies and Research in Partial Fulfilment of the Requirements for the Degree of Doctor of Philosophy

Department of Mining, Metals and Materials Engineering
McGill University
Montreal, Canada

August 2005

Library and
Archives Canada

Published Heritage
Branch

395 Wellington Street
Ottawa ON K1A 0N4
Canada

Bibliothèque et
Archives Canada

Direction du
Patrimoine de l'édition

395, rue Wellington
Ottawa ON K1A 0N4
Canada

Your file Votre référence
ISBN: 978-0-494-25244-4
Our file Notre référence
ISBN: 978-0-494-25244-4

NOTICE:
The author has granted a non-exclusive license allowing Library and Archives Canada to reproduce, publish, archive, preserve, conserve, communicate to the public by telecommunication or on the Internet, loan, distribute and sell theses worldwide, for commercial or non-commercial purposes, in microform, paper, electronic and/or any other formats.

The author retains copyright ownership and moral rights in this thesis. Neither the thesis nor substantial extracts from it may be printed or otherwise reproduced without the author's permission.

AVIS:
L'auteur a accordé une licence non exclusive permettant à la Bibliothèque et Archives Canada de reproduire, publier, archiver, sauvegarder, conserver, transmettre au public par télécommunication ou par l'Internet, prêter, distribuer et vendre des thèses partout dans le monde, à des fins commerciales ou autres, sur support microforme, papier, électronique et/ou autres formats.

L'auteur conserve la propriété du droit d'auteur et des droits moraux qui protège cette thèse. Ni la thèse ni des extraits substantiels de celle-ci ne doivent être imprimés ou autrement reproduits sans son autorisation.

In compliance with the Canadian Privacy Act some supporting forms may have been removed from this thesis.

While these forms may be included in the document page count, their removal does not represent any loss of content from the thesis.

Conformément à la loi canadienne sur la protection de la vie privée, quelques formulaires secondaires ont été enlevés de cette thèse.

Bien que ces formulaires aient inclus dans la pagination, il n'y aura aucun contenu manquant.

Canada

ABSTRACT

The effect of warm and cold rolling parameters on the development of annealing textures and their effects on the final formability were studied in two LC steels containing 0.8%Cr. Warm rolling temperatures between 640 and 750°C were employed, together with reductions of 65% to 80%. The effects of an additional cold rolling reduction of 40%, different initial hot band grain sizes (HBGSs) and a decrease in the heating rate during annealing were also studied. The ND fibre, <111>//ND, of the recrystallization texture was strengthened as the warm rolling temperature was decreased. A noticeable improvement in both the continuity and intensity of the ND fibre was obtained when samples were submitted to an additional 40% cold rolling reduction. The ND fibre was even more continuous and intense when a low heating rate was utilized, yielding r-values of 1.2 and 1.3 for the warm rolled and warm plus cold rolled samples, respectively. On the other hand, the volume fraction of grains containing shear bands is slightly lower for the finer HBGS. However, this does not reduce the amount of in-grain nucleation of γ grains, suggesting that shear bands are not the only factor that has to be considered in the improvement of warm rolling textures. Although the normal anisotropy is not affected by the HBGS, much lower Δr values were associated with the finer grained steel.

The texture changes taking place during recrystallization were examined using electron back-scattered diffraction. The recrystallization textures resemble the deformation textures but with a more extensive α fibre that includes the {113}<471> orientation; the gamma fibre extends to the {554}<225>. These two orientations are related to the {112}<110> deformed grains by near 26° rotations about selected <110> axes. Nevertheless, both orientations appear in the early stages of recrystallization, an observation that does not support the oriented growth theory. The {111}<hkl> orientations are the first to recrystallize while the α fibre is present until the end of recrystallization. It is finally consumed by all types of grains as well as by subgrain coalescence. The relatively constant volume fractions of the main orientations and the similarities in the growth rates for the {111}<hkl> and random orientations suggest that recrystallization is controlled by the oriented nucleation concept.

RÉSUMÉ

L'effet des conditions de laminage tiède et à froid sur le développement des textures de recuit et sur la formabilité du produit final a été étudié sur deux aciers bas carbone contenant 0.8%Cr. Des températures de laminage comprises entre 640 et 750°C ont été utilisées, ainsi que des réductions de 65% à 80%. Les effets d'un laminage à froid supplémentaire de 40%, de la taille initiale des grains de la bande à chaud (TGBC) ainsi que de la vitesse de chauffe pendant le recuit ont également été étudiés. La fibre ND de la texture de recristallisation, <111>//ND, est renforcée par une diminution de la température de laminage à chaude. Une amélioration notable de la continuité et de l'intensité de la fibre a été obtenue lorsque l'échantillon avait subi une réduction à froid additionnelle de 40%. La fibre ND était bien plus continue et intense quand une faible vitesse de chauffe était utilisée, menant à des valeurs du coefficient d'anisotrope r de 1,1 et de 1,3 pour les échantillons laminés à tiède et laminés à tiède et à froid, respectivement. D'autre part, la fraction volumique de bandes de cisaillement est légèrement inférieure pour la TGBC plus petite. Cependant, ceci ne réduit pas la quantité de nucléation intragranulaire de grains appartenant à la fibre γ, ce qui suggère que les bandes de cisaillement ne sont pas le seul facteur qui doit être pris en considération dans l'amélioration des textures obtenues par laminage a tiède. Bien que l'anisotropie normale ne soit pas affectée par la TGBC, des valeurs beaucoup plus basses de ΔR ont été obtenues avec l'acier comportant la plus petite TGBC. Les changements de texture en cours de recristallisation ont été examinés par la diffraction des électrons rétro-diffusés. Les textures de recristallisation ressemblent aux textures de déformation mais avec une fibre α plus étendue qui comprend la composante {113}<471>; la fibre gamma s'étend jusqu'à {554}<225>. Ces deux orientations sont liées aux grains déformés {112}<110> par des rotations de près de 26° autour des axes <110>. Néanmoins, ces deux orientations apparaissent dès le début de la recristallisation, une observation qui ne soutient pas la théorie de croissance orientée. Les orientations {111}<hkl> sont les premières à recristalliser tandis que la fibre α est présente jusqu'à la fin de la recristallisation. Celle-ci est finalement consommée par tous les types de grains aussi bien que par coalescence de sousgrains. La fraction volumique constante des orientations principales et les vitesses de croissance semblables des orientations {111}<hkl> et des autres orientations suggèrent que la recristallisation ait lieu selon le concept de germination orientée.

ACKNOWLEDGMENTS

This work is a humble recognition of the contributions of many persons.

My sincere thanks go to Professor J.J. Jonas, my thesis supervisor, for sharing his experience and knowledge, for his time, and for teaching me the best way through his own example.

Thanks are also due to Professor P.J. Jacques of the Université catholique de Louvain for making possible the extensive EBSD measurements that were essential for the accomplishment of this work.

I am thankful to National Council of Science and Technology of Mexico, CONACYT, for giving me the financial support to complete this project.

I am also grateful to Mr. Edwin Fernandez at McGill and Claude Galvani at CANMET for their help in the experimental parts of this work. Significant assistance was also received from Slavek Poplawski in the area of X-ray diffraction and Helen Campbell in the area of electron microscopy.

Major contributions were continuously received from my fellow researchers and graduate students in the areas of texture analysis, experimental set up, and good company. In the category of the two first are Dr. S. Godet, Dr. Y. He, Dr. R. Varano, Dr. A.O. Humphreys, Dr M. Toroghinejad, and Lan Jiang. With regard to the latter, I would like to express my appreciation to Dr. A. El-Wasri, Dr. F. Zarandi, A. Rezaian, N.R. Andrade, and H. Hong.

I express my deepest thanks to my parents Miguel and Josefina, to my wife Verónica, and to my daughters Frida and Mónica, who always gave me their love and support.

TABLE OF CONTENTS

LIST OF FIGURES

LIST OF TABLES

CHAPTER I

I INTRODUCTION

The production of steel sheets rolled at temperatures within the ferrite region (650-800°C), known as warm rolling (WR), has been studied and progressively established for nearly a decade, principally for IF steels [1-7]. Warm Rolling offers considerable cost savings since it requires lower reheat temperatures, less deformation energy and produces less scale loss and roll wear [8]. However, the results obtained on low-carbon (LC) steels have not been entirely satisfactory as these materials exhibit low mean r-values with high directional variabilities (Δr), resulting in poor formability [9, 10]. This is because at WR temperatures low carbon steels experience dynamic strain aging (DSA) due to the presence of solute carbon during the deformation process.

Additions of Ti, Nb, B or Cr have been used to reduce the detrimental effect of C for warm rolled steels. These additions modify the DSA behaviour, extending the effects of dynamic strain hardening to higher temperatures in the warm rolling range [11, 12]. However, Ti and Nb are expensive, hence Cr additions constitute a suitable option for improving the formability of LC steels at low cost. Previous investigations have been concerned with the effect of chromium for contents from 0.5 to 0.8 %wt [9, 13, 14]. These studies included elements such as boron and phosphorus or high contents of Mn additions that resulted in textures with strong <110>//RD fibres or in a weak or discontinuous <111>//ND fibre and consequently a poor level of formability.

The first aim of the present work was to improve the recrystallization texture so as to produce a material suitable for industrial applications. In order to do this, the effect of chromium addition and of an optimum amount of Mn on the annealing texture and on the final formability were investigated. On the other hand, several thermomechanical parameters influence the final formability along with the chemistry of the steel. Among these are the hot band grain size (HBGS), the deformation temperature during warm rolling and the amount of reduction. The latter in particular has an important effect on the texture of the steel sheet after cold rolling and annealing.

Thermomechanical processing of the experimental materials involved reductions of 65 to 80% and rolling temperatures between 640 and 750°C for materials with two different initial hot band grain sizes (HBGSs). Also, as the amount of deformation is very important, the effect of an additional cold rolling reduction of 40% was also examined. Finally, the effects of two heating rates of 1.5×10^{-2} $K.s^{-1}$ and 2 $K.s^{-1}$ were considered with the aim of promoting the precipitation of C and N and of coarsening these precipitates before the onset of recrystallization. In this way, the amount of dissolved C and N is reduced and the {111} recrystallization texture can in principle be improved.

The prediction of annealing textures requires a full understanding of the mechanisms of recrystallization. Several reviews have recently been published dealing with this topic [15-17]. However, full knowledge regarding the process is not yet available; in particular, there is a lack of information regarding the recrystallization of *warm rolled* steels. Therefore, the second aim of the present work was to determine the mechanisms controlling texture formation in such steels. To this end, EBSD studies were carried out at various stages of recrystallization on samples that offered the best results in terms of formability. These measurements allowed the nucleation characteristics to be determined, including the locations of the nucleation sites and the volume fractions of the nuclei belonging to the three main orientation components. These were first the ND or γ

fibre, <111>//ND, which is beneficial to the formability, second, the RD or α fibre <110>//RD, which is detrimental to the formability, and finally, all the other orientations excluding the first two, which are referred to here as the random orientations, R. The latter are either neutral or slightly harmful to the final formability, depending on the detailed distribution of the orientations that make up this component.

Two main types of models have been proposed to account for texture development during recrystallization, the 'oriented nucleation' and 'selective growth' models [18-25]. These will be considered in detail in the literature review*. As will be seen in the following sections, the two main aims of the present work were fully accomplished: i) the recrystallization textures were improved, leading to industrially acceptable r-values, and ii) the types of mechanisms controlling the formation and evolution of the texture were established.

* See also T. Senuma, H. Yada, R. Shimizu and J. Harase. Acta Metallurgica et Materialia 1990; 38:2673-2682, where there is a full discussion regarding the effects of solute C.

CHAPTER II

II LITERATURE REVIEW

II.1 Definition of Texture

In nature almost all solids, such as metals, minerals, ceramics and some plastics, are polycrystalline; i.e., they are formed of crystals or grains. Each grain can be described by a crystallographic orientation determined by how its atomic planes are positioned relative to a fixed reference. In a given polycrystalline material, most of these grains show a preferred orientation better known as the texture [26]. Texture can also be understood as the statistical distribution of the crystal orientations g.

$$f(\mathbf{g}) = \frac{\mathbf{dVg}/\mathbf{V}}{\mathbf{dg}} \qquad 1)$$

where f(g) represents the orientation distribution function (ODF) of the crystallites in the sample, **V** is the total volume of the sample and $\mathbf{dV_g}$ is the volume of crystallites having the orientation **g** within the angular element **dg**.

Texture studies are important because the properties of materials, such as Young's modulus, strength, ductility, electrical conductivity, magnetic permeability, among others, are strongly direction dependent. In the case of the plastic deformation of metals, the deformation of a crystallite is almost always accompanied by a change in its crystallographic orientation [27]. The study of the texture changes occurring during the rolling and annealing of steel sheet produces information about the deformation and recrystallization mechanisms. In addition, it is by understanding these mechanisms that the thermomechanical processing steps and chemical composition can be manipulated to improve the formability.

The drawability or formability of a sheet material is its ability to undergo a large amount of plastic flow in the sheet plane without experiencing appreciable thickness reduction. This property is represented by the mean r-value, which is also known as the Lankford parameter r_m [28], defined as:

$$r_m = \frac{(r_0 + 2r_{45} + r_{90})}{4} \qquad 2)$$

where r is the ratio of the width to the thickness strains as measured in a tensile test, and the subscripts 0, 45 and 90 refer to the angles of inclination of the longitudinal axes of the test samples with respect to the rolling direction of the sheet [29].

II.2 Texture Representation

To represent an orientation, a convenient reference system has to be selected. In the case of steel sheets, the crystal coordinate system Kc is related to the principal directions of the unit cell structure, which in this case is BCC, and the sample reference system Ks is parallel to representative axes of the sample. Fig. II.1 illustrates these coordinate systems.

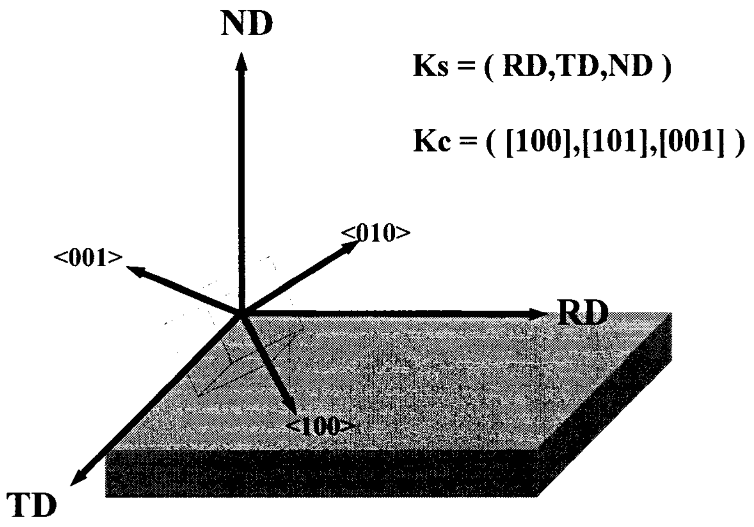

Figure II.1: Relationship between the crystal coordinate system Kc and sample coordinate system Ks.

Having determined the reference systems, the orientation of the crystal, Kc, referred to the sample coordinate system Ks, is defined as

$$\mathbf{K}_c = \mathbf{g}.\mathbf{K}_c \qquad 3)$$

where g is the orientation, represented by the orientation matrix:

$$g = \begin{bmatrix} \cos\alpha_1 & \cos\beta_2 & \cos\gamma_1 \\ \cos\alpha_2 & \cos\beta_2 & \cos\gamma_2 \\ \cos\alpha_3 & \cos\beta_3 & \cos\gamma_3 \end{bmatrix} \qquad 4)$$

and α, β and γ are the angles between the crystal and sample axes.

Orientations are traditionally represented by pole figures [30] or by the crystallite orientation distribution function (ODF) [30, 31]. However, pole figures do not provide a complete description of the texture [12] since they only represent a two-dimensional projection of a three-dimensional property. In this work, all textures will be represented on ODF's.

The ODF specifies the frequency of occurrence of particular orientations, conventionally scaled in random units, and can be conveniently represented in the three-dimensional Euler space by means of the three Euler angles, (φ_1, Φ, φ_2). The latter represent three consecutive rotations around predefined axes, which transform one reference system into another. The Euler angles of a particular set of rotations can be defined in several ways but the convention proposed by Bunge [27] is the most commonly accepted.

In Bunge's convention, the crystal coordinate system is initially aligned with the sample coordinate system. In the first step, the Kc system is rotated about the Z-axis through the angle φ_1; then it is rotated with respect to its new orientation around the new X' axis through the angle Φ; finally, it is rotated again respect to this second new orientation around the Z'-axis through the angle φ_2. The Euler angles, as they appear after the three consecutive rotations are shown in Fig. II.2.

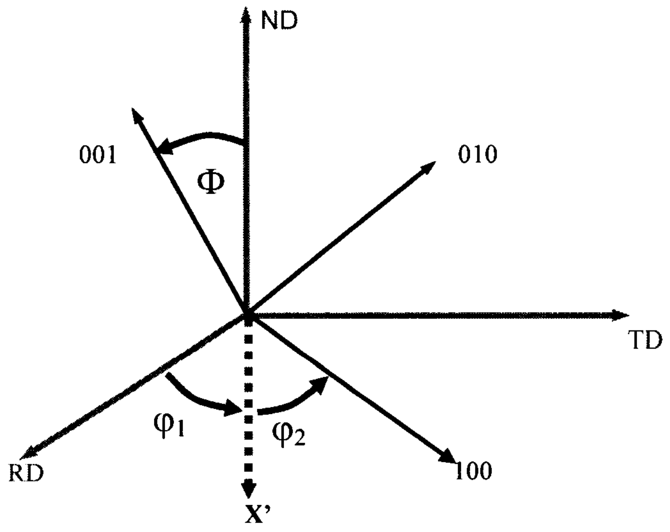

Figure II.2. Euler angles (φ_1, Φ, φ_2).

Each crystal orientation denoted by φ_1, Φ, and φ_2 can also be represented by the equivalent Miller indexes {*hkl*}<*uvw*>. These symbolize that the {*hkl*} crystallographic planes of the grain are parallel to the plane of the sheet, while its <*uvw*> crystallographic directions are parallel to the rolling direction.

Complete Euler space is defined by the intervals $0 \leq \varphi_1 \leq 2\pi$, $0 \leq \Phi \leq \pi$, and $0 \leq \varphi_2 \leq 2\pi$. However, in the case of cubic crystal symmetry, in which there are 24 symmetry elements, one 24th of the total space suffices to represent each orientation once. Nevertheless, as this subdivision does not display linear boundaries, a more convenient subspace defined by $0 \leq \varphi_1 \leq 2\pi$, $0 \leq \Phi \leq \pi/2$, $0 \leq \varphi_2 \leq \pi/2$ is generally selected. Such a subspace displays three-fold redundancy, i.e. each orientation is represented by three symmetrical points. The further consideration of sample symmetry, which is orthorhombic for rolled materials (each of the sample axes is a two-fold symmetry axis), introduces a four-fold redundancy into the former subspace. The latter defines the appropriate subspace in which the texture of cubic-orthorhombic materials can be conveniently represented. This confined to the reduced space $0 \leq \varphi_1, \Phi, \varphi_2 \leq \pi/2$ [32].

The $0 \leq \varphi_1, \Phi, \varphi_2 \leq \pi/2$ reduced space is presented in Fig. II.3, in which the locations of some important fibres and a few ideal orientations have been included. Additionally, all the important components of the rolling texture of LC steels can be found in the $\varphi_2 = 45°$ section of Euler space, which is shown in Fig. II.4. The important components of the rolling texture of LC steels are located along three orientation lines: the α or RD fibre (rolling direction || <110>), γ or ND fibre (normal direction || <111>) and ε or TD fibre (transverse direction || <110>). Furthermore, in the case of the ND fibre, there are only two different important ideal orientations {111}<110> and {111}<112>; as a result, the range $\varphi_1 = 60$ to 90° is sufficient to represent the complete γ-fibre.

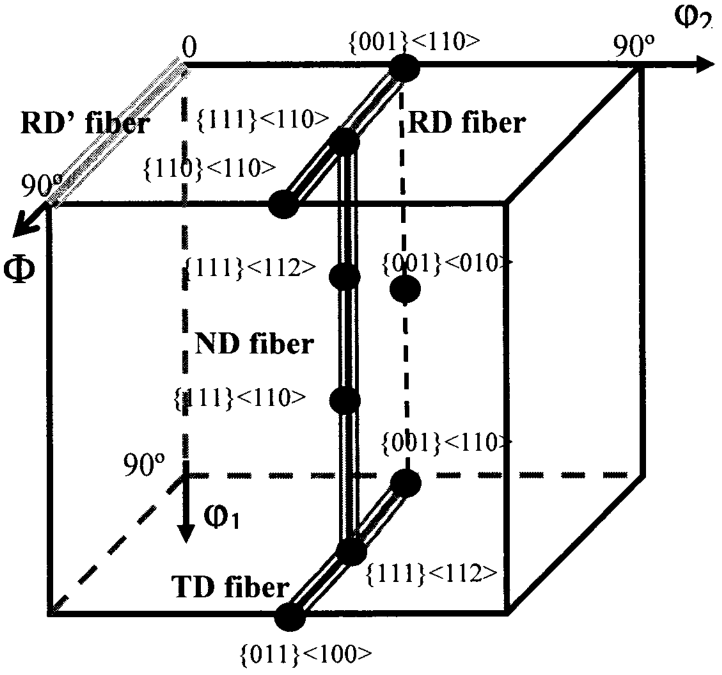

Figure II.3. Three-dimensional view of Euler space with locations of some ideal orientations and fibres.

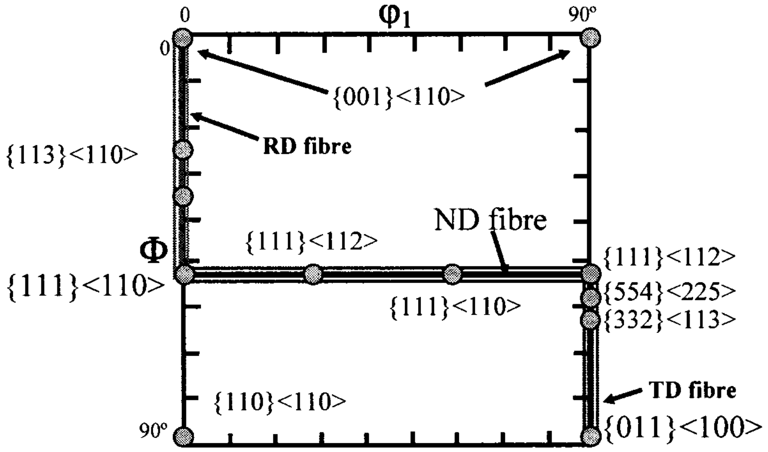

Figure II.4. ODF representation of the main steel texture components ($\varphi_2 = 45°$ ODF section)

II.3 Texture Measurement

ODF measurements rely on calculations from several pole figures determined by macrotexture methods such as X-ray and neutron diffraction. The principle of pole figure measurement by means of diffraction techniques is based on Bragg's law for the reflection of radiation, X-rays or neutrons, by the crystal lattice. Bragg's law is usually written as

$$\lambda = 2d\sin\theta_B \qquad 5)$$

where d is the distance between diffracting planes, θ_B the diffraction angle, and λ the wavelength of the X-rays. As each set of lattice planes has a different lattice spacing d, reflections from various sets of lattice planes can be distinguished by setting the detector to the corresponding angle 2θ with respect to the incident radiation [33]

II.3.1 Microtexture, a finer scale approach

Macrotexture information concerns the orientations within a given volume fraction of the sample, whereas Electron Backscattered Diffraction (EBSD) or the *microtexture* technique can be used to determine how individual grains are distributed. EBSD can be used to measure microstructural attributes, such as the misorientation between two grains and the boundary properties. It can also be used in conjunction with chemical analyses to identify unknown phases [34].

The primary output of a microtexture technique is the diffraction pattern emanating from individual crystallites. Microtexture work is principally based on the interpretation of Kikuchi patterns, although selected area diffraction and micro-Kossel techniques are also occasionally employed [26]. Kikuchi diffraction occurs both in TEM and SEM microscopes. The main differences between TEM and SEM techniques involve the accuracy of orientation determination and the spatial resolution. For the SEM, typical values are 1° and about 100nm, respectively, compared with ~0.1° and 10 nm for the TEM [35]. However, difficulties with automatic line detection and slightly more complicated indexing (due to the smaller acquisition angle and the higher indices of the diffracting planes) makes TEM less attractive.

For EBSD in the SEM, diffraction occurs from the interaction of primary backscattered electrons with lattice planes close to the specimen surface. When an electron beam enters a crystalline solid, it is diffusely scattered in all directions creating a diffraction cone, known as a Kossel cone; the latter extends about the normal to the reflecting atomic planes with a half apex angle of $90° - \theta_B$. This relation indicates that the diffracted electrons satisfy Bragg's law at every set of lattice planes.

Electron scattering occurs between lattice planes generating two cones of radiation from each family of planes. If a recording medium, such as a phosphor screen interfaced to a fast acquisition camera, is positioned so as to intercept the diffraction cones, a pair of parallel conic sections results. These are Kikuchi bands, separated from each other by a distance equal to the interplanar angle $2\theta_B$. The intersection of a pair of bands corresponds to a zone axis (pole), while the intersection of several pairs of bands denotes a major zone axis. The orientation of the pattern and hence of the volume from which it has arisen is evaluated by 'indexing', i.e. identifying the poles and bands in the pattern and calculating the relationship between these and some chosen set of reference axes [26]. Tilting the specimen by angles of typically 60-70° allows more electrons to be diffracted and to escape towards the detector. The formation of an EBSD or Kikuchi pattern is illustrated in Fig. II.5

Since the mid-1980s, the continuous development of automatic data acquisition systems such as OIM^{TM} and more recently **HKL** has led to the practical application of EBSD to obtaining statistically relevant information from bulk materials [36]. This technique has reached a high level of maturity so that it can be seen as a standard technique for material characterization [37]. The principal strength of OIM resides in its ability to provide information about the morphological aspects of the microstructure as well as of the lattice orientations [34, 38].

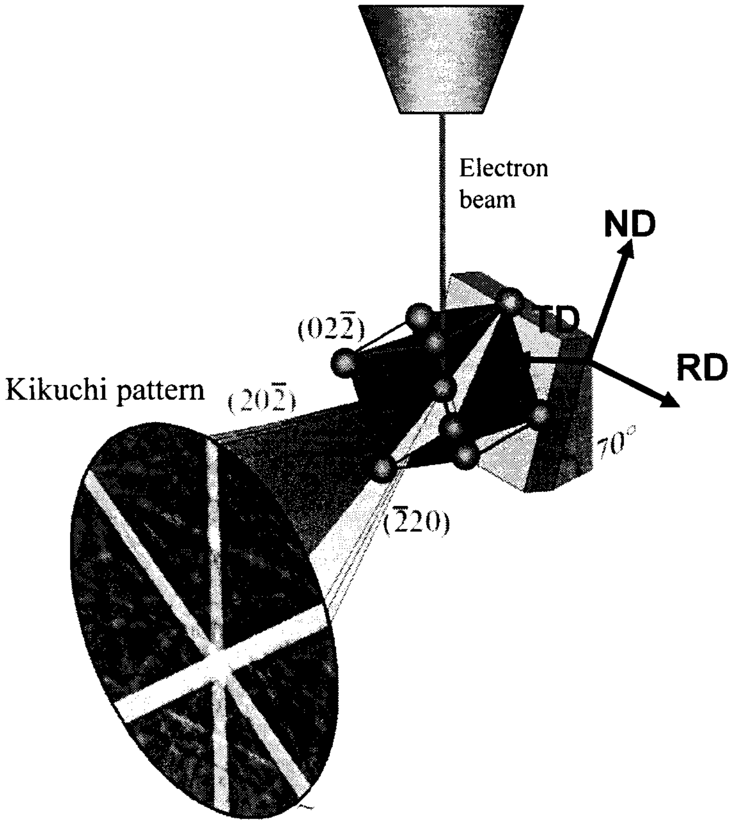

Figure II.5. Schematic representation of the formation of an EBSD pattern.

The output of an EBSD scan consists of sets of data, including the (x,y) coordinates, a phase indicator, the three Euler angles and a measure of the quality of the acquired pattern. This information is transformed into an image in which crystallographic orientations are represented according to a certain color code. Several types of maps of different attributes, such as image quality, crystallographic orientation, grain boundary misorientation, Taylor factor, and other parameters directly related to the crystallography of the sample, can be obtained. Examples of an image quality map and an orientation map of a partially recrystallized steel sample are displayed in Fig. II.6.

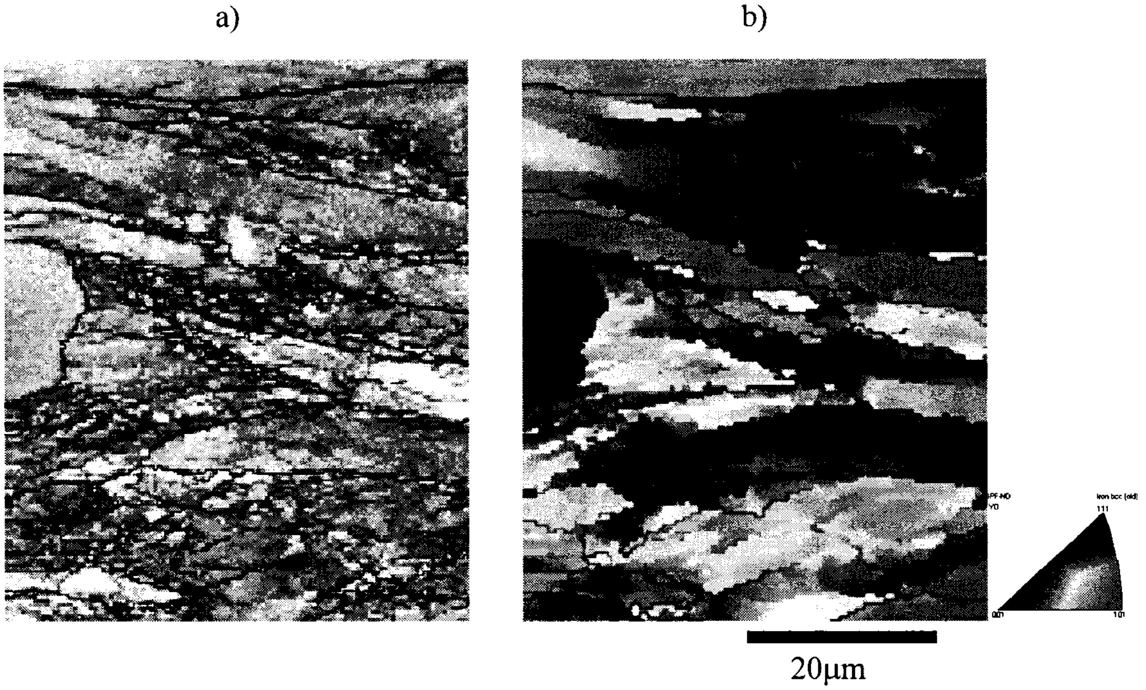

Figure II.6: Image quality map and orientation map of a partially recrystallized steel sample

II.4 Texture in the Production of Steel Sheets

Over the last 40 years extensive texture studies [4-6, 31, 39-44] have been carried out to improve the formability of the steel sheet produced by hot rolling, cold rolling and annealing.

Such production involves several texture development stages, going from deformation of the austenite to the fully recrystallized condition after cold deformation. Each previous texture influences the next one through the thermomechanical process. However, this review will focus principally on the textures resulting from hot rolling, cold rolling and recrystallization. A second classification involves the textures produced by "hot" rolling in the ferrite region, i.e. by warm rolling, as this is the main process used in the current work.

II.4.1 Hot rolling textures

The hot rolling of low carbon steels is completed while they are still in the austenite phase; nevertheless, their final condition is completely ferritic (and pearlitic). As a result, the "hot rolling" texture is formed by transformation from the austenite. During hot rolling, the parent austenite phase develops a crystallographic texture, which is later inherited by the ferrite on transformation [45]. If the austenite recrystallizes, during or after rolling, the texture will be represented principally by the rotated cube orientation {001}<110> [46]. In the opposite case when the austenite does not recrystallize, a sharp texture containing the brass {110}<112>, copper {112}<111> and S {123}<634>, together with a weaker Goss {110}<001> component will result prior to transformation [45].

The transformation textures resulting from hot rolling highly alloyed IF steels (containing 0.24%Nb or 0.30% Ti) are quite strong compared to those for low carbon steels. These textures display a <110>//RD partial fibre with maxima at {112}<110> or {001}<110>. The former originates from the copper {112}<111> whereas the latter originates from the cube {100}<001> component of the parent texture [45] [12]. A weaker component of interest is the {554}<225> or, more accurately, the {332}<113>, which results from transformation of the brass {110}<112> [45]. In the case of the IF steel considered here (0.0038%C, 0.17%Mn, 0.006%P, 0.006%S, 0.019%Nb, 0.018%Ti, 0.043Al and 0.003N), the hot rolling texture is qualitatively similar to that of low carbon steels [46]. The texture for this IF steel can be seen in Fig II.7.

II.4.2 Cold rolling textures

The textures resulting from cold rolling display a partial <110>//RD fibre and a continuous {111}//ND fibre. The transformed austenite recrystallization component, {001}<110> or rotated cube, is also contained in this texture.

Cold rolling textures are highly affected by the amount of reduction; this can be seen in the textures of an ultra low carbon steel (ULC), with deformations of 70 and 95%, illustrated in Fig. II.8. With increasing deformation, the intensity of the {111}//ND and

<110>//RD texture is gradually enhanced but its main distribution only changes slightly with the maximum for the <110>//RD fibre moving from {112}<110> to {223}<110>. This change of intensity plays a major role in determining the subsequent recrystallization texture. For deformations from 60 to 85%, the {111}//ND fibre is strengthened in the recrystallization texture and consequently the formability of the steel is improved; but for higher deformations, the result is not favourable.

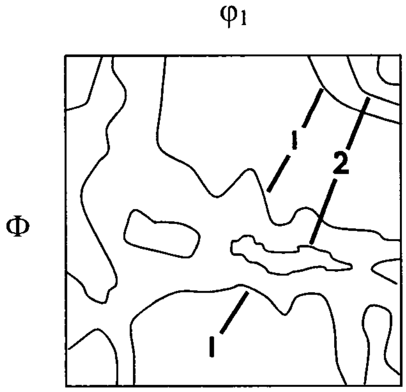

Figure II.7. ODF for IF steel austenitized at 1150°C and hot rolled to 90% reduction, at a finishing temperature of 920°C [46]. φ_2 =45° section.

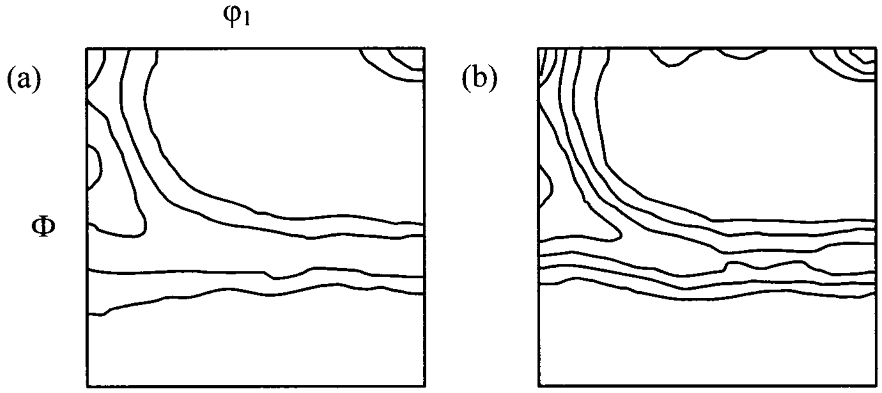

Figure II.8. Cold rolling textures after: (a) 70 and (b) 95% cold rolling reduction. Levels: 2-4-6-8-11 [47]. φ_2 =45° section.

Recently, Quadir and Duggan [23] suggested that the internal structure of {001}<110> grains remains homogeneous at reductions up to 85%, i.e. without lattice curvature, while at higher reductions, orientation splitting in the form of deformation bands occurs. This can be used to explain the optimum cold rolling reduction for good deep drawability of around 85%. At this level of reduction, no nuclei form in the α–fibre but at higher reductions, nucleation does take place and this deteriorates the final texture as far as the drawability is concerned.

Kestens and Jonas [20] have also offered an explanation in terms of the selective growth theory. They found that the RD fibre is consumed in the last stages of recrystallization by the {113}<471> and {554}<225> components in a 95% deformed ULC steel. Both orientations display the characteristic <110>26° orientation relation with respect to {112}<110>. Selective growth will be described in detail in the growth section.

The addition of alloying elements to low carbon steels seems to have little direct influence on the characteristics of the cold rolling texture. The effect of a number of alloying elements will be reviewed in further sections.

II.4.3 Warm rolling textures

Fig. II.9 illustrates the textures of an LC and an IF steel 65% deformed at room temperature and at 700°C. It is clear that the warm rolled texture resembles that of the cold rolled material. However, warm rolling textures are not only affected by the previous hot rolling texture and the amount of deformation during warm rolling, but also by the deformation temperature and the alloy content.

The effect of the deformation temperature on the volume fraction of grains containing shear bands and on the maximum texture intensity is represented in Fig. II.10 with data taken from Barnett and Jonas [48]. From this it can be seen that, for a constant reduction of 65%, the texture intensity is maintained almost constant for deformation temperatures between ambient and approximately 300°C. Above this temperature and up to the ferrite-to-austenite transformation limit, the intensity of the texture increases gradually in the low carbon steel. This has been explained in terms of the dynamic strain behaviour displayed by low carbon steels. At the lower temperatures, the strain rate sensitivity is slightly positive and favours the formation of shear bands. This causes fragmentation of the orientations in the interiors of the grains and weakens the intensity of the deformation texture. As the deformation temperature is increased, the number of shear bands is reduced drastically and the intensity of the texture is as high as 17 times random.

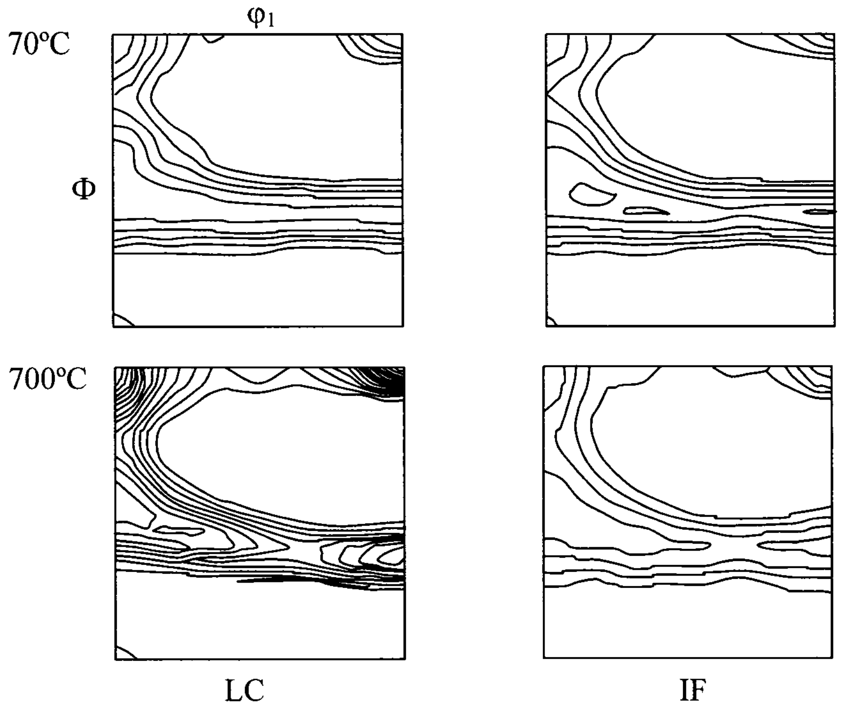

Figure II.9. ODF sections illustrating the textures of LC and IF steels rolled at 70 and 700°C (intensity levels 2,3,4....) [48]. $\varphi_2 = 45°$ ODF sections.

When stabilizing elements such as titanium and niobium are added, as in the case of the IF steels, the effect of dynamic strain aging is reduced and therefore the deformation temperature does not particularly affect the rolling texture of these steels.

In a second study, Toroghinejad et al. [49] have shown that for IF steels the intensities of orientations such as the {115}<110> and {114}<110> are reduced at a deformation temperature of 640°C and eliminated at 710°C. This splits the RD fibre in two and is an effect of the alloying additions. However, the texture intensity *increased* with the deformation temperature in this case.

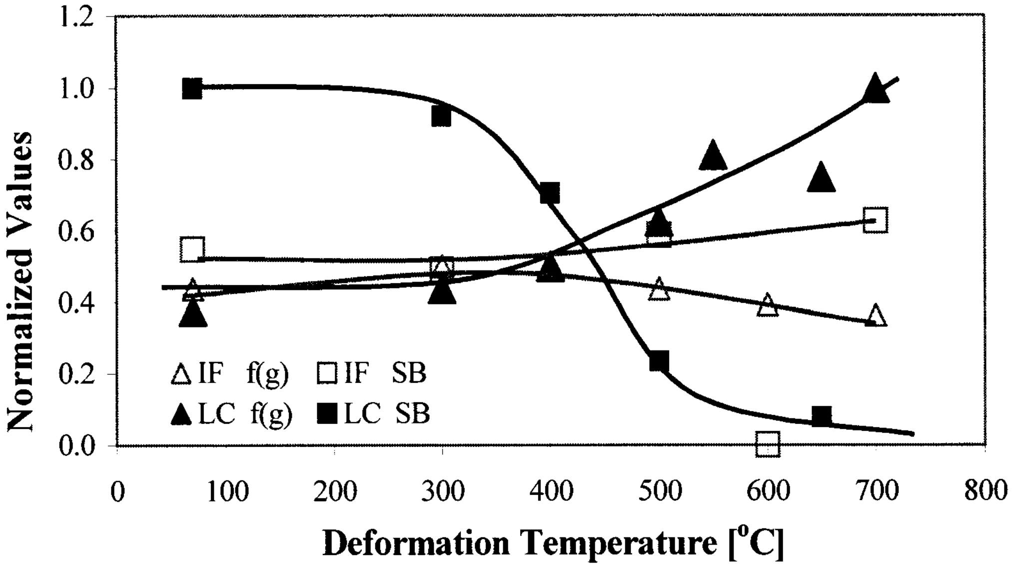

Figure II.10. Effect of deformation temperature on the normalized volume fraction of grains containing shear bands (SB) and the normalized texture intensity *f*(g) for low carbon and IF steels. [48]

II.4.4 Recrystallization textures

Recrystallization textures are the result of the complete thermomechanical process, which includes hot rolling, warm and/or cold rolling, the steel chemistry, and intermediate steps such as precipitation that may take place during coiling after hot rolling and the heating stage during annealing.

The desired recrystallization texture is that which offers the best drawability, which is characterized by a high r_m value. These values are favoured by increasing the intensity of the {111}<hkl> or ND fibre texture, while at the same time suppressing the {001}<110> component [50].

II.4.4.1 Effect of previous cold rolling

In the case of the recrystallization texture of initially cold rolled steels, the ND fibre is the dominant component and its intensity is strengthened with increasing rolling strain. Fig. II.11 illustrates that, at a rolling reduction of 65%, a nearly homogeneous intensity distribution along the ND fibre is obtained, both for LC and IF steels. However, there are some small variations, with some steels displaying a maximum at the {111}<1-10> component. When higher rolling reductions are employed, a nearly homogeneous intensity distribution along the ND fibre is obtained, which finally curves to the {554}<22-5> component at reductions of the order of 90% [12].

The differences in the final recrystallization texture, caused by differences in the level of solute carbon, have an important effect on the final r_m value; these are of the order of 2.8 for IF steels and 1.8 for LC aluminum killed steels [51]. Another consequence of this difference is that the lower the carbon content the higher the deformation needed to obtain the optimum r-value. This deformation is of the order of 85% and 90% for LC and IF steels, respectively [41].

II.4.4.2 Effect of previous warm rolling

The textures resulting from the recrystallization of warm rolled materials do not display the same similarities between LC and IF steels, as illustrated in Fig. II.11. The recrystallization texture for the LC steel is highly affected by the deformation temperature, yielding a final texture mainly composed of a strong rotated cube component and a partial RD fibre. However, it is not so much the rolling temperature that affects the recrystallization texture of low carbon steels as much as the content of carbon in solution. It is the latter that causes DSA to occur at warm rolling temperatures. In the case of the IF steels, it is the low solute carbon content and the Ti or Nb addition that eliminates the DSA. This leads to a drop in the volume fraction of grains containing shear bands, which in turn has a direct effect on the intensity of the prior deformation texture. Furthermore, the higher carbon content of the LC steel has a further detrimental effect during annealing; this will be reviewed in the section on carbon and nitrogen.

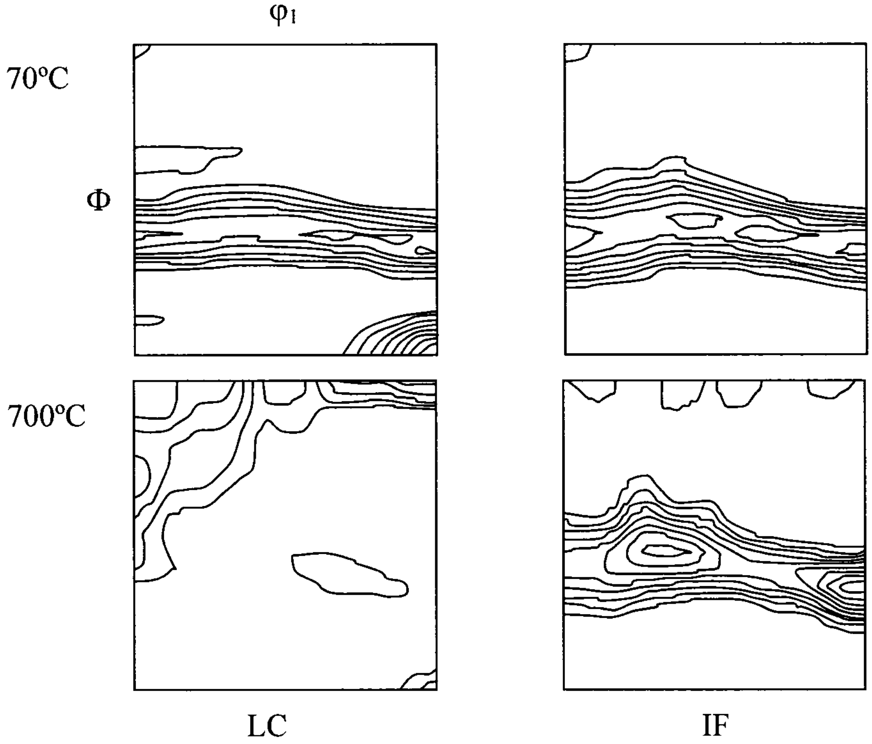

Figure II.11. Textures of LC and IF steels rolled at 70 and 700°C and annealed at 700°C (intensity levels 2,3,4….) [52]. $\varphi_2 = 45°$ ODF sections.

II.5 Recrystallization

Recrystallization is the formation of new grains in a deformed material by the formation and migration of high angle boundaries driven by differences in the stored energy of deformation. High angle boundaries are those with misorientations greater than 10–15° [15]. During thermomechanical processing, the deformation energy is stored in the material mainly in the form of dislocations. This energy is released by means of three main processes, those of recovery, recrystallization, and grain coarsening.

Recovery is a relatively homogeneous process in which the rearrangement and annihilation of dislocations occurs in the deformed material, without the migration of a high angle grain boundary.

During **recrystallization**, a further restoration process occurs in which new dislocation-free grains are formed within the recovered structure. These then grow and consume old grains, resulting in a new structure with a low dislocation density [53].

Finally, **grain coarsening** can be defined as the growth of the recrystallized grains by migration of the boundaries. These are thermodynamically unstable and their surface energy per unit volume is reduced so as to lower the stored energy.

II.6 Nucleation

In the case of recrystallization, a nucleus is considered to be a strain-free region, surrounded totally or in part by a high angle boundary. In contrast to other structural transformations, such as solidification, new grains do not 'nucleate' during recrystallization by the thermal fluctuation of atoms; instead, they grow from recovered subgrains or cells that are already present in the deformed microstructure [15].

Successful subgrains must have a stored energy appreciably lower than that of the surrounding material. They must also be of a size such that an increase in volume lowers the overall energy. Additionally, a high misorientation angle with respect to the adjacent deformed material is necessary to provide enough mobility for them to evolve into new recrystallized grains [54].

Four main forms of nucleation have been identified: high stored energy, low stored energy, shear band, and particle stimulated nucleation [4, 12, 55-57]. The textures that arise from three of these mechanisms are summarized in Fig. II.12. However, there are in a sense only *two* main forms of nucleation, as both shear band and particle stimulated nucleation are indeed also high stored energy forms. Both high and low stored energy nucleation involve orientation selection during the nucleation stage of recrystallization [15]. The first appears to operate via a subgrain growth or coalescence mechanism that is favoured in the vicinity of dense dislocation sites; it is often observed in grains of specific orientations (e.g. the {110} or {111} components) or near grain boundaries, shear bands or particles [22]. High stored energy nucleation generally leads to the development of {111} oriented nuclei. On the other hand, low rolling reductions are at the origin of low stored energy nucleation, which in steel favours the appearance of {001} oriented grains or other α–fibre nuclei [19, 58].

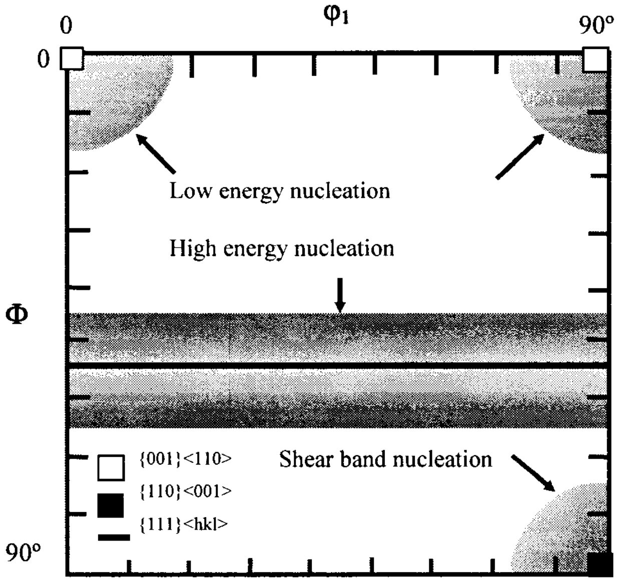

Figure II.12. Grain orientations resulting from the operation of three different nucleation mechanisms. [55]

II.6.1 High stored energy nucleation

High stored energy nucleation occurs in highly heterogeneous regions, where the deformation energy is well above average. The stored energy of deformation increases in the sequence {001}<{112}<{111}<{110} [59], which as can be seen in Fig. II.13 also applies to the order of increase in the Taylor factor. On this basis, it can be expected that the final recrystallization texture resulting from this mechanism will consist largely of the

{111}<hkl> components (and a spread of random orientations), together with a small {110} component [41, 60].

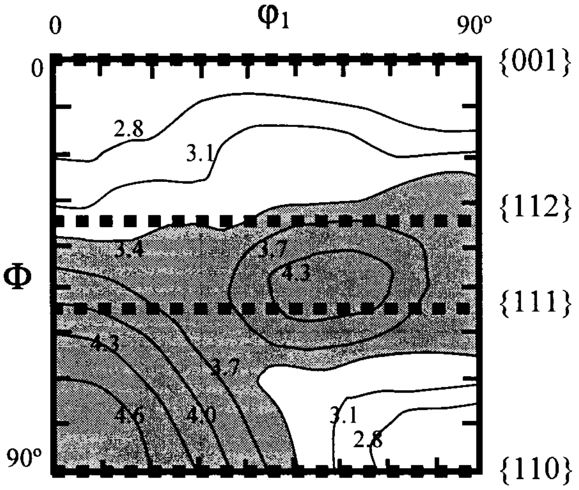

Figure II.13: Taylor factor distribution in the $\varphi_2 = 45$ deg section of Euler space. The shaded region represents the domain in which the Taylor factor exceeds a critical threshold of 3.4. Adapted from Ref. [61].

II.6.2 Shear band nucleation

The types of nuclei that can be formed in a shear band depend strongly on the orientation, shape and intensity of such bands. Shear bands formed in {111}<112> grains have often been observed to give rise to Goss nuclei, but also to near-ND fibre orientations, depending on the conditions under which the shear band is formed [4, 42, 57, 62]. Long shear bands of moderate intensity serve as sites for nucleation of the <111>//ND fibre [14], while intense shear bands contribute to the development of the {110}<001> orientations or Goss component [4, 63, 64]. Coincidently, the second type of shear band forms in initially coarse-grained hot bands.

Shear bands have been shown to cause fragmentation of the warm rolled microstructure promoting an increase in the spread of misorientations [65] and weakening the deformation texture. These features impact on the nucleation of recrystallization, enhancing nucleation at sites situated both within the grain interiors and at grain boundaries.

II.6.3 Particle stimulated nucleation

It is generally accepted that particle stimulated nucleation weakens the recrystallization texture by promoting random nucleation [53]; this will lead to an increase in the number of random components present in the final texture. Because of the irregular shapes of these particles, the deformation modes in their vicinities are rather undefined. Given that these particles are "randomly" distributed in grains of all orientations, their sizes play important roles with regard to their contributions to the overall texture. Recently, studies have shown that carbide particles with diameters of the order of 0.3 μm can act as successful nucleation sites [66].

II.6.4 Low stored energy nucleation

This nucleation type is commonly associated with the strain-induced boundary migration (SIBM) mechanism [67, 68]. SIBM involves the bulging of part of a pre-existing grain boundary, leaving a dislocation-free region behind the migrating boundary, as shown schematically in Fig. II.14. The characteristic feature of this mechanism is that the new grains have orientations similar to those of the old grains from which they have grown [53].

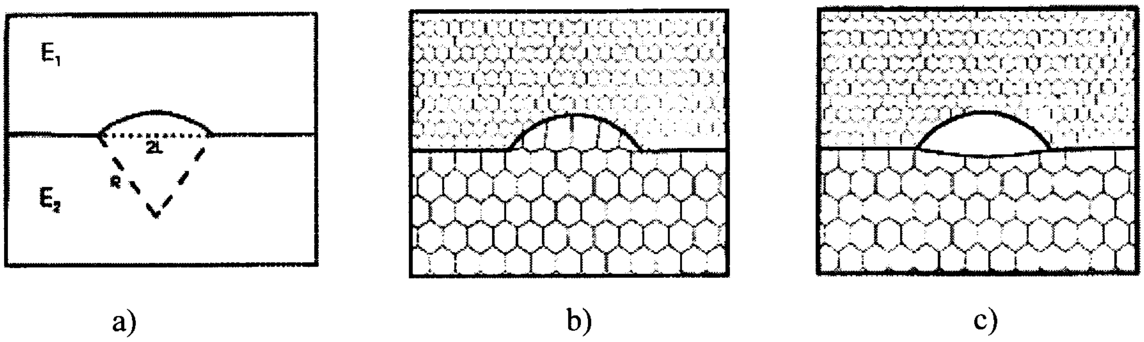

a) b) c)

Figure II.14. (a) SIBM of a boundary separating a grain of low stored energy (E_2) from one of higher energy (E_1). (b) Dragging of the dislocation structure behind the migrating boundary. (c) The migrating boundary is free of the dislocation structure [53].

The driving force for SIBM is presumed to arise from the difference in dislocation density on opposite sides of the grain boundary [15]. This recrystallization mechanism is of prime importance after low rolling reductions [58] or after conventional rolling strains at elevated temperatures [69]. In contrast to the characteristics of high stored energy nucleation, low Taylor factor orientations are favoured by the low stored energy mechanism. Examples are the cube fibre and the Goss orientation, which have been observed to appear after the annealing of temper-rolled non-oriented electrical steels [70]

II.7 Growth

After nucleation, the new grain grows into the surrounding material removing the stored dislocations and increasing the amount of relatively strain-free material. The growth velocity v at which the boundary moves depends on the mobility of the boundary M and the net pressure on the boundary P. The relation between these parameters is given as:

$$v = \mathrm{M.P} \qquad 6)$$

Recrystallization textures can either be growth or nucleation controlled [18-25], depending on the thermomechanical process employed. The selective growth effect is greatly enhanced by the presence of sharp deformation textures (> 90% reduction) or by cross rolling [58]. This type of deformation texture strongly diminishes the effect of oriented nucleation through the mechanism of orientation pinning [18], which leads to the reduced availability of sufficiently mobile recrystallization nuclei. Furthermore, a sharp deformation texture (e.g. the {112}<110>) provides a very strong filter, which will only allow a limited number of nuclei to grow, i.e. the ones that display the ideal misorientation with respect to the texture of the deformed matrix.

Oriented nucleation, on the other hand, is the controlling orientation selection process for rolling reductions of about 70%, since the resulting recrystallization texture resembles the early nucleation texture; this consists of a nearly homogeneous ND fibre [47]. Oriented nucleation is the model according to which grains of particular orientations nucleate more frequently than grains of other orientations. Such grains maintain their initial number advantage in the final recrystallization texture. By contrast, oriented growth considers that nuclei possessing certain misorientation relations with respect to the surrounding matrix will grow faster than other grains and hence dictate the final recrystallization texture. The occurrence of one or the other of these mechanisms depends on the intensity and distribution of the deformation texture and on the microstructure.

In most cold rolled steels, the resemblance between the early texture of the recrystallized grains and the final recrystallization texture [12, 51] supports the occurrence of oriented nucleation. This can be explained in terms of stored energy considerations. The stored energy of deformation increases in the sequence {001}<{112}<{111}<{110} [41, 59, 60]. Then, if the deformation texture is mainly represented by the RD and ND fibres, the recrystallization texture will be expected to display these two components. However, as the {111} orientations have a nucleation advantage, the final recrystallization texture will be represented principally by the ND fibre and, as mentioned before, by a spread of random orientations, together with a small {110} component [41, 60].

Selective growth has been reported to take place during the late stages of recrystallization in a heavily deformed ULC steel (95%CR). [19, 47]. Kestens and co-workers attributed the occurrence of selective growth to the increase in RD fibre intensity after 95% cold rolling, illustrated in Fig. II.8, which is consumed in the very last stages of recrystallization by the {113}<471> and {554}<225> components. Both orientations display the characteristic <110>26° orientation relation with respect to the {112}<110> component of the α-fibre. Selective growth has also been reported to occur when small rolling strains are applied. In this case, it was demonstrated that the mobility of interfaces characterised by <110>26.5° misorientations was greatly enhanced in a ULC steel 4.5% deformed along various directions [18]. Similar results have been observed in experiments carried out on lightly deformed single crystals, in which many new grains are produced by localized deformation and the new grains compete with each other by growth. In this case, any small growth advantage of a particular boundary will lead to the dominance of one orientation [15].

There are other selective growth theories in which the driving force is considered to depend either on the local misorientation between the nucleus and the deformed grain [71, 72], or on the orientation [73]. The former considers that the most important driving force for recrystallization is the stored energy due to the dislocations whose arrangement is dependent on the deformation texture; this in turn gives rise to the absolute maximum principal stress direction. Then, the fastest growing nuclei are those with their directions of minimum Young's modulus aligned with the direction of maximum principal stress in the deformed grain.

The second theory considers that the driving force is provided by the grain boundary energy, i.e. the energy of the interface itself. As a result, this theory applies equally to normal and abnormal grain growth. The high energy boundary has more structural defects and these are often linked to a high grain boundary migration rate and a high grain boundary diffusion rate.

Because these high energy boundaries will be removed preferentially from the microstructure, this leads to a pronounced selective growth effect. This phenomenon is associated with the development of the Goss component during the secondary recrystallization of electrical steels [74].

The model based on the minimum Young's modulus direction has been used to explain the formation of the <100> recrystallization texture from axisymmetrically deformed fcc metals, that of the cube recrystallization texture from cold rolled fcc metals, the {111}<112> recrystallization texture from cold rolled bcc iron alloys, and various recrystallization textures from axisymmetrically deformed bcc metals [75, 76].

II.8 Warm Rolling

In the case of warm rolling, some preliminary studies were carried out long ago [77-79], but it was not until the early 90's that steelmakers begun to take a detailed interest in this process. In this way, the broad outlines have been progressively established, principally for IF steels [1-3, 5]. However, as vacuum degassing is required, together with the addition of titanium or niobium, the production of IF steels is relatively expensive. It seems then that the warm rolling of low carbon steels could represent an attractive alternative. Unfortunately, the results obtained on these steels have been largely unsatisfactory, as the product is not appropriate for deep drawing purposes.

As mentioned above, good formability is represented by high values of r_m, which in turn are associated with the development of a strong {111} texture [12]. Low carbon steels possess low mean r-values, resulting in poor formability [9, 10]. This limitation represents the motivation for this work, which is intended to improve the formability of low carbon steels and to increase our understanding of the mechanisms of texture evolution during recrystallization.

II.8.1 Dynamic strain aging

At warm rolling temperatures, low carbon steels are predisposed to dynamic strain aging (DSA) due to the presence of solute carbon during the deformation process; this results in a weak {111} texture [39]. DSA is caused by the diffusion of carbon and nitrogen atoms at a rate faster than the speed of the dislocations so as to lock them. It then becomes necessary to increase the load to tear the dislocations away from the solute atoms [80]. As shown in Fig. II.15, DSA has a great impact on the strain rate sensitivity (m), resulting in negative values at low temperatures and high rate sensitivities at higher temperatures [81]. The strain rate sensitivity is defined as the change in stress required to produce a certain change in strain rate at a constant temperature.

$$m = \left. \frac{\Delta \ \mathbf{ln}(\ \sigma\ )}{\Delta \ \mathbf{ln}(\ \dot{\varepsilon}\ )} \right|_T \qquad 7)$$

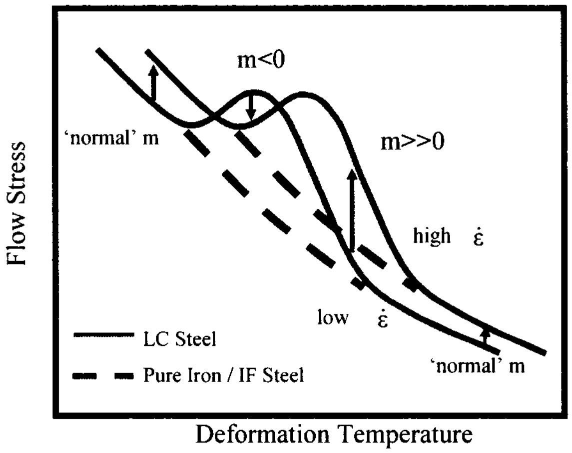

Figure II.15. The effect of DSA on the rate sensitivity, m. [81]

Negative or small positive values of strain rate sensitivity promote the formation of shear bands, which in turn have been related to the nucleation of new {111}<hkl> oriented grains, also known as the γ-fibre. Conversely, high rate sensitivities reduce the number of shear bands within the grains, allowing the development of unfavourable components, such as grains having their <110> directions parallel to the rolling direction, also known as the α–fibre [57, 65, 82, 83].

The inconvenience represented by dynamic strain aging can be eliminated by using an interstitial free steel. However, the vacuum degassing operation and the addition of titanium or niobium involved in this process makes this a fairly expensive alternative. A second option was proposed by Barnett [11] after his review of the careful work carried out by Glen [84] on the effect of various alloying elements on the flow stress of steel. This involved the addition of chromium. Further information and analysis about the effect of chromium additions will be considered in section 2.7.2, But first, a review of the characteristics and implications of shear band formation during warm rolling will be presented in the section that follows.

II.8.1.1 Shear bands

Shear bands constitute a form of localized flow within a deformed grain, which means that they, like other flow localization phenomena, are sensitive to the deformation temperature, rate sensitivity and work hardening rate [85]. A number of related types of bands have been identified and classified depending on their nature; they have been named microbands, shear bands, deformation bands, lamellar bands, etc. Furthermore, three types of shear bands have been recognized: long, short and intense [66]. However, shear bands show inclinations of 20-35° with respect to the rolling plane without regard to their classifications [86, 87]. As will be seen in more detail below, they play important roles in the metallurgy of warm rolled steels [81].

The formation of shear bands is closely related to the value of the Taylor factor. Grains possessing the highest Taylor factors have the highest potential to form shear bands [48]. Grains of {111}<112> orientation possess high Taylor factors and have been identified as the most prevalent source of shear bands in steel [4, 57, 62, 65]. It is clear from Fig. II.13 that the order of increased potential for shear band formation according to the value of the Taylor factor is {001} < {112} < {111} < {110}. This is consistent with the sequence of increasing stored energy of deformation proposed by Hutchinson [41].

The shear bands formed in {111}<112> grains have often been observed to give rise to Goss nuclei, as well as to near ND-fibre orientations, depending on the conditions under which the shear band is formed [4, 42, 57, 62].

According to several authors, the average r-value is significantly improved by refining the hot band grain size (HBGS) [42, 88, 89]. The explanation offered for this effect is based on the fact that recrystallized {111} grains frequently nucleate on former grain boundaries. Thus a finer HBGS will provide more nucleation sites for {111}//hkl orientations, thereby improving the texture after annealing.

Conversely, coarse-grained materials exhibit higher heterogeneities of deformation. Shear banding is one manifestation of such a heterogeneity, which means that larger initial grain sizes result in more shear bands. However, according to Ushioda *et al.* [4], the recrystallization nuclei formed along shear bands contribute strongly to the Goss texture. Alternatively, other results obtained from warm rolling studies have shown that the fragmentation caused by shear banding plays a large role in the nucleation of ND-fibre grains at sites situated both within the grain interiors and at grain boundaries [65, 90, 91].

The effect of the hot band grain size on the formation of shear bands will be studied in this work to determine its implications on the nature and number of such shear bands and its subsequent effects on nucleation. Two main outcomes from studies carried out previously on the nature of shear bands are that long shear bands of moderate intensity serve as sites for nucleation of the <111>//ND fibre [14], while intense shear bands contribute to the development of the {110}<001> orientation, i.e. of the Goss component [4, 63, 64].

The deformation temperature influences both the deformation texture and the morphology of the shear bands, which in turn influence the recrystallization texture. Shear bands of moderate intensity are formed in IF steels at all temperatures; this results in a partial α-fibre and a continuous γ-fibre of moderate intensity for the deformed condition and a continuous γ-fibre with a high intensity at {554}<225> for the recrystallized material. Conversely, LC steels are characterized by the formation of intense shear bands at low rolling temperatures, with a reduction in intensity as the temperature is increased. This results in a partial α-fibre and a continuous γ-fibre of sharp intensity for the deformed condition and in a *discontinuous* γ-fibre of weak intensity for the recrystallized material [9, 92].

II.8.2 Thermomechanical processing

The thermomechanical processing steps applied to the steel sheet strongly influences the final recrystallization texture. The hot rolling texture, hot band grain size, coiling temperature, cold rolling reduction, annealing temperature, and heating rate during annealing are known parameters involved in hot and cold rolling. Warm rolling is associated with the same parameters. Fine hot band grain sizes enhance the presence of the γ-fibre [88] by promoting the nucleation of recrystallized {111} γ-fibre grains in the close vicinity of the prior γ–γ-grain boundaries [4, 93]. γ-fibre grains nucleate and grow in the early stages of recrystallization by consuming the γ-fibre components of the deformed matrix [91]. Thus, as mentioned earlier, a finer initial grain size should favour the γ-fibre texture after annealing by providing more nucleation sites for grains of this type [42, 89].

The coiling process after hot rolling is employed to control the precipitation of carbides and nitrides, which in the form of uniformly dispersed and relatively coarse particles are favourable to the development of {111} textures during recrystallization. The coiling temperature depends on the type of annealing cycle. High coiling temperatures (>700°C) promote the precipitation of coarse and widely dispersed carbides, and are suitable for continuous annealing production. On the other hand, low coiling temperatures (<600°C) are used in the case of box annealing [51]. Low coiling temperatures promote the formation of uniform dispersions of fine carbides and the low heating rates associated with the second make them coarser [12]. A recovery anneal (aging) after warm rolling has been used in previous works to simulate the effect of slow cooling after coiling and in this way to strengthen the recrystallization texture of LC-Cr and LC steels [9, 94].

Rolling reduction is a key parameter in the production of good textures, as it is well known that reductions of the order of 70-90% give rise to the highest r-values when annealing is carried out after cold rolling [82, 92, 94]. Reductions of around 65% and 80 % have been employed in the warm rolling of low carbon steels, but the results obtained were not satisfactory [9, 13]; this was probably because of the steel chemistry and other parameters may have played a role. When chromium was added and the reduction was increased to around 80%, the resultant textures were satisfactory [11].

According to the results of Senuma and Kawasaki [95], the warm rolling temperature has a notable effect on the reduction required to produce high r-values. For instance, at 750°C, a warm rolling reduction of about 28% was better than 60%. These gave rise to r-values of 1.0 and 0.75, respectively. A good opportunity arises here if low warm rolling reductions can lead to r values close to 1.0, because an additional small cold rolling reduction can increase this value by enhancing the final recrystallization texture. The benefit of this process lies in that, although the cold rolling step is not eliminated, at least it can be reduced from 80-85% to smaller reductions of about 40%. The last, in terms of true strain, represents a reduction from 1.85 for a typical 80% cold rolling reduction to 0.6.

In this work, 65% and 80% warm rolling reductions will be employed in order to compare the present results with previous work. Additionally, the effects of subjecting the initially warm rolled samples to a further 40% cold rolling reduction will be reviewed.

Other alternatives, such as high reduction warm rolling plus high reduction cold rolling [9, 94], or warm rolling-annealing-cold rolling, have also been studied [95, 96]; r-values as high as 1.73 and 3.0 have been obtained for ELC and IF steels, respectively. A résumé of the important results obtained by several authors [9, 11, 94, 95] is presented in Table II.1, while Table II.2 shows the chemical compositions of the corresponding steels. Nevertheless, deformation is not enough to produce high r-values in LC steels and alloying additions are necessary to reduce the detrimental effect of C.

II.8.3 Effect of alloying elements

II.8.3.1 Carbon and nitrogen

Interstitial elements such as carbon and/or nitrogen, when in solution, have an important effect on the mobility and generation of new dislocations. This in turn influences the flow stress, the number and nature of shear bands, and consequently the number and distribution of nuclei and then the final grain size.

Table II.1. Some important results obtained with different thermomechanical schedules taken from references [9, 11, 94, 95].

Author	Steel			Finishing Temp.	Hot rolling thickness	Grain size	Reheat T.		Warm rolling		strain rate	Recovery annealing		Annealing		Cold rolling	Annealing		Grain size	Total red.
		r value	Δr	(°C)	mm	µm	Temp (°C)	time (hr)	Temp (°C)	red. (%)	$\dot{\varepsilon}$ (s^{-1})	Temp (°C)	time (hr)	Temp (°C)	time (hr)	red. (%)	Temp (°C)	time (hr)	(µm)	(%)
M	A	0.5	0.6	>950	11	34	1050	0.5	640	65	30						700	1-4		65
M	B	1.3	0.8	>950	11	~300	1050	0.5	640	65	30						700	1-4		62
M	E	0.9	-0	>950	11	54	1050	0.5	640	65	30						700	1-4		62
M	A	0.5	0.1	>950	11	34	1050	0.5	640	65	30	450	6				700	1-4		65
M	B	1.4	0.8	>950	11	~300	1050	0.5	640	65	30	450	6				700	1-4		62
M	E	0.6	-0	>950	11	54	1050	0.5	640	65	30	450	6				700	1-4		62
M	I	0.6	0.2	>950	11		950	0.5	640	65	30	450	6				700	1-4		62
M	J	0.7	0	>950	11		950	0.5	640	65	30	450	6				700	1-4		62
M	A	**1**	0.2	>950	11	34	1050	0.5	640	65	30					**44**	700	1-4		**80**
M	E	0.9	0.5	>950	11	54	1050	0.5	640	65	30					52	700	1-4		80
B	1	**1.5**		?	10	30	950	1	670	**80**	10	450	4				700	5	40	80
B	3	0.55		?	10	30	950	1	670	80	10	450	4				700	5	62	80
B	2	1.8		?	10	30	950	1	600	85	10	400	3				700	5	21	85
B	3	1.1		?	10	30	950	1	520	85	10	400	3				700	5	15	85
B	2	1.2		?	10	30	950	1	600	85	10	400	3				750	0.33	11	85
B	3	1		?	10	30	950	1	520	85	10	400	3				750	0.33	16	85
T	1	**1.73**	-0	**920**	30	?	1050	0.1	620	66	PC	400	?			**40**	700	?		80
T	2	2.34	0.6	**940**	30	?	1050	0.1	710	66	PC	400	?			**60**	700	?		86.6
S	1	**0.99**		**930**	10	fine			750	**28**							700	1	55	**28**
S	2	**3**		**923**	12	fine			750	75				750	1	80%	700	4	35	92.5

Authors key: M= Toroghinejad et al, B=Barnett, T=Tomitz and Kaspar, S=Senuma and Kawasaki

Table II.2. Chemical compositions of the steels presented in Table II.1 taken from references [9, 11, 94, 95].

Steel	C	Mn	Al	N	Ti	B	Cr	Si	P	S	Nb	Mo
A: ELC	0.020	0.12	0.041	0.0007			0.071	0.006	0.004	0.007		0.004
B: IF(Ti)	0.004	0.15	0.048	0.0037	0.062		0.065	0.006	0.005	0.01		0.018
E: LC(Cr)	0.037	0.35	0.036	0.0012	-	-	0.48	<0.02	<0.02	<0.01	-	-
I: LC(LCr,B)	0.04	0.14	0.032	0.0032	0.015	0.0039	0.49	?	?	?		
J:LC(HCr, B)	0.040	0.15	0.037	0.0025	0.15	0.0045	0.80	?	?	?	-	-
B1	0.060	0.20	0.040	0.0040	-	-	0.57	0.01	0.01	0.01	-	-
B2	0.030	0.11	0.030	0.0030	-	-	1.3	0.041	0.012	0.004	-	-
B3	0.032	0.14	0.043	0.0030	-	-	0.021	0.009	0.012	0.003	-	-
T1: ELC	0.037	0.22	0.040	0.0040	0.001	-		0.01	0.008	0.006	0.002	-
T2	0.002	0.10	0.042	0.0030	0.038	-		0.007	0.01	0.004	0.007	-
S1	0.010	0.24	0.021	0.0020	trace			0.006	0.004	0.004		
S2	0.0032	0.22	0.053	0.0019	0.058			0.018	0.013	0.006		

Solute carbon and nitrogen make steel prone to DSA, a common phenomenon present at temperatures between 150 and 300°C during the deformation of low carbon steels in tensile tests. This can be explained in terms of the way in which interstitial atoms interact with mobile dislocations. At such intermediate temperatures, carbon atoms diffuse to dislocations during deformation and interact with them so as to restrict their motion. This results in enhanced dislocation multiplication, high flow stresses, negative strain rate sensitivities, and serrations in the flow curves [48, 97]. At higher temperatures, carbon atoms move with the dislocations as mobile Cottrell atmospheres [81]. As described above, the presence of the DSA peak leads to high strain rate sensitivities at warm rolling temperatures, reducing the frequency of formation of shear bands. According to independent studies made by Barnett and Toroghinejad et al. [49, 65], such a decrease reduces the number of nucleation sites for the favourable γ-fibre. Fig. II.16 shows the dependence of **m** on temperatures in a LC steel, compared with a material not affected by DSA (ideal).

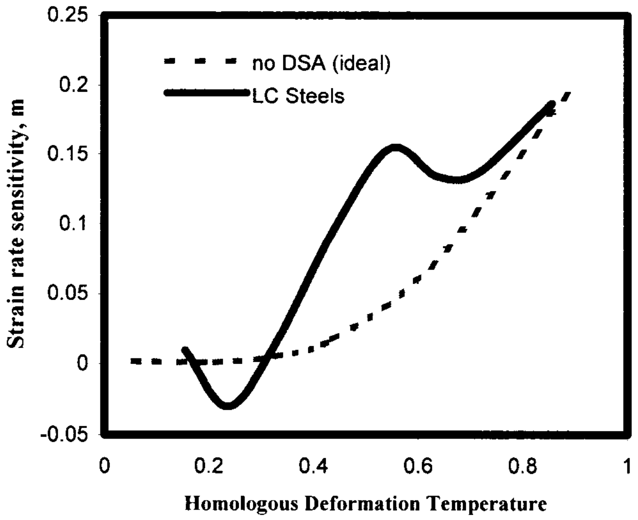

Figure II.16. Dependence of the calculated rate sensitivity (m) upon temperature [81].

The ideal material, not displaying DSA behaviour, is represented by the IF steel grades. In contrast to the LC material, these typically contain large numbers of fine precipitates [52]. The effect of deformation temperature on the interaction between dislocations and precipitates in the IF steels is very weak because these precipitates are essentially stationary at warm rolling temperatures while the solute carbon is not.

II.8.3.2 Chromium

The DSA behaviour of low carbon steels can be modified by adding alloying elements such as chromium and boron and thus extending the DSA peak into the warm rolling temperature region. Previous investigations have shown that these elements create a plateau in the flow stress/temperature curve obtained from tensile tests rather than the single peak usually associated with conventional carbon-nitrogen DSA behaviour (Fig. II.17) [11, 84]. A small increase in strain rate does not then result in a large increase in flow stress within this plateau region, a modification that in turn reduces the rate sensitivity of the material. Although the mechanism for this effect is still not clearly understood, it appears to be due to the formation of C-Cr complexes that are less mobile than isolated solute carbon or nitrogen atoms, resulting in DSA hardening at significantly higher temperatures [13].

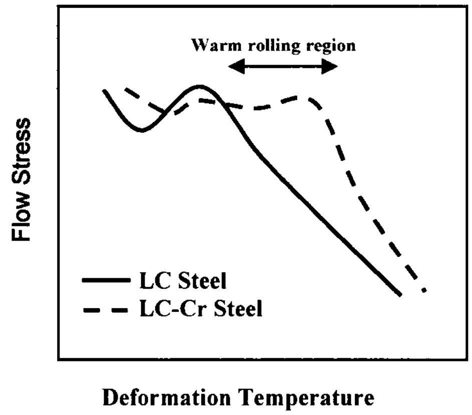

Figure II.17. Effect of chromium addition on DSA in a LC steel [11, 84].

In a recent work, Timokhina and co-workers [66] showed that a particular LC steel can be made to experience a decrease in the number of grains containing shear bands; these are the ones that deteriorate the deformation texture. The addition of chromium to the LC steel (LC(Cr)) reversed this tendency. The increase in shear band frequency in the LC(Cr) steel appeared to be due to the formation of coarse $Cr_{23}C_6$

carbides and fine strain-induced $Cr_{23}C_6$ and Cr_3C_2 carbides. Chromium addition also led to an increase in grain thickness and thus in the tendency to form conventional shear bands.

It is known that strong ND fibre textures, leading to improved formability in warm rolled and annealed low carbon steels, can be obtained with Cr additions of the order of 1.3% and 0.57% [11]. However, in another study, where the Cr addition was about 0.5%, the results were not as favourable as in the first case. Nevertheless, the addition was still found to reduce the strain rate sensitivity [14]. In this work, the effect of the addition of 0.8%Cr will be studied.

II.8.3.3 Manganese

Manganese additions are known to be detrimental to the development of deep drawing textures in low carbon steels. Mn-C complexes form during annealing, owing to the attractive interaction between the dissolved C from cementite and Mn [98]. Such complexes inhibit recovery by retarding the climb rate of dislocations (solute drag effect); they also prolong the incubation period for recrystallization and retard the growth rate of recrystallized grains. Consequently, development of the γ-fibre is weakened and the intensity of the α-fibre is increased after recrystallization. To eliminate the negative effects of Mn, low C and low Mn contents have to be combined; in general, contents of about or below 0.15% Mn lead to good formability [12, 98].

II.8.3.4 Boron

Since boron has a strong affinity for nitrogen, its presence is capable of reducing the susceptibility to DSA and consequently of reducing the strain rate sensitivity. It has been shown that steels with boron contents ranging from 0.007 - 0.020 wt% exhibit greatly diminished aging tendencies [99]. When the boron and nitrogen contents satisfy a stoichiometric ratio of 0.8 to 1.0, low carbon steels display the lowest yield and tensile strengths, peak elongations [100], and highest r-values. On the other hand, at boron contents greater than B/N = 1.0, the effect is reversed and the r-value decreases [101]. However, other authors have found that, in IF steels, lower B/N ratios can be used to obtain high formabilities [102].

In the case of warm rolling, boron additions to low carbon steels have been found to enhance the development of shear bands at the higher rolling temperatures. But despite this desirable effect, boron was detrimental to the annealing texture, as it created a retained rolling component that *reduced* the r-value and hence the formability [14].

CHAPTER III

III EXPERIMENTAL PROCEDURE

The current study is a continuation of previous investigations in which the physical metallurgy of the warm rolling of low carbon steels was explored. The experimental route employed here was intended to improve the formability of these steels and to improve our understanding of the mechanisms of texture formation. In accordance with this approach, the present chapter details the materials, thermomechanical processing routes, and measurement methods employed in the current work.

III.1 Experimental Materials

Two steels were selected for this study, together with an IF steel for comparison purposes. The main criteria involved those characteristics that could lead to improvements in the formability of warm rolled low carbon steels. Two carbon levels were considered together with an optimum amount of manganese and a 0.8% addition of chromium. The chemical compositions are shown in Table III.1. The 0.04%C grade will be referred to here as LC(Cr) and the 0.02%C material as ELC(Cr). Dofasco Inc. of Hamilton, Canada manufactured the two steels

Table III.1 Chemical compositions of the present steels (wt%)

Steel	C	Mn	Al	N	Ti	Cr
LC(Cr)	0.044	0.166	0.042	0.0042	0.015	0.76
ELC(Cr)	0.022	0.151	0.035	0.0038	0.015	0.78
IF	0.004	0.15	0.048	0.0037	0.062	0.02

The steels were cast and forged into 50 mm thick slabs. They were prepared from electrolytic iron to minimize impurity levels of the residual elements and so as to eliminate any unexpected DSA effects.

III.2 Thermomechanical Processing Routes

Rolling trials were completed at CANMET, Ottawa, using the pilot mill operated at an average equivalent strain rate of ~30s^{-1}. Prior to warm rolling, the steel samples were reheated at two different temperatures, soaked for 1½ hours, and then hot rolled down to a thickness of 11 mm. The specimen temperature was monitored using a thermocouple inserted approximately 40 mm into the midplane of each strip.

The first route combined austenitizing at 1250°C; a finishing temperature of 1000°C, and seven passes of small reductions aimed at producing a coarse hot band grain size (CHGS – 30μm). The second involved solution heat treatment and finishing temperatures of 1150 and 950°C, respectively, and four deformation passes with a final reduction of approximately 40%, to generate a finer hot band grain size (FHGS – 18μm). Finishing temperatures lower than 950°C were not considered in order to avoid pancaking the austenite, thus ensuring a uniform recrystallization texture.

Strips of the CHGS samples were subsequently reheated at 1050°C and held for 1 hour, while the FHGS specimens were reheated to the lower temperature of 930°C. These treatments ensured that the carbon had entered into solution. Before warm rolling, the samples were removed from the furnace and wrapped with thermal insulation to promote slow cooling to the test temperature. A soluble oil lubricant was applied to the surfaces of the rolls to reduce friction and thus to avoid a texture gradient through the sample thickness.

The CHGS steels were rolled to reductions of 65% at 640°C and 80% at 700 and 750°C using two to three deformation passes; consequently, the rolling temperatures are average values. To investigate the effects of an additional cold rolling reduction, a second specimen rolled at 640°C was further deformed by 40% at room temperature. After warm rolling, the steel sheets were immediately water quenched to prevent further static recrystallization and hence preserve the as-rolled microstructure. Finally, samples of each material were annealed at 700 °C for 4 hours, using two different heating rates of 2 K.s^{-1} and 1.5x10^{-2} K.s^{-1}. The lower heating rate was selected in order to enhance the precipitation of solute carbon. The first annealing cycle involved a previous recovery anneal of 6 hours at 450C° to simulate coiling. The latter has been found helpful for formability improvement [11, 94], as it removes solute carbon by carbonitride precipitation [9]. The complete thermomechanical schedule is illustrated in Fig. III.1

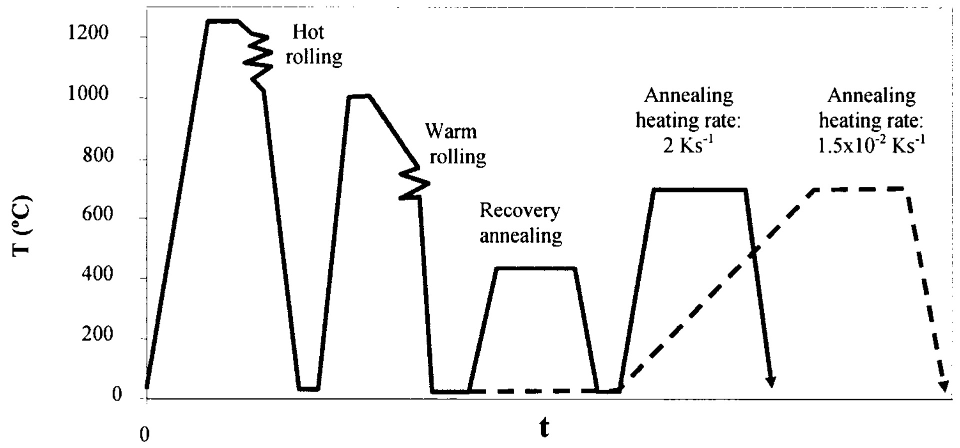

Figure III.1. Schematic of the series of thermomechanical routes for the CHGS steels.

The processing route for the FHGS material was set after knowing the preliminary results for the CHGS. These samples were rolled to reductions of 65% at 640°C and 80% at 580 and 675°C using two to four passes. Additionally, a second specimen rolled at 640°C was further deformed by 40% at room temperature. After warm rolling, the steel sheets were immediately water quenched to prevent further static recrystallization. Finally, all samples were annealed at 700 °C for 4 hours, using a heating rate of 1.5×10^{-2} $K.s^{-1}$. The thermomechanical cycle for this route is illustrated in Fig. III.2

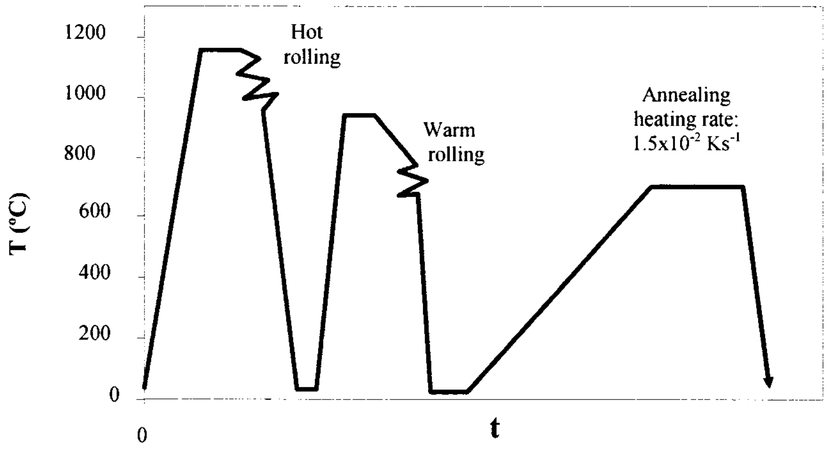

Figure III.2. Schematic of the series of thermomechanical routes for the FHGS steels.

III.3 Annealing

Samples for annealing 20mm long by 5mm wide were cut from the mid-width region of the warm rolled specimens. These dimensions were selected to facilitate heat transfer rates during annealing.

A molten salt bath was used for the annealing trials, as its high heat transfer rate allows for very short annealing times. However, a minimum time is needed for the sample to reach the treatment temperature. To avoid any effect of this on the results, each sample was preheated for 2 minutes in the space above the molten salt [54]. The experimental annealing time started when the sample was immersed into the salt. Samples were annealed at 700°C for times between 5 and 5000 seconds to determine the recrystallization kinetics.

Previous to the partial annealing tests, the temperature in the salt bath was calibrated to assure the reliability of the results. A variation of +/- 7°C between the center of the salt pot and its extremes was found; the depth also showed a +/-3°C gradient. To avoid any effect of this variability, all the samples were submerged 5 cm below the surface at the center of the bath.

III.3.1 Samples for EBSD measurements

Selected samples for EBSD measurements were annealed at different temperatures employing an average heating rate of $4x10^{-2}K/s^{-1}$. The aim was to produce recrystallization percentages of approximately 5, 15, 35, 70 and 100%. The low heating rate was selected on the basis of preliminary results, which pointed to it as an important parameter in the improvement of formability. In this way, the nucleation and growth characteristics of the nuclei generated during recrystallization were studied under optimal experimental conditions.

III.4 Measurements

III.4.1 Microstructural characterization

Microstructural studies were carried out on the as-warm rolled, annealed, and partially annealed samples. Samples were taken from longitudinal sections parallel to the rolling direction. They were prepared by routine metallographic techniques using bakelite mounts and etched with a 2%-nital solution to reveal the microstructure.

Optical microscopy was conducted on specimens of all conditions to obtain information about the number and nature of shear bands in the as-deformed samples; to determine the recrystallization kinetics in the partially annealed samples; and to establish the grain size in the fully recrystallized samples.

The fraction of grains containing shear bands was calculated using a point counting technique. A 15x11 point grid was used and the shear band fraction was determined by taking the ratio of the number of points within grains containing shear bands to the total number of points. In order to obtain a representative value of the shear band fraction, this procedure was repeated 6 times per specimen.

The fraction recrystallized for samples annealed for varying times was measured using a point counting method similar to that employed for the shear bands. The recrystallized fraction was determined by calculating the ratio of the points that lie within recrystallized grains to the total number of points. This procedure was repeated 5 times per sample in order to obtain an accurate estimate of the fraction of recrystallized material.

The grain size for the fully recrystallized samples was determined using a linear intercept procedure according to ASTM standard test method E 112 – $96^{\epsilon 1}$ [103].

III.4.2 Dislocation density

The dislocation density stored in a deformed material is closely related to the hardness of such a material. As recovery and recrystallization advance, the hardness decreases gradually as a result of the rearrangement and elimination of dislocations. Also affected by the dislocation density is the atom plane spacing. A variation in this quantity causes the X-ray diffraction peaks to broaden. As recovery and recrystallization progress, the x-ray line broadening decreases. Previous studies have established the good agreement between the normalized stored energy measured by X-ray diffraction and the normalized dislocation density from hardness measurements [54].

The hardness of the samples rolled under different conditions was measured using a microhardness machine and a Vickers diamond indenter with a load of 20 Kgf. The results obtained from these measurements are directly proportional to the flow stress, which in turn, is a function of the square root of the dislocation density [80]. The measured samples were the same as those used for the determination of the recrystallization kinetics. Five measurements were carried out on each sample and then averaged. The hardness of the samples before deformation was subtracted from the as-rolled measurements and the results were squared. Then, the squared results were normalized by dividing them all by the highest. The final value is expected to be linearly related to the stored dislocation density.

III.4.3 Compression testing

Compression tests were carried out at deformation temperatures between ambient and 900°C using a servo-hydraulic axial compression machine. The cylindrical specimens were 11.4mm in height and 7.6mm in diameter and were machined from the forged slabs. Prior to testing, the samples were soaked for 15 minutes at 900°C to promote dissolution of the carbides and hence maximisation of the DSA effects. Samples were then rapidly cooled to each test temperature using forced air. In order to minimize friction during testing, sheets of pelco mica, lubricated with a mixture of boron nitride powder and ethanol, were placed between the specimen and the anvils. The flow stress of each material was measured at a compressive strain of 10% at strain rates of 10^{-1}, 10^{-2} and $10^{-3}s^{-1}$, allowing the rate sensitivity of the (work hardened) flow stress to be calculated for each material [104]. The value of 10% strain was chosen because the effect of barrelling is minimal at this point and the strain hardening is high enough for the effect of DSA to be detectable on the stress-strain curve.

III.4.3.1 Flow stress

The engineering stress was calculated from the data acquired from each compression test, according to:

$$s = \frac{4F}{\pi d_0^2} \qquad 8)$$

where F is the applied force and d_0 is the initial diameter of the compression specimen. On the other hand, the engineering strain, e, was calculated using Equation 9, where h_0 is the initial height of the specimen and Δh is the change in specimen height.

$$e = \frac{\Delta h}{h_0} \times 100 \tag{9)}$$

However, the elastic part of the engineering stress-strain curve involves an apparent strain associated with the elasticity of the compression machine and tools, which is present as a linear portion at the beginning of the strain-stress curve [105]. If a line is drawn through this straight segment, it is possible to fit the data to a linear equation of the type:

$$y = mx + b \tag{10)}$$

The apparent strain (e_c) associated with the compression machine was then calculated as:

$$e_c = \frac{s - b}{m} \tag{11)}$$

where s is the engineering stress corresponding to the end of the elastic portion of the curve, m is the slope of the elastic portion, and b the y-intercept of the plastic portion. The adjusted strain (e_S), was then calculated by subtracting the strain of the compression machine from the engineering strain (e), see equation 12, which represented the actual strain in the sample. This was the value used for further calculations.

$$e_s = e - e_c \tag{12)}$$

III.4.3.2 Rate sensitivity

Rate sensitivities were calculated for each deformation temperature using Equation 7 and the plots of flow stress vs. strain rate. Log scales were used since the slope of a straight line on this graph is the rate sensitivity at the given temperature.

III.4.4 Texture measurement by X-ray diffraction

Bulk texture changes after warm rolling and full annealing were measured in specimens of each condition. Textures were determined by measuring three incomplete pole figures, {200}, {110} and {112} with a Siemens D500 goniometer system (Mo tube) and the standard reflection technique.

Using Bunge's series expansion method [27], the orientation distribution functions (ODF's) were calculated from the pole figure data, with an expansion of l_{max}=22 [106]. Textures were represented in the reduced $0° \leq \varphi_1$, Φ, $\varphi_2 \leq 90°$ Euler space, since cubic crystal and orthorhombic sample symmetries are involved.

Estimated mean Lankford values (r_m) for these samples were calculated on the basis of the texture data using software developed at McGill University. These values are presented as functions of the angle to the rolling direction. The calculations were made using the relaxed constraint method of crystal plasticity, where the critical resolved shear stress ratio (α) for glide on the {112}<111> slip systems ($\tau_{\{112\}}/\tau_{\{110\}}$) is 0.95. These simulations were based on the observation that the grains in the present steels are of pancake shape (For the *annealed* microstructures, the calculation was considered to be an approximation). The appendix contains a comparison between calculated and measured r-values for selected samples.

III.4.4.1 Sample preparation

Specimens 15 mm x 25 mm with the main area parallel to the rolling plane were cut from the mid-width regions of the as-rolled strips to avoid possible edge effects from the rolling process, Fig. III.3. The samples were ground down to half thickness using 1200 grinding paper, polished with 3μm diamond cloth, and finally electro-polished. A solution containing 20% perchloric acid and 80% acetic acid was used for electro-polishing, applying a current of 3-4 amps and a voltage of 30V for 90 sec.

III.4.5 Microtexture measurement by EBSD

EBSD measurements were carried out in order to obtain information related to the nucleation and growth characteristics of the main crystallographic orientations. Automated electron backscattered diffraction measurements were performed with a field emission type microscope at the Université catholique de Louvain, in Louvain-la-Neuve, Belgium. An acceleration voltage of 20 keV, together with a working distance of 15 mm and the sample tilted 70° were selected to maximize backscattered electron diffraction. Additionally, as the smallest nucleus size was considered to be of the order of 1μm [15], a 0.3 μm step size was chosen, because a minimum ratio of 1:3 between the step size and the size of the smallest feature of interest is required for the data to be consistent. Sampled areas of about $3 \times 10^5 \mu m^2$ were measured to obtain a statistically reliable number of indexed points.

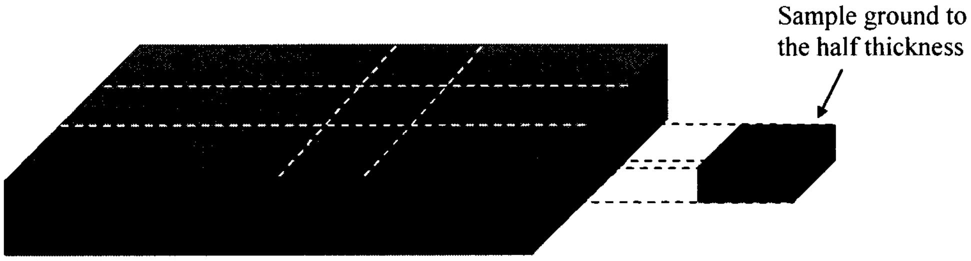

Figure III.3. Schematic of sample preparation.

The EBSD patterns collected from the scans carried out in the FEG-SEM were processed using the fully automated data acquisition programs TexSem™ and HKL. The output of an EBSD scan consisted of a list of records containing the (x,y) coordinates of each indexed pattern, a phase indicator, the three Euler angles and a parameter that weights the quality of the acquired pattern (known as image quality, IQ, or band contrast, BD) [34, 38]. During post-processing, this information was transformed into images, from which various characteristics related to the crystallography of the sample can be represented according to a certain colour code. The principles of the software are illustrated in Fig. III.4.

In the current work, the following information was obtained from the EBSD measurements and processed for further analysis:

- Orientation matrices, which were exported for further mathematical manipulation,
- Crystallographic orientation maps,
- Inverse pole figures,
- Euler angles
- Misorientation profiles
- Grain boundary maps
- Image quality maps.
- ODFs from EBSD data.

Since diffraction only occurs in the top 10-50 nm of the specimen [26], a sample surface free of distortion is needed in order to get a good electron backscattered pattern (EBSP). Therefore, special steps were necessary in addition to the classical preparation for optical metallography.

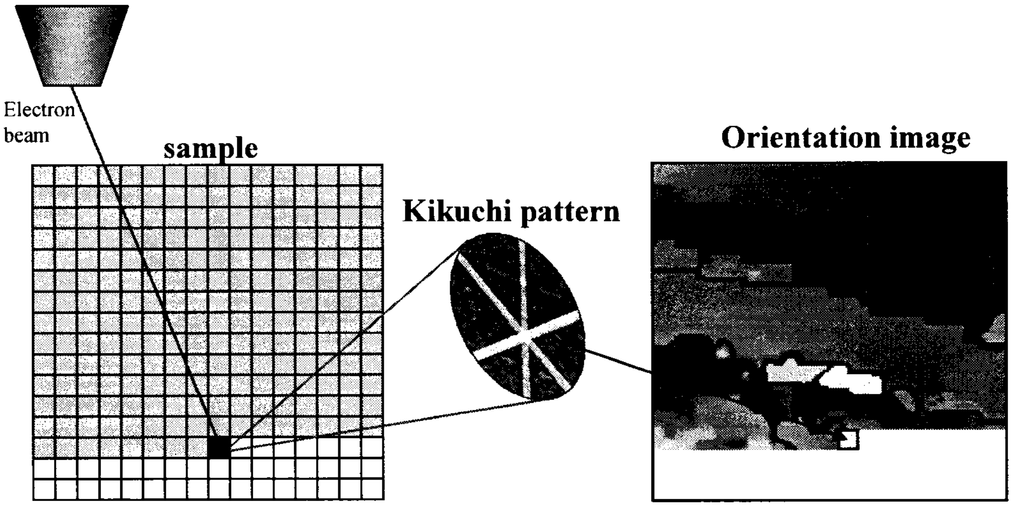

Figure III.4. Schematic illustration of the principles of orientation imaging.

III.4.5.1 EBSD sample preparation

When an EBSD sample is inserted into the FEG-SEM chamber, a conducting mounting medium or some other way of establishing electrical contact is required. Otherwise, electrical contact to the specimen cannot be established and the sample will become charged, consequently preventing a clear EBSD pattern from being obtained.

In order to avoid the introduction of superficial mechanical stresses, the sample was ground starting with a grit size of 600-800 and a rotation speed of 150 rpm. Then it was polished using 3 and 1 micron diamond polishing for periods of 10 and 30 minutes, respectively. Finally, samples were polished for 50 minutes using colloidal silica. Long polishing periods were selected to ensure that most of residual stresses at the surface were removed. This last step is very important because the absence of an EBSD pattern in a representative sample is evidence that it is non-crystalline, highly strained, or that the grain size is finer than the probe size [26].

CHAPTER IV

IV RESULTS

This section is divided into three main parts; first, the results are given pertaining to the deformed state, such as the deformed microstructures, the DSA behaviour, the normalized dislocation density, and the deformation textures. Second, the recrystallization kinetics, the recrystallized microstructures and the recrystallization textures, and their effects upon anisotropy are presented. Finally, the results related to the nucleation and growth behaviour are shown.

IV.1 Deformation Microstructure

The as-hot rolled microstructures of steels LC(Cr) and ELC(Cr) are illustrated in Figs. IV.1a and b, respectively, for the finishing temperature of 1000°C; these were preheated to 1250°C and are referred to here as the coarse hot band grain size (CHGS) samples. The microstructures of the same two steels are presented in Figs. IV.1c and d, respectively, for the finishing temperature of 950°C and a reheat temperature of 1150°C (FHGS case). It is readily evident that the higher reheat and finishing temperatures led to coarser microstructures in both cases. The average grain size for the CHGS samples was 26-30μm while it was 18μm for the FHGS samples.

The warm rolling microstructure is highly affected by the rolling temperature and amount of reduction. The most noteworthy features are the elongation of the deformed grains and the deformation or shear banding. Shear bands, which are contained within individual grains, are typically inclined at 15 to 35 degrees to the rolling direction. Optical micrographs presenting the effects of deformation temperature and amount of deformation are illustrated in Fig. IV.2 for the ELC(Cr) steel. Clearly, the amount and intensity of the shear bands increase with decreasing temperature and increasing rolling reduction. In the additionally cold rolled sample, particularly coarse in-grain banding is evident. On the contrary, the few in-grain bands at 750°C are very fine and short. These microstructures are also representative of the LC(Cr) steel; as no significant difference was observed, they are not represented here.

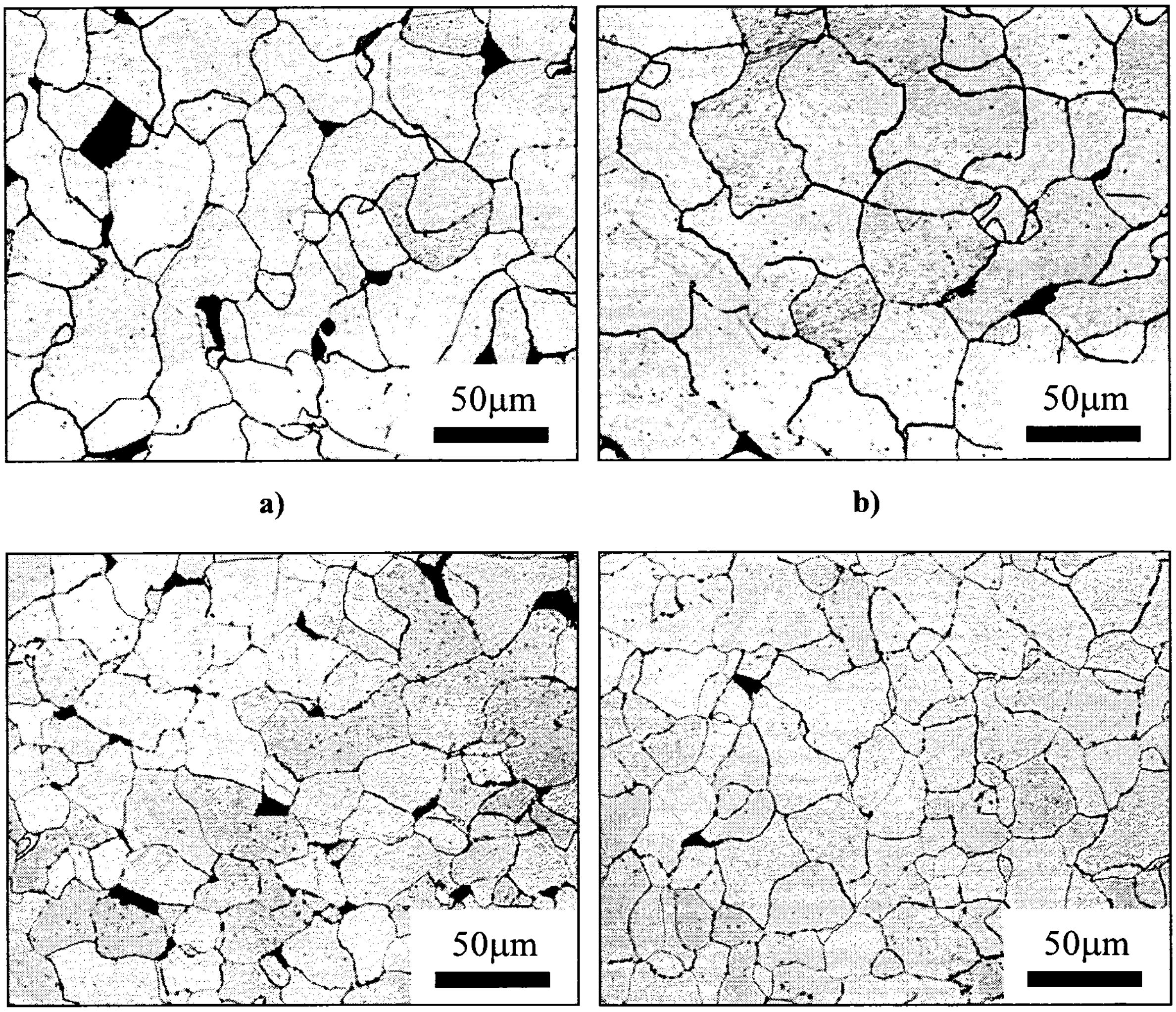

a) b)

c) d)

Figure IV.1. Hot rolling microstructures: a) and b) CHGS samples and c) and d) FHGS samples. Micrographs a) and c) correspond to steel LC(Cr) and b) and d) to steel ELC(Cr).

a)

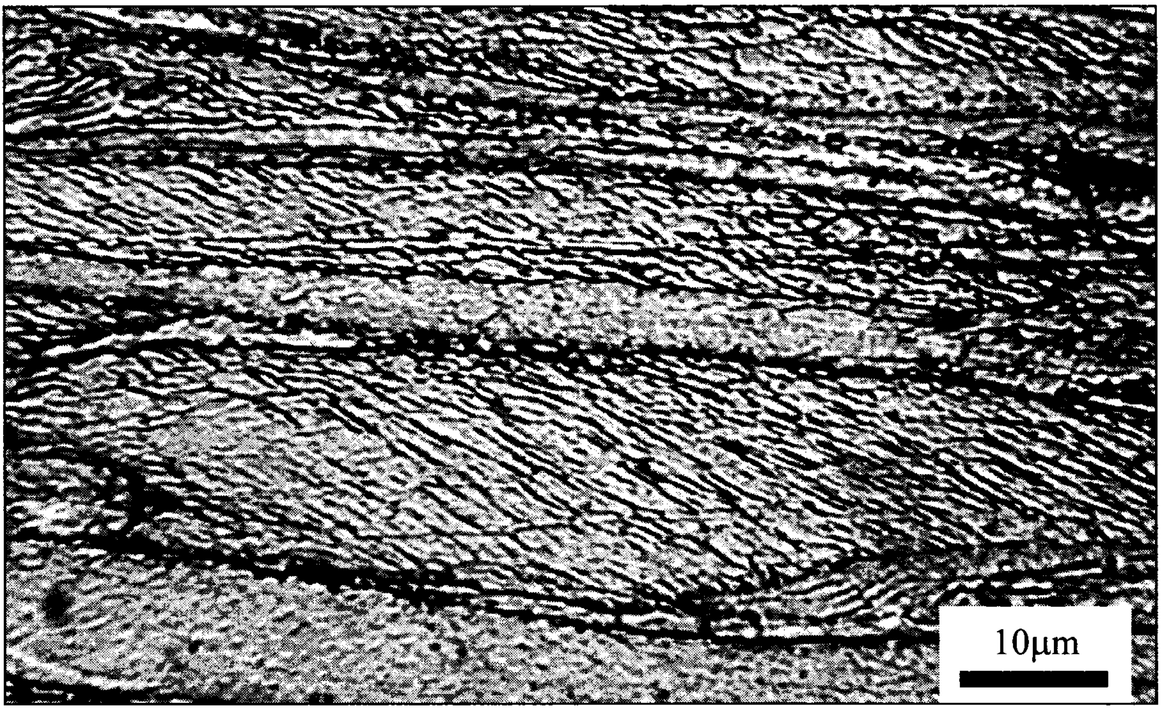

b)

Figure IV.2. Micrographs showing elongated grains containing in-grain shear bands in the ELC(Cr) sample. The following warm rolling conditions were covered: a) 80%WR @ 750°C, b) 80%WR @ 700°C, c) 65%WR @ 640°C and d) 65%WR @ 640°C plus an additional 40%CR reduction.

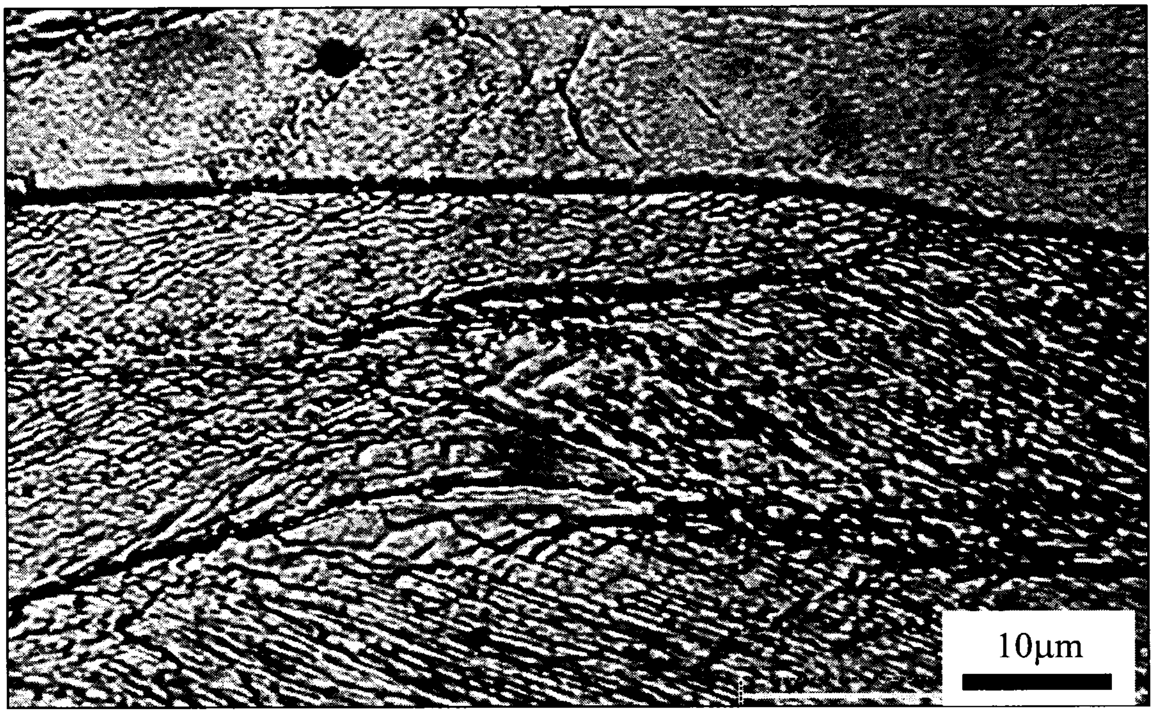

c)

d)

Figure IV.2. Continuation...........

IV.2 Dynamic Strain Aging

The dependence of the flow stress (at 10% strain) on temperature in the LC(Cr) and ELC(Cr) steels is presented in Fig. IV.3. Here, the results for a plain extra low carbon steel (ELC) and a low carbon steel with chromium and boron additions (LC(Cr,B)) from a previous study [13, 14, 105], are included for comparison purposes. The chemical compositions of these steels are given in Table IV.1.

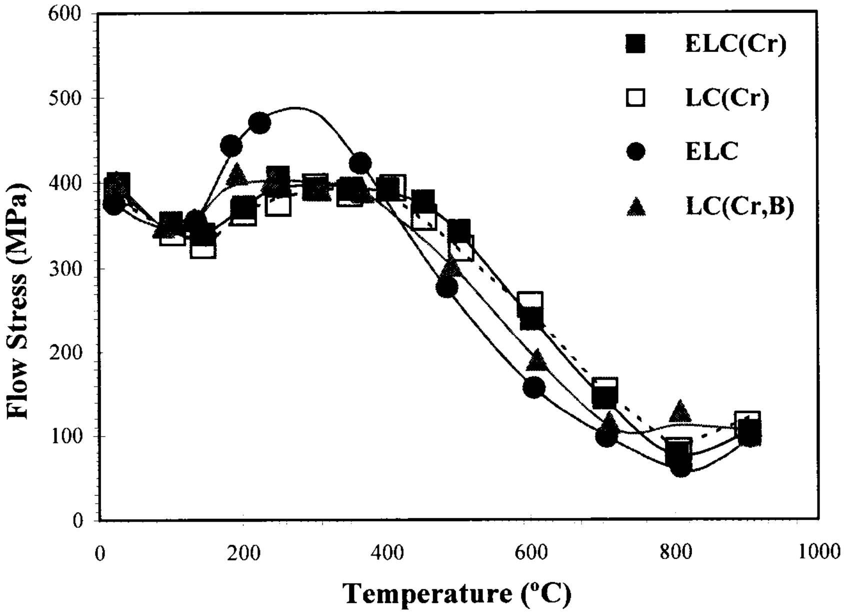

Figure IV.3. Dependence of flow stress (at $\varepsilon = 0.10$) upon temperature (at strain rate of $10^{-1}s^{-1}$)

Table IV.1. Chemical compositions of the literature steels (wt%).

Steel	C	Mn	Cr	Al	Ti	P	B	N
LC	0.02	0.12	0.071	0.041	-	0.004	-	0.0067
LC(Cr,B)	0.04	0.15	0.08	0.037	0.015	-	0.0045	0.0025

The present LC(Cr) and ELC(Cr) steels displayed flow stress peak behaviours similar to those of the previous LC(Cr,B) and ELC steels. However, the DSA peaks exhibited by the LC(Cr), ELC(Cr) and LC(Cr,B) steels were broader than that of the ELC steel. It is important to note that the DSA hardening range was extended to temperatures

350°C above the flow stress maximum for the two present LC-chromium steels and that the upper limit of this range is about 100°C higher than that for the LC(Cr,B) steel.

The broadening of the flow stress peak reduced the strain rate sensitivities of the LC(Cr) and ELC(Cr) steels to values below those for the ELC steel, while the further addition of boron brought them still closer to those for the ideal material, as illustrated in Fig. IV.4.

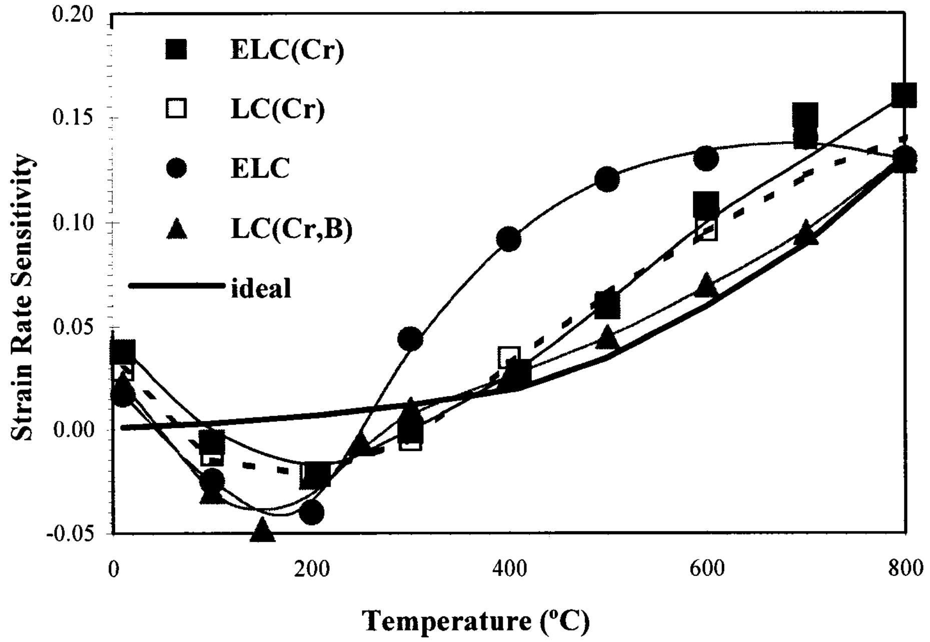

Figure IV.4. Calculated strain rate sensitivities of the four steels (at a mean strain rate $\dot{\varepsilon}$ of $10^{-2}s^{-1}$)

The strain rate sensitivity has an important effect on the morphology of the resulting shear bands. For instance, the present ELC(Cr) steel displayed longer and more intense shear bands than the previous ELC material in samples deformed 65% at 640°C. This is illustrated in Fig. IV.5.

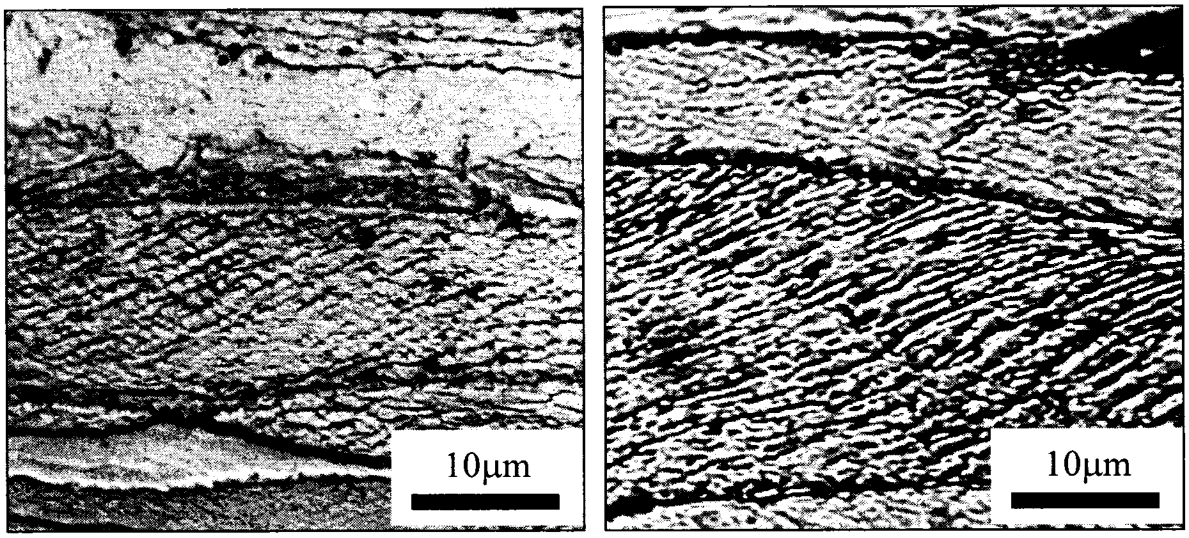

a) b)

Figure IV.5. Deformation microstructures after warm rolling at 640°C, showing the morphology of shear bands for steels 65% deformed at 640˚C: a) ELC; b) ELC(Cr) steel.

IV.2.1 Shear bands

The change in the volume fraction of grains containing in-grain shear bands in the LC(Cr) and ELC(Cr) steels with coarse hot band grain sizes (CHGSs) is presented in Fig. IV.6. It can be seen that lower WR temperatures and higher reductions increased the number of shear bands. There was little difference between the two steels, although the ELC(Cr) displayed a slightly higher fraction.

The effect of hot rolling finishing temperature on the number of grains containing in-grain shear bands is illustrated in Fig. IV.7. It can be seen that the fraction of such grains was slightly reduced when the initial hot band grain size was refined; this corresponds to the ELC(Cr)-FHGS sample.

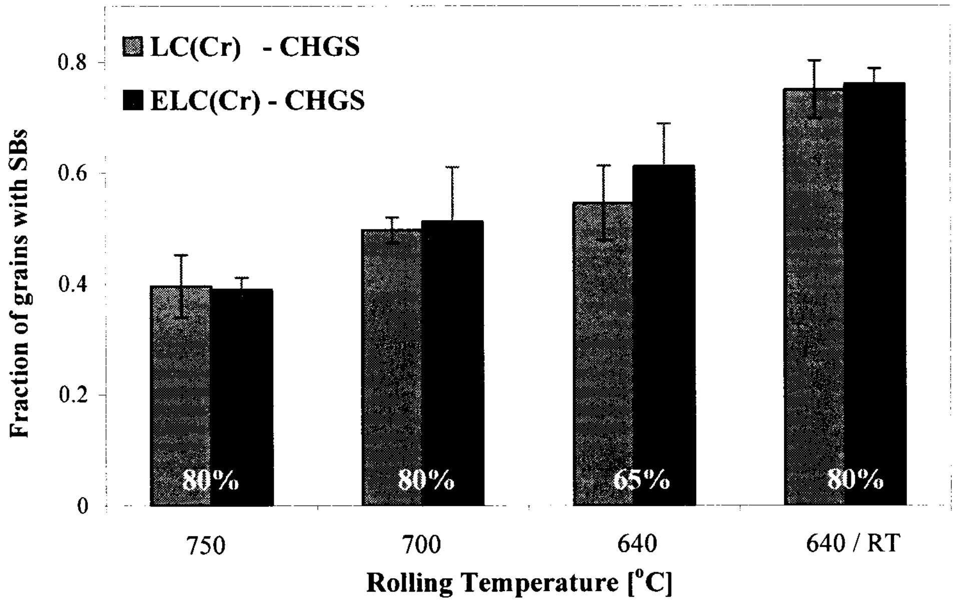

Figure IV.6. Volume fraction of grains containing in-grain shear bands produced at different WR temperatures. The deformation applied at each temperature is shown on each bar. The 640/RT sample was 65% deformed at 640°C and further reduced 40% at room temperature.

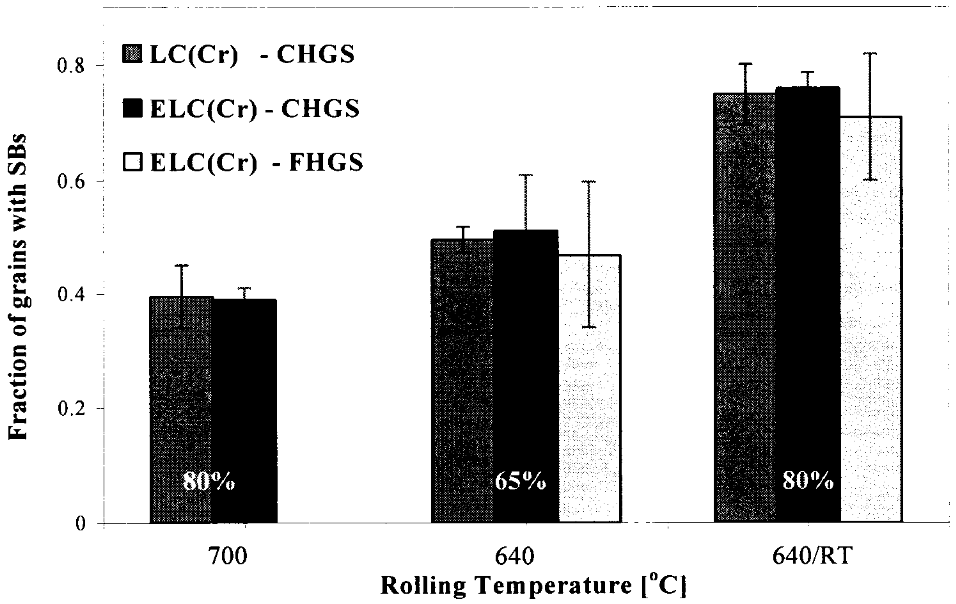

Figure IV.7. Volume fraction of grains containing in-grain shear bands produced at different WR temperatures. The deformation applied at each temperature is shown on each bar. The 640/RT sample was 65% deformed at 640°C and further reduced 40% at room temperature.

The addition of chromium raised the fraction of grains containing shear bands to about 50% compared to that for the literature ELC steel at rolling temperatures of 640 and 700°C; this can be seen in Fig. IV.8. On the other hand, the further addition of boron produced a similar effect at 640° and appeared to be slightly more effective at 700°C. However, boron additions also promote the retention of a strong RD component in the recrystallization texture [13, 14, 104].

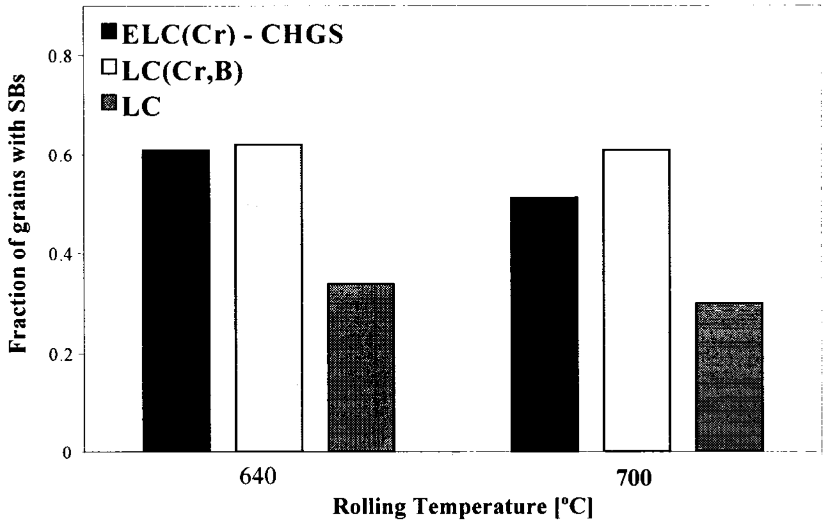

Figure IV.8. Volume fraction of grains containing shear bands after rolling at 640 and 700°C.

IV.3 Dislocation Density

The present results show that the deformation temperature has an important influence on the dislocation density. As can be seen in Fig. IV.9 for the CHGS specimens, true strains of 1.2 (65% reduction) and 2 (80% reduction) produced the same dislocation density at 640 and 700°C, respectively, even though the sample deformed at 640°C was submitted to a lesser amount of deformation. Moreover, a lower true strain of 1.8 consisting of a further 40% cold rolling reduction applied to the latter augmented the dislocation density by approximately 300%.

The results corresponding to the FHGS material, illustrated Fig. IV.10, show that refinement of the hot band grain size prior to warm rolling leads to an increase in dislocation density at all temperatures. The influence of the initial microstructure is clearly greatest at lower temperatures.

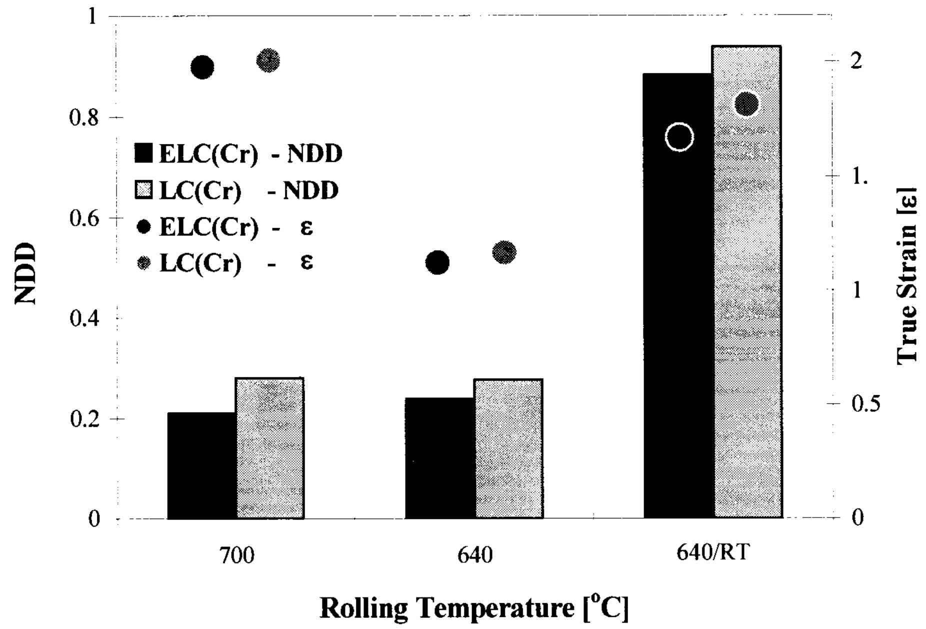

Figure IV.9. Normalized dislocation density, calculated from hardness measurements, and the true strain corresponding to each applied reduction for the CHGS materials.

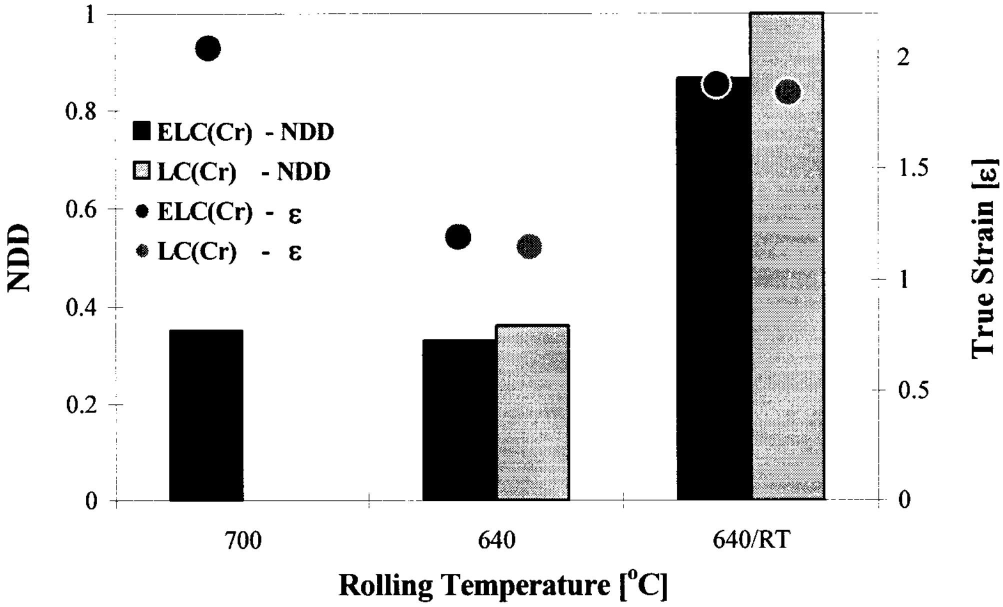

Figure IV.10. Normalized dislocation density, calculated from hardness measurements, and the true strain corresponding to each applied reduction for the FHGS materials.

IV.4 Deformation Texture

The deformation textures of the LC(Cr) and ELC(Cr) steels for the CHGS condition are displayed in Fig. IV.11 in the Φ_2=45° section of the ODF. These textures were similar and consisted of a strong rotated cube component, an intense α-fibre running from {001-111}//<110>, and a γ-fibre running from {111}<110-112>. The intensity of the deformation texture increased with rolling temperature and the amount of deformation, but no difference was observed between the LC(Cr) and ELC steels. When a further 40% cold rolling reduction was applied to the samples warm rolled 65% at 640°C, the intensity of the texture increased slightly, but its distribution remained unchanged.

In the case of the FHGS material, the texture intensity was almost 1.3 times higher than that of the CHGS, presumably due to the greater restrictions on dislocation movement introduced by the finer grain size. This is illustrated in Fig. IV.12 for the ELC(Cr) sample warm rolled to a reduction of 65% at 640°C.

IV.5 Recrystallization Kinetics

The recrystallization kinetics are of considerable importance for selection of the annealing parameters necessary for consistent production. In this section, results are presented concerning the effect of deformation temperature and amount of deformation on the kinetics.

The kinetics of recrystallization of the LC(Cr) and ELC(Cr) steels with initial CHGSs are given in Fig. IV.13. Standard JMAK curves with n values of 2 were fitted to the results to enable interpolation of the time to 50% recrystallization. According to these results, the warm rolled steels exhibit approximately the same kinetics for deformation temperatures of 640 and 750°C, although the 640°C samples were subjected to lower strains. Compared to the LC(Cr) material, the ELC(Cr) displayed slightly faster kinetics. The additional 40% cold rolling reduction applied to the 65% warm rolled sample had a considerable effect on the recrystallization behaviour, reducing the time for 50% recrystallization from 300 to 20 seconds.

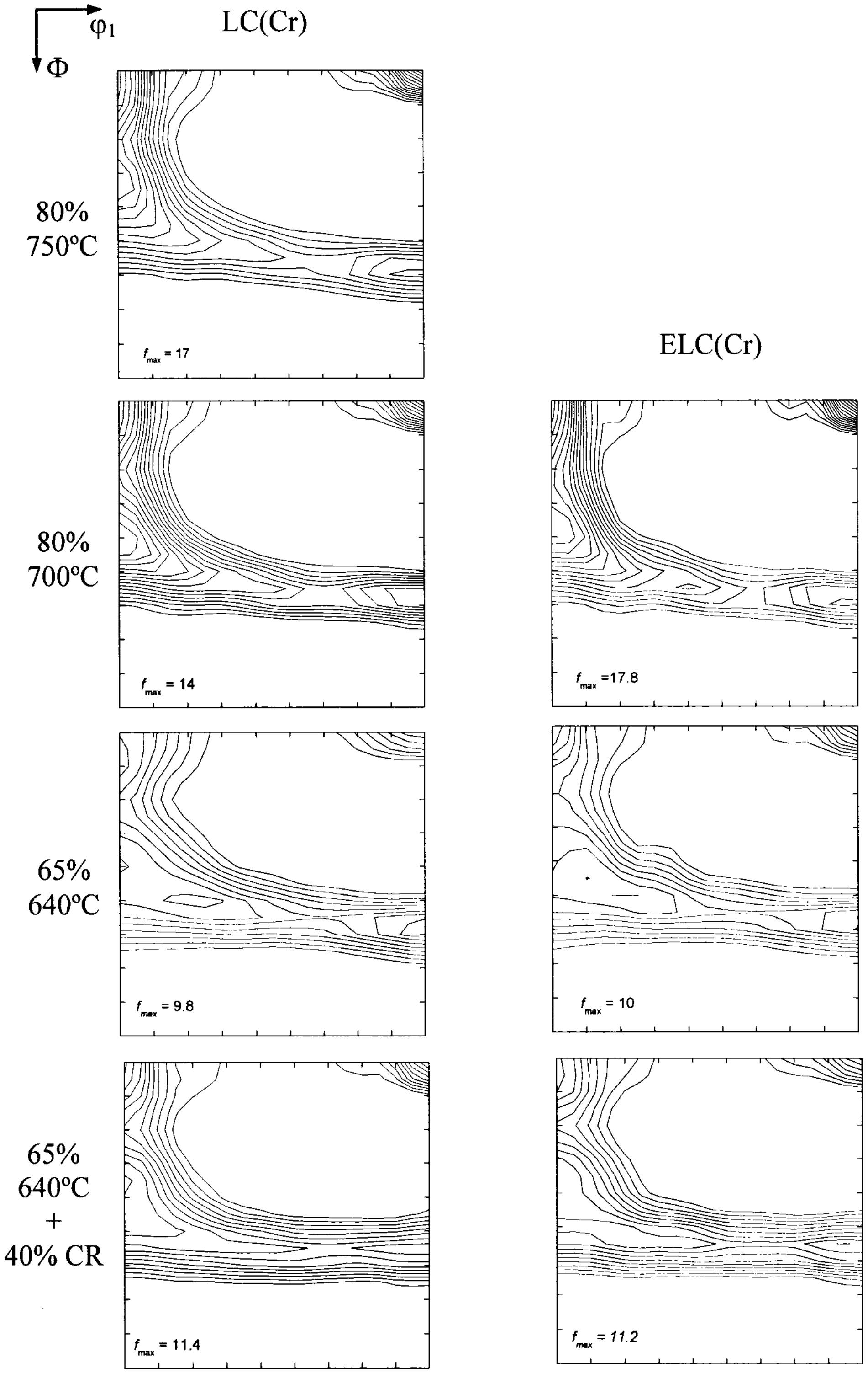

Figure IV.11. Warm rolling textures of the LC(Cr) and ELC(Cr) steels for the CHGS condition. The deformation temperature and rolling reduction are indicated at the left of each ODF. (levels 2,3,….).

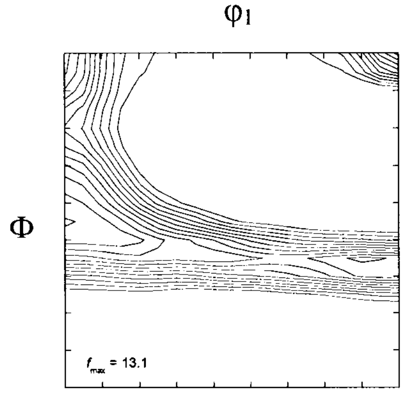

Figure IV.12. Warm rolling texture of the ELC(Cr) steel (FHGS condition) warm rolled 65% at 640°C. (levels 2,3,….).

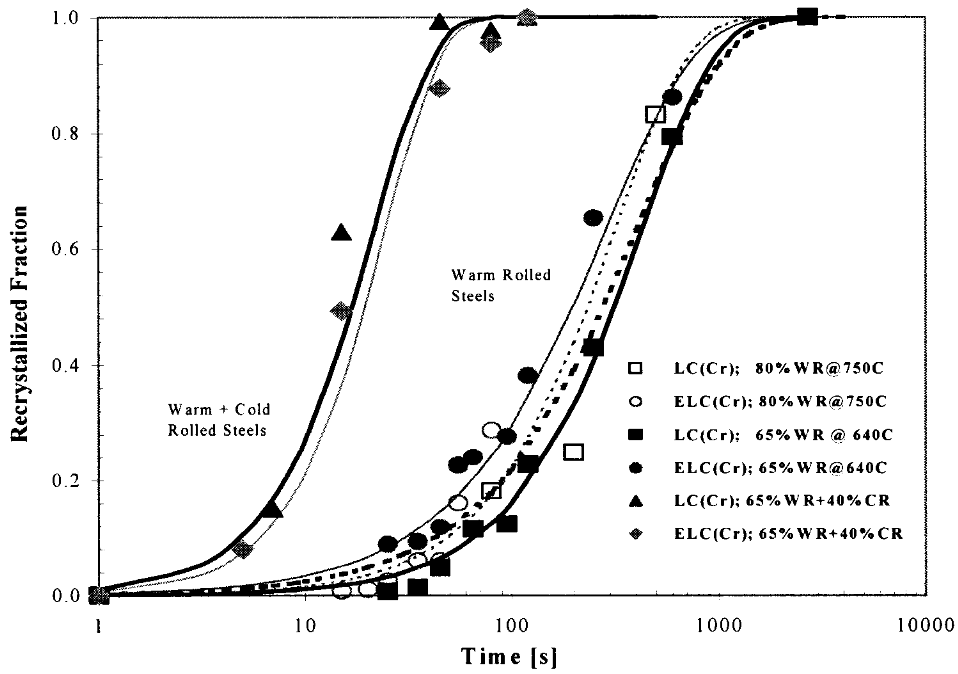

Figure IV.13. Recrystallization curves for the LC(Cr) and ELC(Cr) steels with CHGSs.

In the case of the FHGS materials, the finer initial grain size modified the kinetics of recrystallization. This effect is presented in Fig. IV.14 for samples prepared for the EBSD studies. These were annealed at a constant heating rate of $4\mathrm{x}10^{-2}$ $\mathrm{K.s}^{-1}$ under non-isothermal conditions and quenched immediately after reaching each selected temperature. Although no direct comparison can be made in terms of time, it is clear that recrystallization is more rapid when the hot band grain size is refined. Results for a regular IF steel are included in this graph, which will be used for comparison purposes in section IV.8.

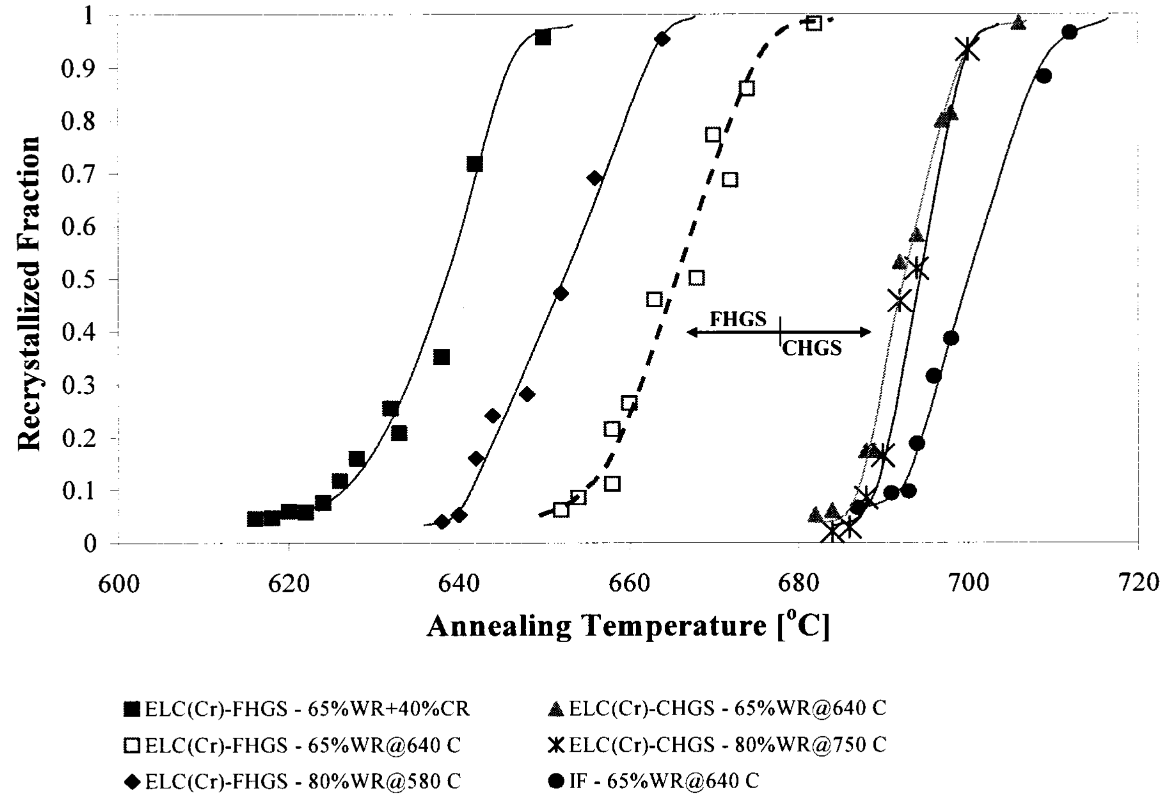

Figure IV.14. Non-isothermal recrystallization curves for the LC(Cr) and ELC(Cr) steels with initial CHGSs determined using a heating rate of $4\mathrm{x}10^{-2}\mathrm{K.s}^{-1}$.

IV.6 Recrystallization Texture

In this section, the ODF's of the recrystallization textures are presented for the experimental samples after a 4 hour anneal at 700°C. The results are divided into three main groups. The first corresponds to the CHGS samples annealed at a medium heating rate of $2K.s^{-1}$. The second presents the effect of lowering the heating rate to $1.5x10^{-2}Ks^{-1}$ on the CHGS material. Finally, results obtained on the FHGS samples annealed using the same lower heating rate are illustrated.

The recrystallization textures for the LC(Cr) and ELC(Cr) steels in the CHGS condition are displayed in Fig. IV.15. These samples were annealed using a medium heating rate of $2K.s^{-1}$. It is evident from these results that a strong rotated cube component, a dominant <110>//RD fibre, and a <111>//ND fibre are present after warm rolling under all conditions.

IV.6.1 Effect of heating rate on the recrystallization texture.

The recrystallization textures of the experimental steels annealed using the low heating rate ($1.5x10^{-2}K.s^{-1}$) are presented in Fig. IV.16. These ODF's can be compared to those presented in Fig. IV.15 for the same steel annealed using a heating rate of $2K.s^{-1}$. The slower heating rate contributed to a weakening of the RD fibre and to forming a more continuous ND fibre. The effect was more evident in the sample without additional cold rolling, in which the cube component almost disappeared and the intensity of the ND fibre was increased.

IV.6.2 Effect of hot band grain size

Figure IV. 17 shows some of the annealing textures produced in the experimental steels when processed in the FHGS condition. The samples were annealed using the same lower heating rate as for the samples of Fig. IV.16. These textures exhibit important differences with respect to the CHGS samples, featuring a more intense and nearly continuous γ fibre but also a stronger retained RD fibre.

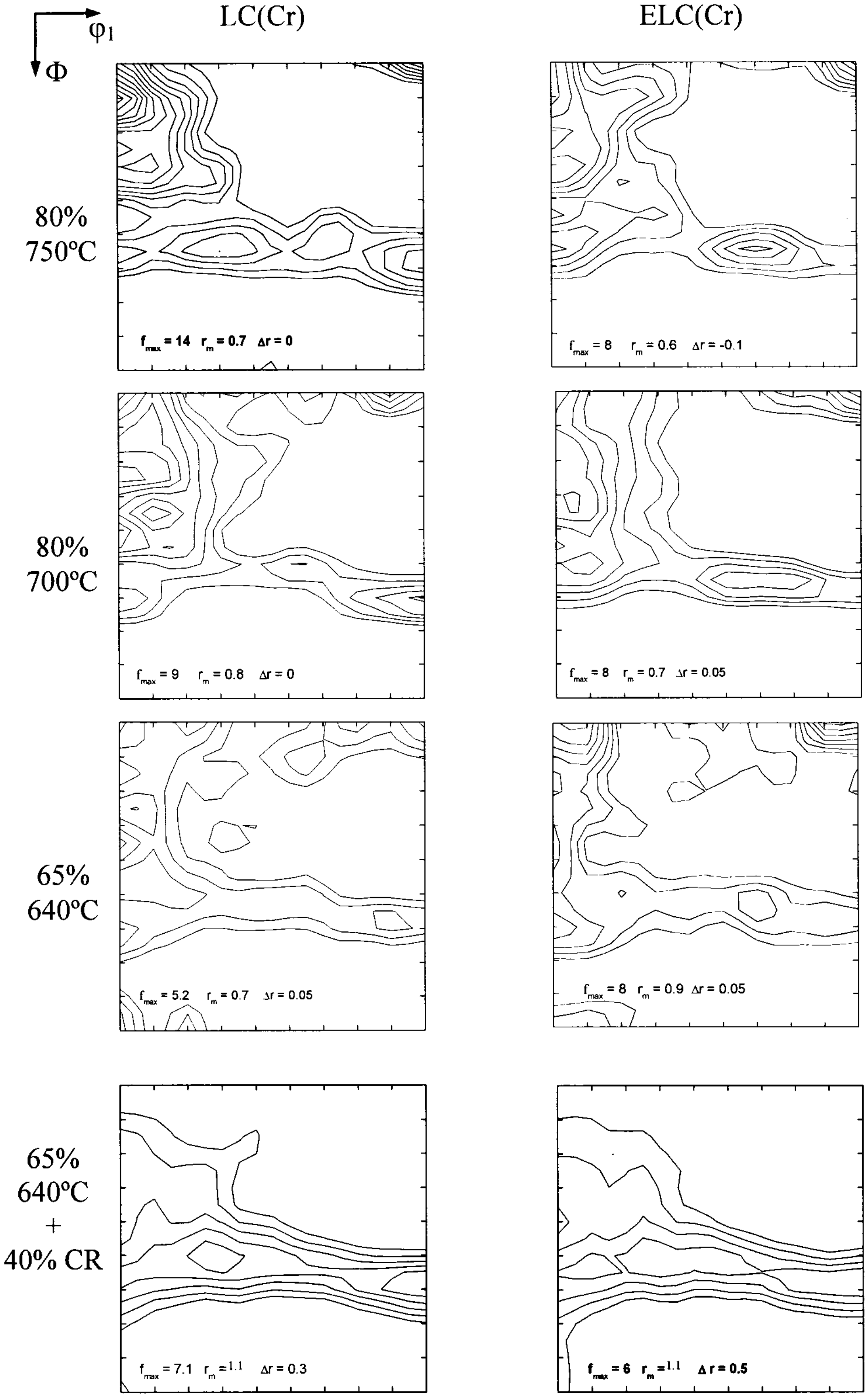

Figure IV.15. Recrystallization textures of the LC(Cr) and ELC(Cr) steels in the CHGS condition; after 4 hours of annealing at 700°C using a heating rate of 2K.s^{-1}. The deformation temperature and rolling reduction are indicated on the left of each ODF. (levels 2,3,....).

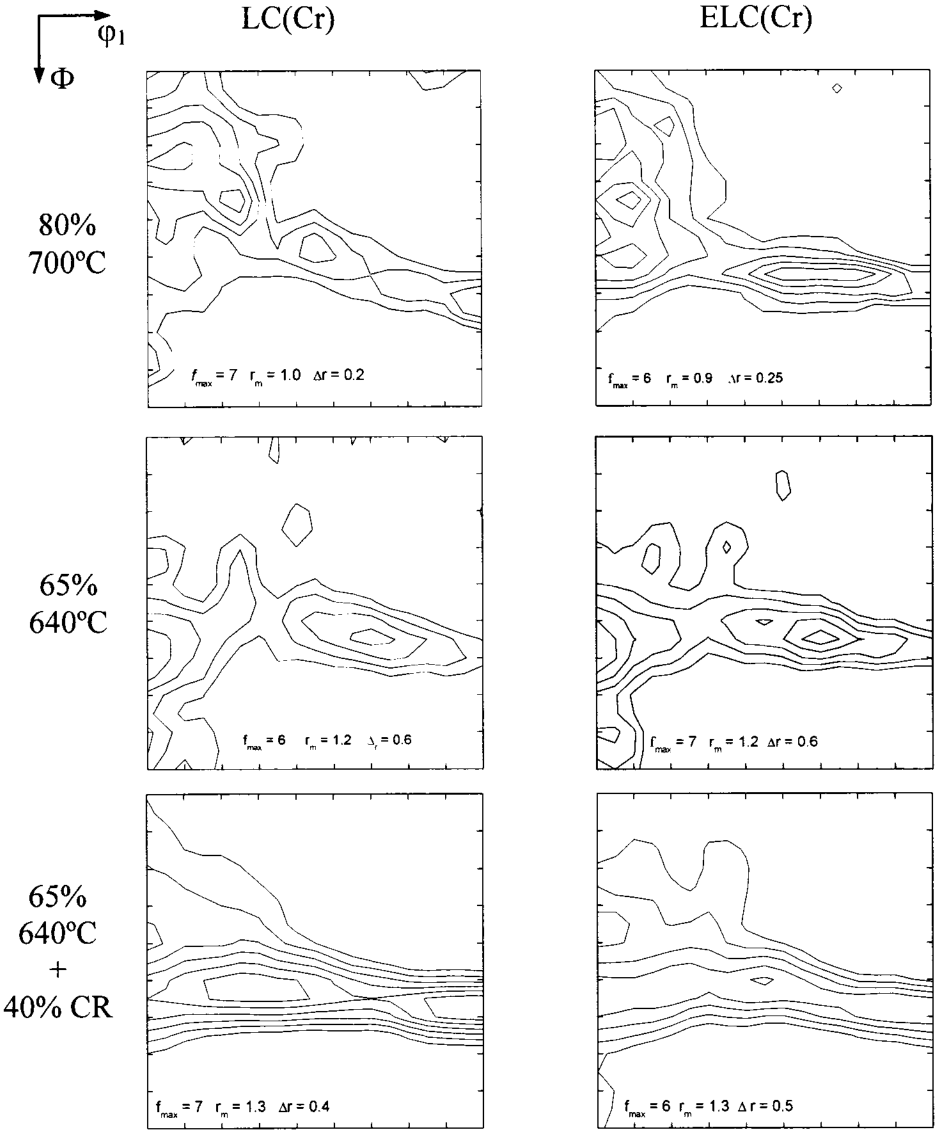

Figure IV.16. Recrystallization textures of the LC(Cr) and ELC(Cr) steels in the CHGS condition; after 4 hours of annealing at 700°C using a heating rate of $1.5X10^{-2}K.s^{-1}$. The deformation temperature and rolling reduction are indicated on the left of each ODF. (levels 2,3,....).

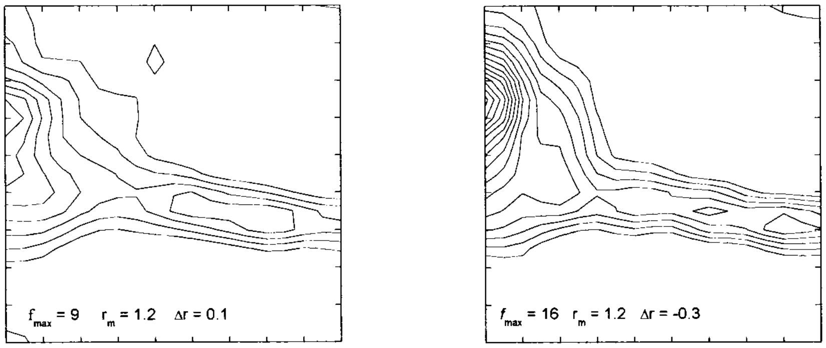

640°C, 65%

640°C, 80%

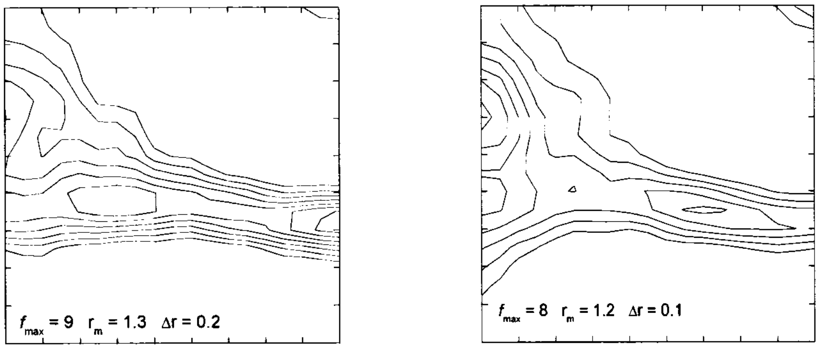

640°C / RT, 80%
(65%WR + 40%CR)

580°C, 80%

Figure IV.17. Recrystallization textures of the ELC(Cr) steel in the FHGS condition; after 4 hours of annealing at 700°C using a heating rate of $1.5X10^{-2}$ $K.s^{-1}$. The deformation temperature and rolling reduction are indicated below each ODF. (levels 2,3,....).

IV.7 Anisotropy

The r-values (calculated using a crystal plasticity program) and the amount of reduction applied to samples of the ELC(Cr) material are illustrated in Fig. IV.18. These steels were in the CHGS condition and were annealed for 4 hours at 700°C employing a mean heating rate of $2K.s^{-1}$. The results corresponding to the LC(Cr) steel are not presented here as they do not differ substantially from those of Fig. IV.18. It can be seen that the r-value increased as the deformation temperature was reduced, even when the sample deformed at 640°C only experienced a reduction of 65%.

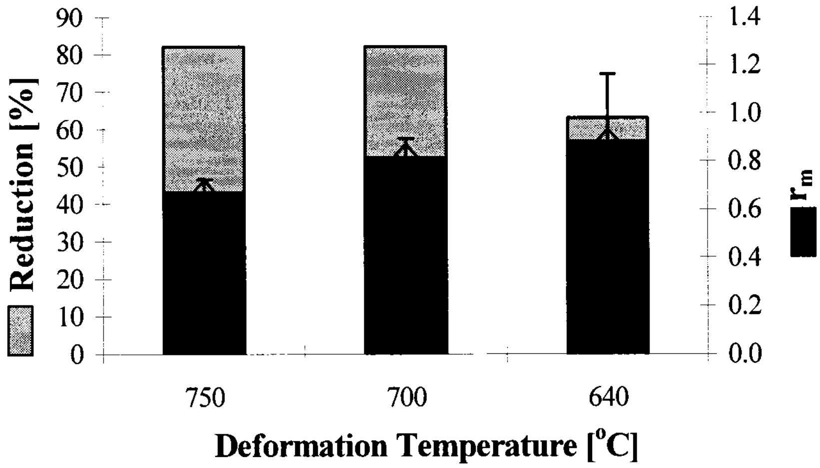

Figure. IV.18. r_m values of ELC(Cr) samples of the CHGS type, warm rolled at different temperatures and then annealed at 700°C using a heating rate of $2K.s^{-1}$.

The formability was increased when the slower heating rate of $1.5x10^{-2}K.s^{-1}$ was used for the annealing treatment, Fig. IV.19. Direct comparisons can be made with the samples deformed at 640 and 700°C of Fig. IV.18. It can be seen that the resistance to thinning of these samples increased from 0.7 and 0.8 to 1.0 and 1.2, respectively. On the other hand, that of the sample 65%WR at 640°C and cold rolled a further 40% increased from 1.2 to a final r-value of 1.3.

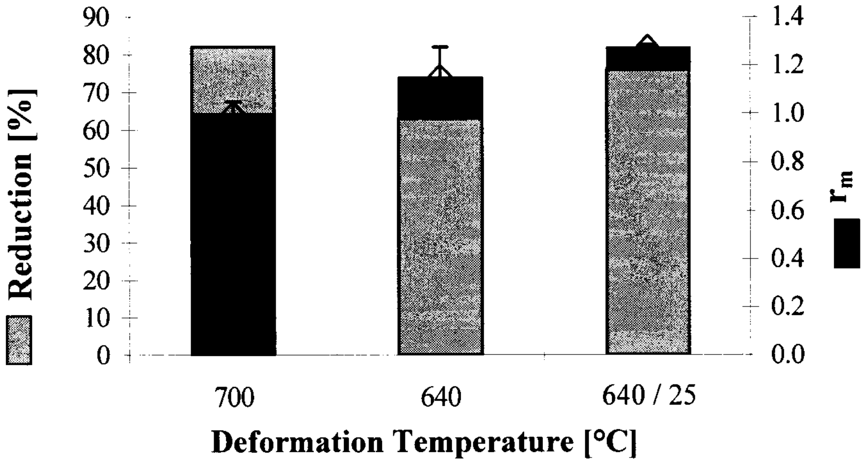

Figure. IV.19. r_m values of samples warm rolled at different temperatures and then annealed at 700°C using a heating rate of $1.5x10^{-2}Ks^{-1}$.

In order to determine the effect of initial HBGS, the r-values of samples 65% warm rolled at 640°C, both for the CHGS and FHGS conditions, and annealed at 700°C at the low heating rate of $1.5x10^{-2}K.s^{-1}$ are presented in Fig. IV.20a; those for the samples subjected to an additional 40%CR are exhibited in Fig. IV.20b.

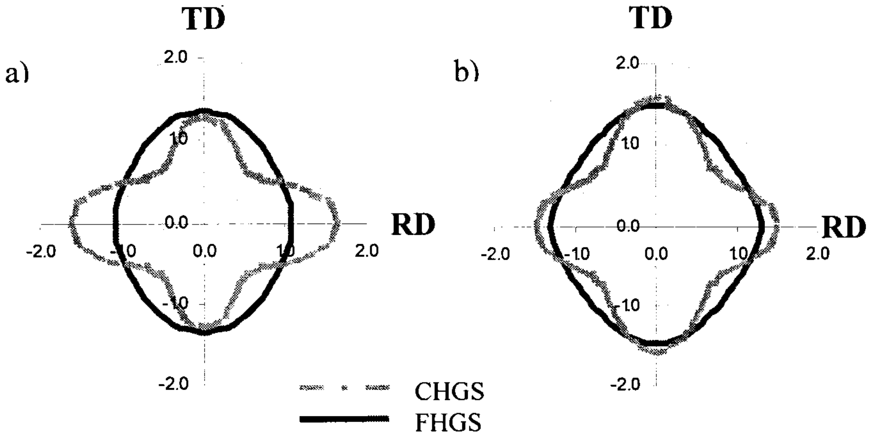

Figure. IV.20. r_m values for recrystallized samples of the CHGS and FHGS materials, calculated from the texture data: a) 65% WR at 640°C, b) 65% warm rolled at 640°C and cold reduced a further 40%. Annealed using a heating rate of $1.5x10^{-2}Ks^{-1}$.

These values were calculated from the texture data and are displayed as functions of sample direction in the sheet plane. In terms of this representation, a circular shape indicates that the r-value is the same along all directions, so that earing should not occur. The steels with the finer HBGSs display near-ellipsoidal shapes. Although the r-value is lower for these samples along the RD, the mean r-value is the same as for the CHGS samples. As the planar anisotropy, or Δr, is lower for this steel, it should have superior formability properties.

The extra cold deformation associated with Fig. IV.20b raised the mean r-value and made the distribution more homogeneous, but still maintained the approximate shape established during warm rolling. The calculated r_m and Δr values for the four samples shown in Fig. IV.20 are listed in Table IV.2.

Table IV.2. Anisotropy values for the samples of Fig. IV.20.

	WR @ 640°C		**WR @ 640°C + CR**	
Condition	r_m	Δr	r_m	Δr
FHGS	1.2	0.1	1.3	0.2
CHGS	1.2	0.6	1.3	0.5

IV.8 Microtexture Studies

The results presented in the last section provide information about the overall texture. However, in order to improve the understanding of the *mechanisms* of texture change during annealing, it is important to have more information about the nucleation process.

EBSD measurements were therefore carried out to obtain information regarding the types of nucleation site and the orientations of these nuclei. Because it is known that nucleation textures are susceptible to considerable statistical spread, large scans were run for each material, using step sizes of 0.3μm over areas of about $3x10^5\mu m^2$.

The three samples selected for EBSD analysis were those offering the highest formability. All were of the ELC(Cr) material as no important difference was observed compared to the LC(Cr) steel. Two of these were 65% warm rolled at 640°C, one each of the CHGS and FHGS materials. A third sample, additionally cold rolled and of the FHGS condition, was also selected. Finally a sample of an IF steel stabilized with titanium was chosen for comparison purposes. All samples were heat treated as described in section III.3.1. The annealing conditions are displayed in Table IV.3. An additional fully recrystallized sample was evaluated in all cases.

The α and γ fibres were subdivided into the main components presented in Table IV.4. The calculations were made using a 15° spread around each main component; all others outside these ranges were considered as part of the "random" population. A graphical description of how these components were measured is presented in Fig. IV.21.

Table IV.3 Samples of the ELC(Cr) steel selected for EBSD analysis.

Sample	Recrystallization Percentage					
65%WR@640°C - CHGS	6	17	56	80	100	100A
65%WR@640°C - FHGS	8	24	50	77	100	100A
65%WR+40%CR - FHGS	8	18	35	70	100	100A
IF 65%WR@640°C	9	19	-	65	100	100A

100 A = fully annealed 4hr at 700°C

Table IV.4 Subdivision of the main α and γ fibres.

α fibre	$\alpha_c = \{001\}<110>$	$\alpha_1 = \{112\}<110>$	$\alpha_2 = \{hkl\}<110>$
γ fibre	$\gamma_1 = \{111\}<110>$	$\gamma_2 = \{111\}<112>$	$\gamma_3 = \{111\}<hkl>$

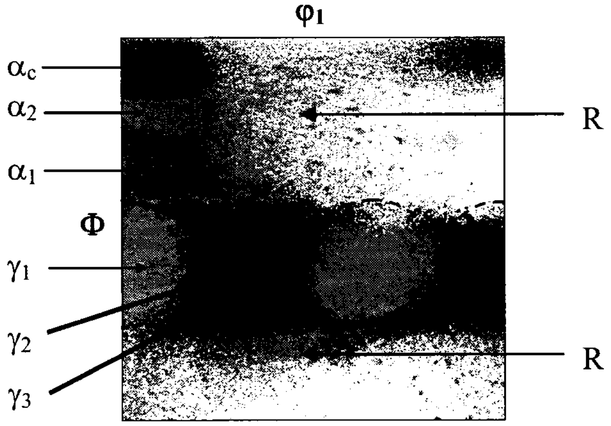

Figure. 4.21. Graphical representation of the definitions of the main components presented in Table IV.4.

The results of this section are organized into three main groups. The first concerns the characteristics of the substructure in terms of the degree of misorientation within the deformed grains. The second involves the preferred nucleation sites and the volume fraction of each type of nucleus. The evolution of texture and the growth rate of each main orientation during recrystallization are presented in the third.

IV.8.1 Substructure

The misorientation profiles within selected deformed α, γ and R grains were measured for the four conditions specified in Table IV.3. The scans were carried out along the lines marked on Figs. IV.22 to IV.25. These figures (and others not shown) correspond to the early stages of recrystallization and each orientation component is identified according to the color code shown below each map. The misorientation profiles were measured for 3 or 4 grains of each component. Both point-to-point and point-to-origin profiles were assessed. The first gives information about the general level of the misorientation and the second allows the location of a possible nucleus to be recognized. The latter can be distinguished in the point-to-origin misorientation profile as a *short* region of fairly large semi-constant misorientation.

The results for the 65%WR-CHGS material are presented in Fig. IV.26. It is clear that deformed γ grains have the highest degree of point-to-point misorientation, followed by the randomly oriented grains and finally by the α grains, whose degree of misorientation is almost insignificant. In the point-to-origin misorientation profiles of Fig IV.27, several regions of semi-constant misorientation can be seen, which translate into a high number of potentially successful nuclei.

In the case of the 65%WR-FHGS material, see Fig. IV.28, the α, γ and R components display similar behaviours. However, the degree of point-to-point misorientation appears to have increased because of the refinement of the hot band grain size. This is represented by a larger number of *peaks*. The effect of this increase is reflected in the point-to-origin profiles of Fig. IV.29 by the increased number of possible nucleation sites.

With regard to the α component, the drastic change observed at a distance of approximately 20μm in the case of $8\alpha_c$ (Fig. IV.29) appears to be due to the increase in substructure content near a grain boundary. In the case of $4\alpha_c$, an additional contribution may arise from narrowing of the deformed grain.

The degree of misorientation increased when a further 40% cold rolling reduction was applied. Some results for the 65%WR+40%CR-FHGS material, which are illustrated in Figs. IV.30 and IV.31, exhibit still higher degrees of misorientation, principally with regard to the γ and R components. In contrast, the α components displayed little change.

In the case of the IF steel, the level of misorientation is approximately 1.5 times higher than in the WR+CR specimen; the number of possible nucleation sites also increases in the point-to-origin graph. This can be seen in Figs. IV.32 and IV.33.

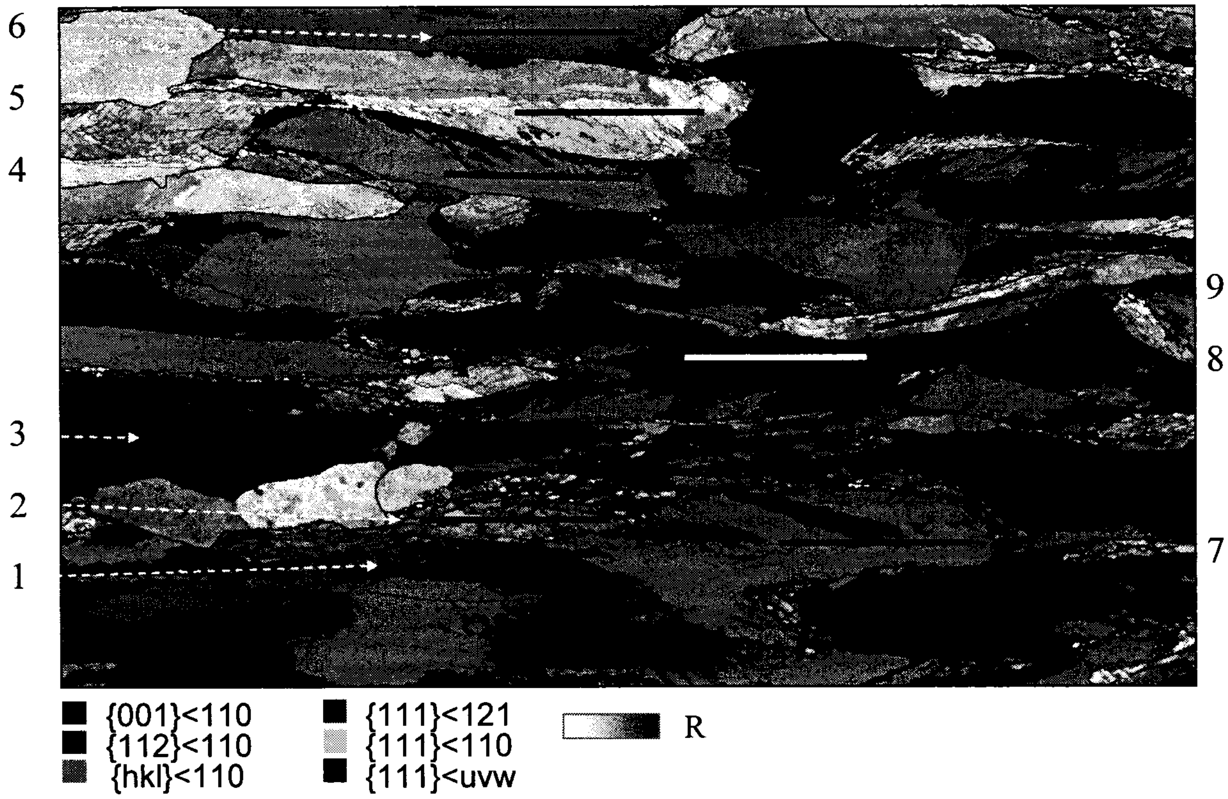

Figure IV.22. Orientation map at 6% recrystallization of the CHGS ELC(Cr) steel WR 65% at 640°C. The α, γ and R components contained within a spread of 15° around each ideal orientation are illustrated according to the color code. The horizontal lines and numbers at the sides of the map correspond to grains in which misorientation profiles were measured.

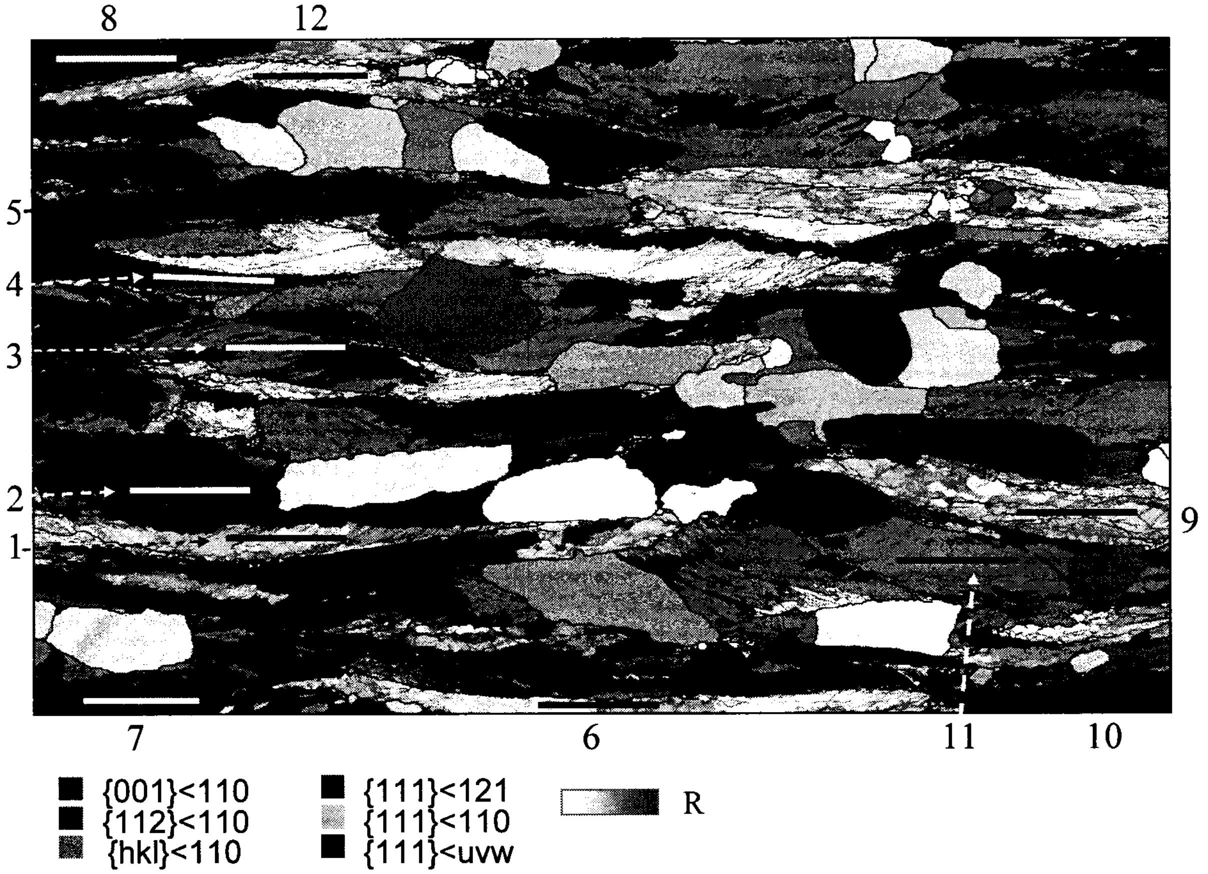

Figure IV.23. Orientation map at 8% recrystallization of the FHGS ELC(Cr) steel WR 65% at 640°C. The α, γ and R components contained within a spread of 15° around each ideal orientation are illustrated according to the color code. The horizontal lines and numbers at the sides of the map correspond to grains in which misorientation profiles were measured.

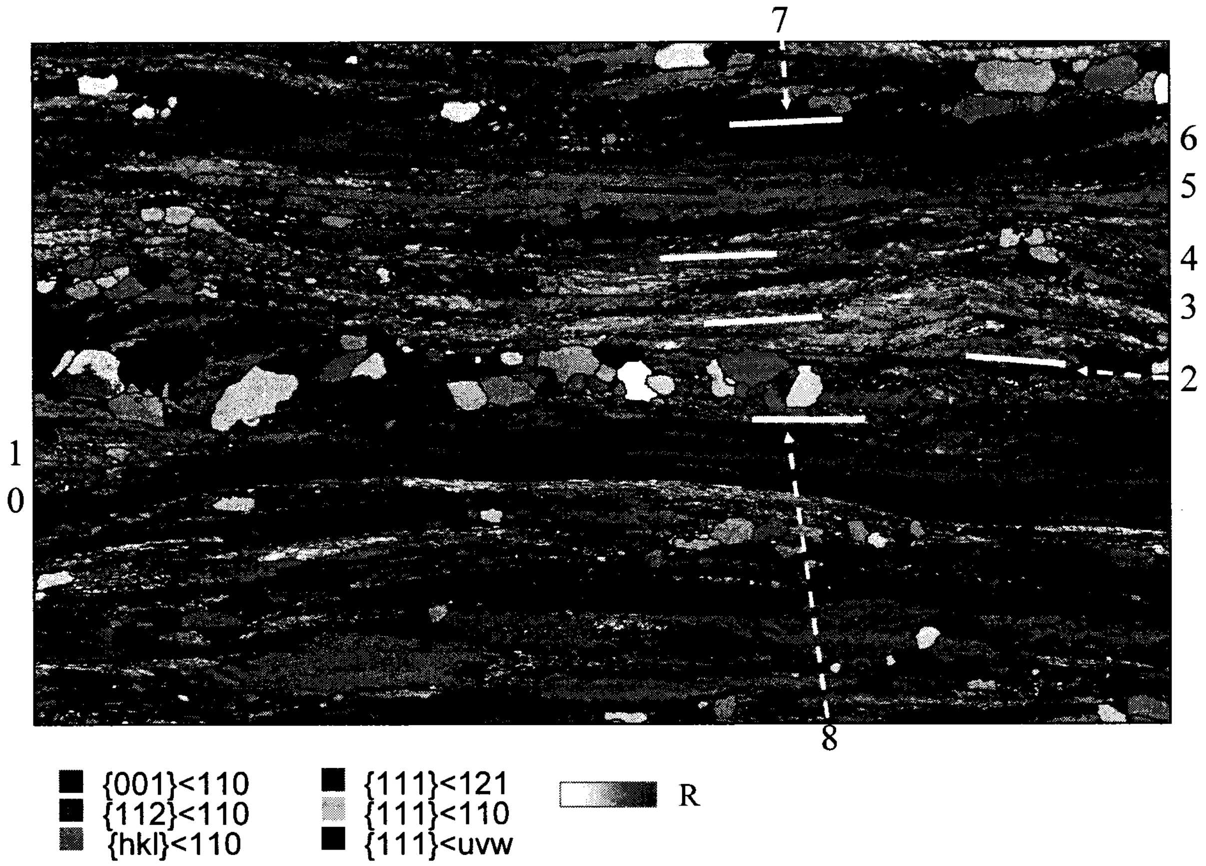

Figure IV.24. Orientation map at 8% recrystallization of the FHGS ELC(Cr) steel WR 65% at 640°C and then cold rolled a further 40%. The α, γ and R components contained within a spread of 15° around each ideal orientation are illustrated according to the color code. The horizontal lines and numbers at the sides of the map correspond to grains in which misorientation profiles were measured.

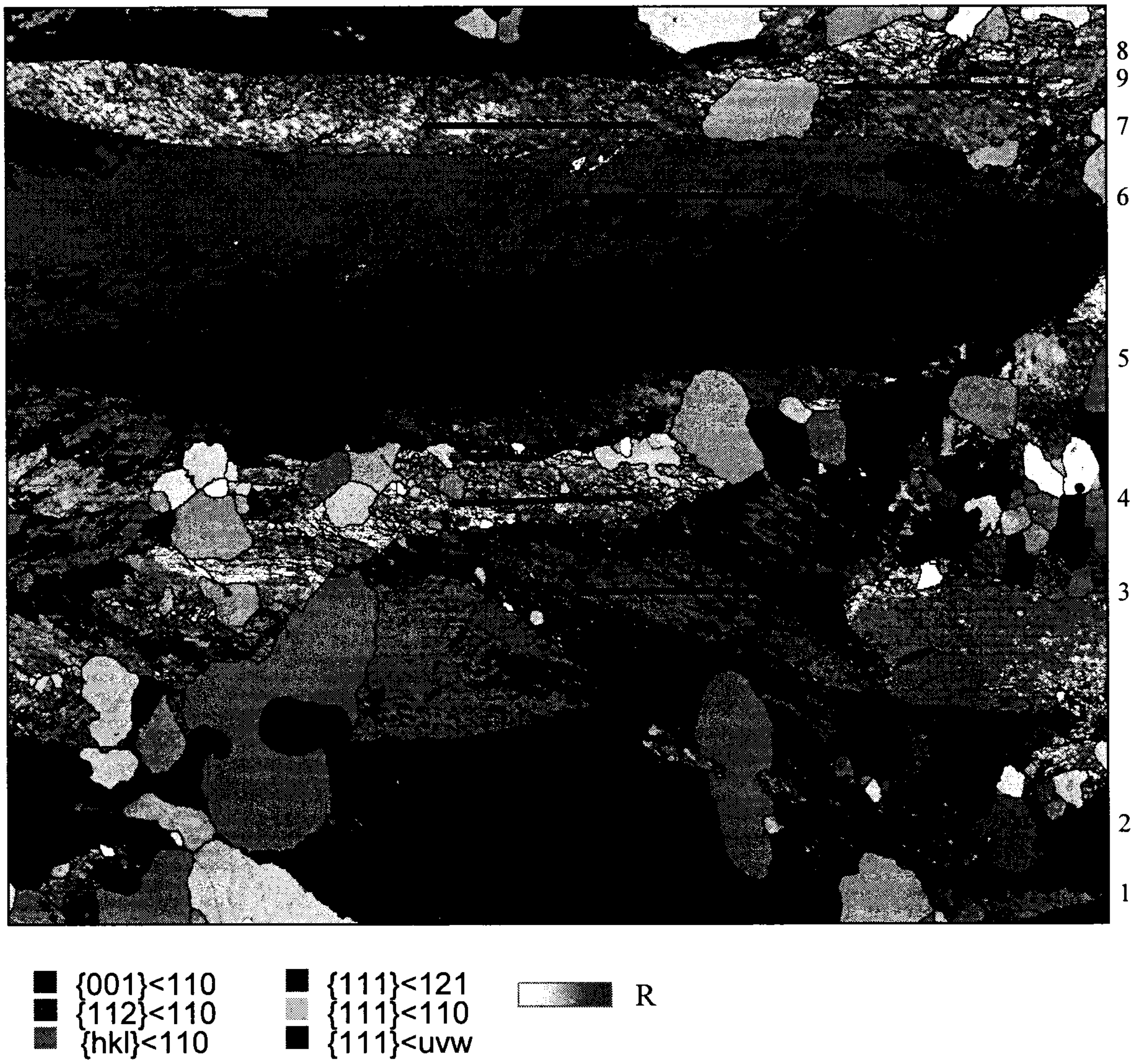

Figure IV.25. Orientation map at 6% recrystallization of the CHGS IF steel WR 65% at 640°C. The α, γ and R components contained within a spread of 15° around each ideal orientation are illustrated according to the color code. The horizontal lines and numbers at the sides of the map correspond to grains in which misorientation profiles were measured.

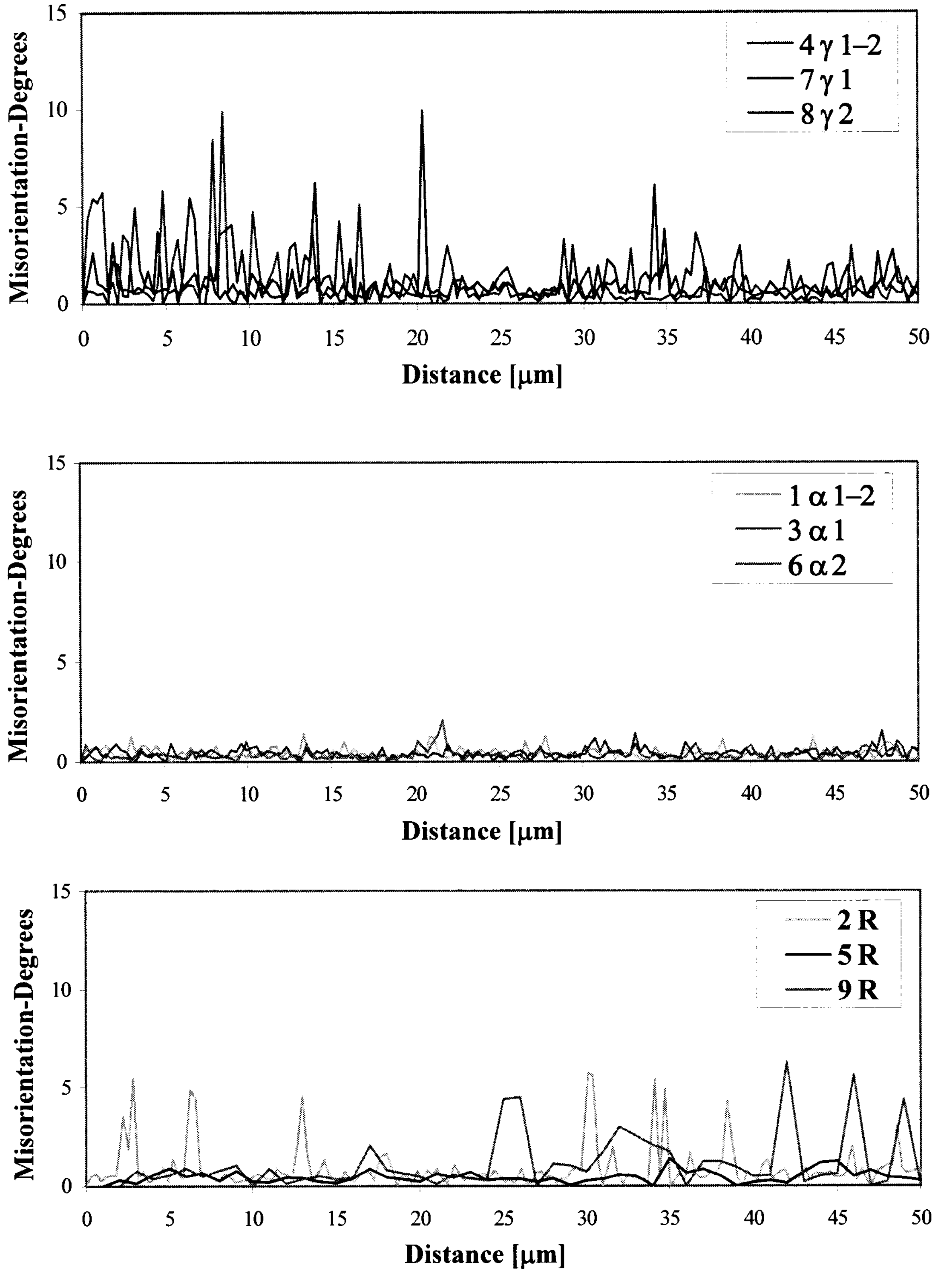

Figure IV.26. Misorientation profiles for the CHGS ELC(Cr) steel WR 65% at 640°C; measured along the marked lines in Fig. IV.22. Point-to-point data.

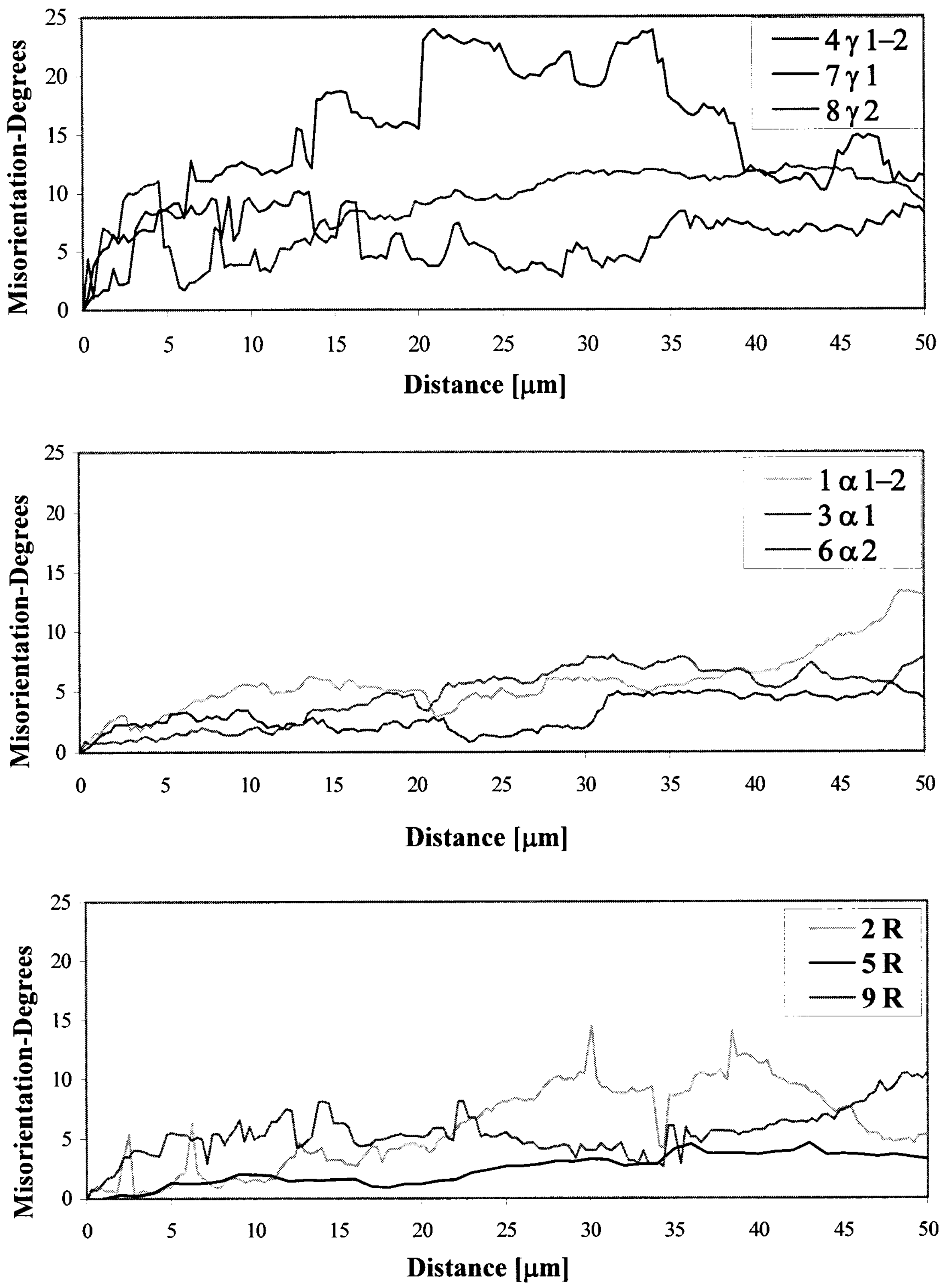

Figure IV.27. Misorientation profiles for the CHGS ELC(Cr) steel WR 65% at 640°C; measured along the marked lines in Fig. IV.22. Point-to-origin data.

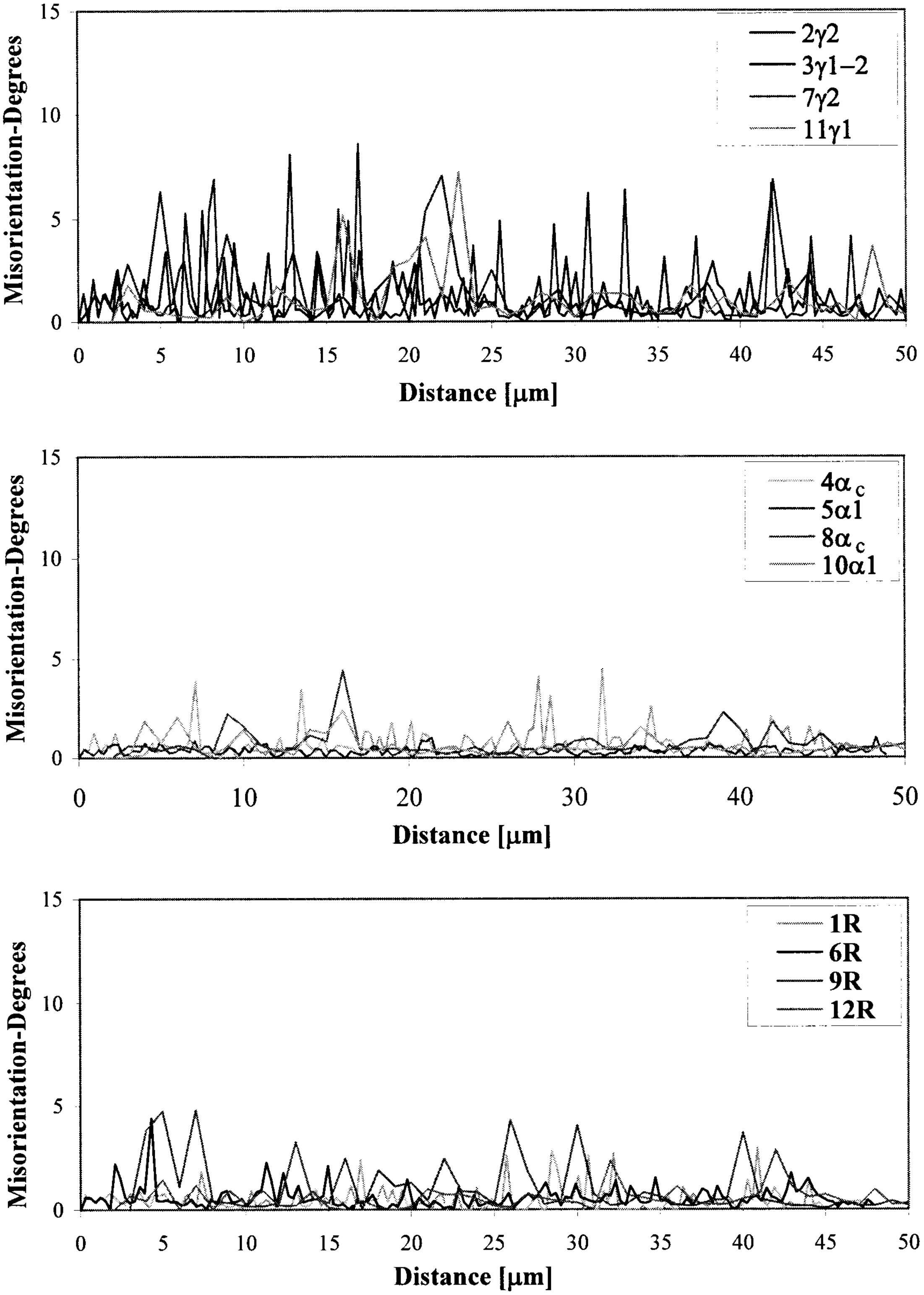

Figure IV.28. Misorientation profiles for the FHGS ELC(Cr) steel WR 65% at 640°C; measured along the marked lines in Fig. IV.23. Point-to-point data.

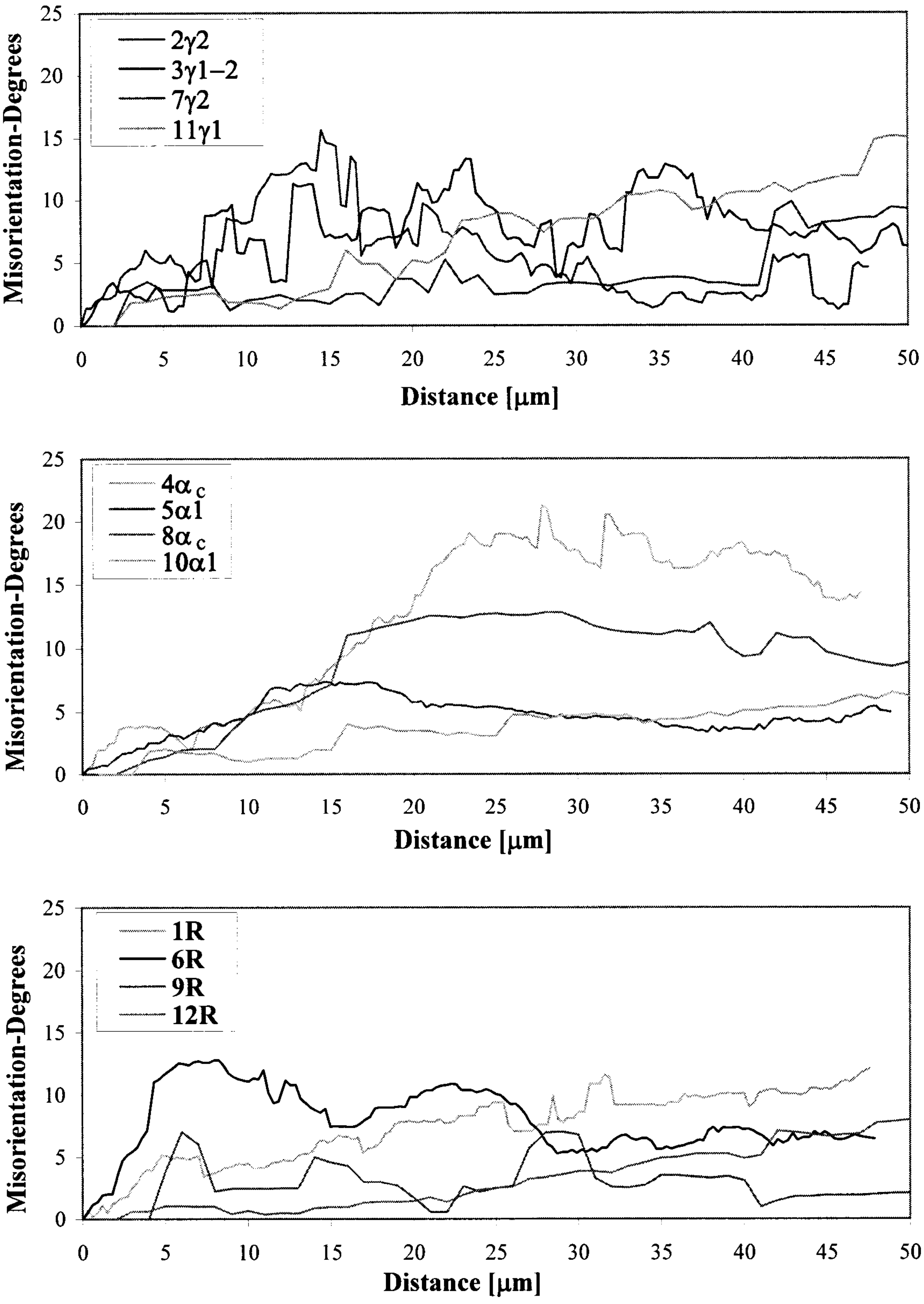

Figure IV.29. Misorientation profiles for the FHGS ELC(Cr) steel WR 65% at 640°C; measured along the marked lines in Fig. IV.23. Point-to-origin data.

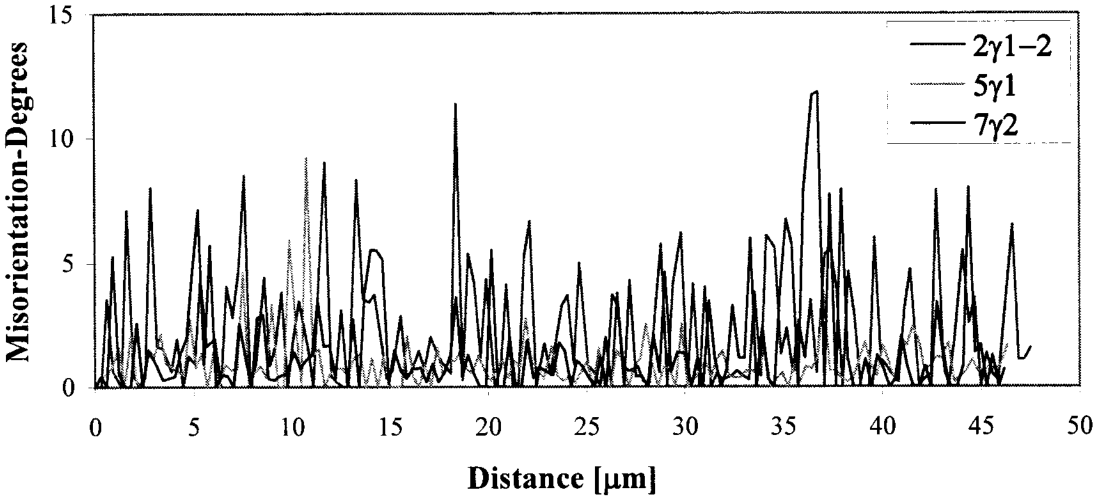

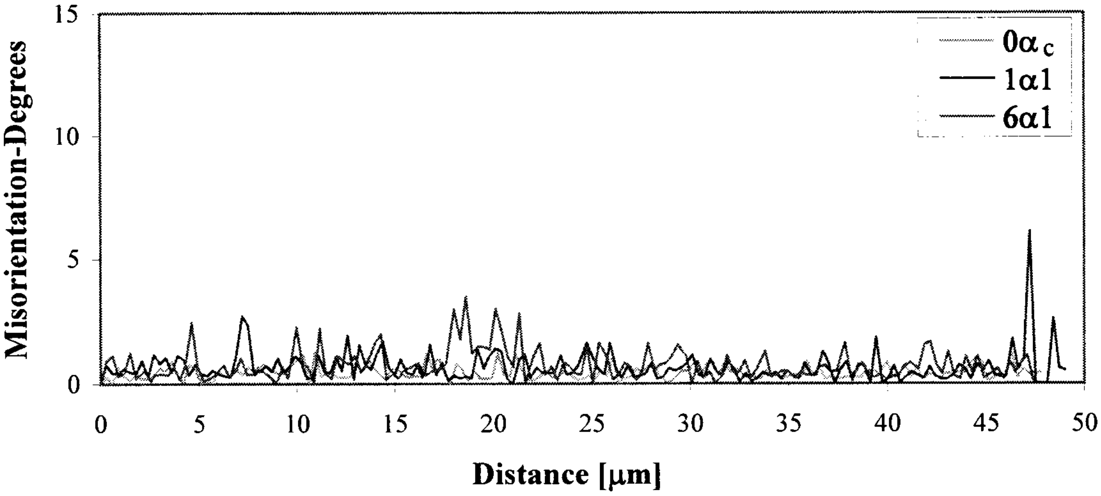

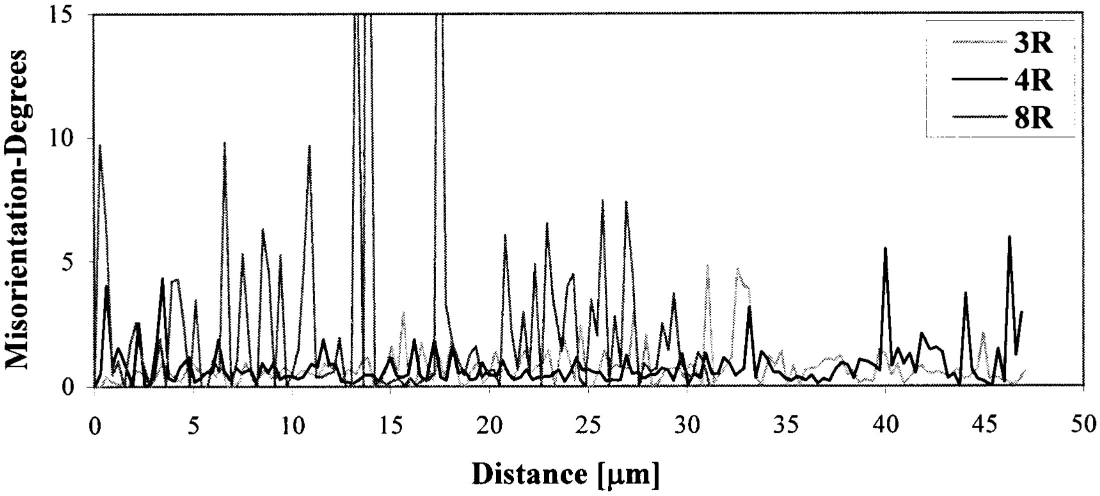

Figure IV.30. Misorientation profiles for the FHGS ELC(Cr) steel WR 65% + CR 40% at 640°C; measured along the marked lines in Fig. IV.24. Point-to-point data.

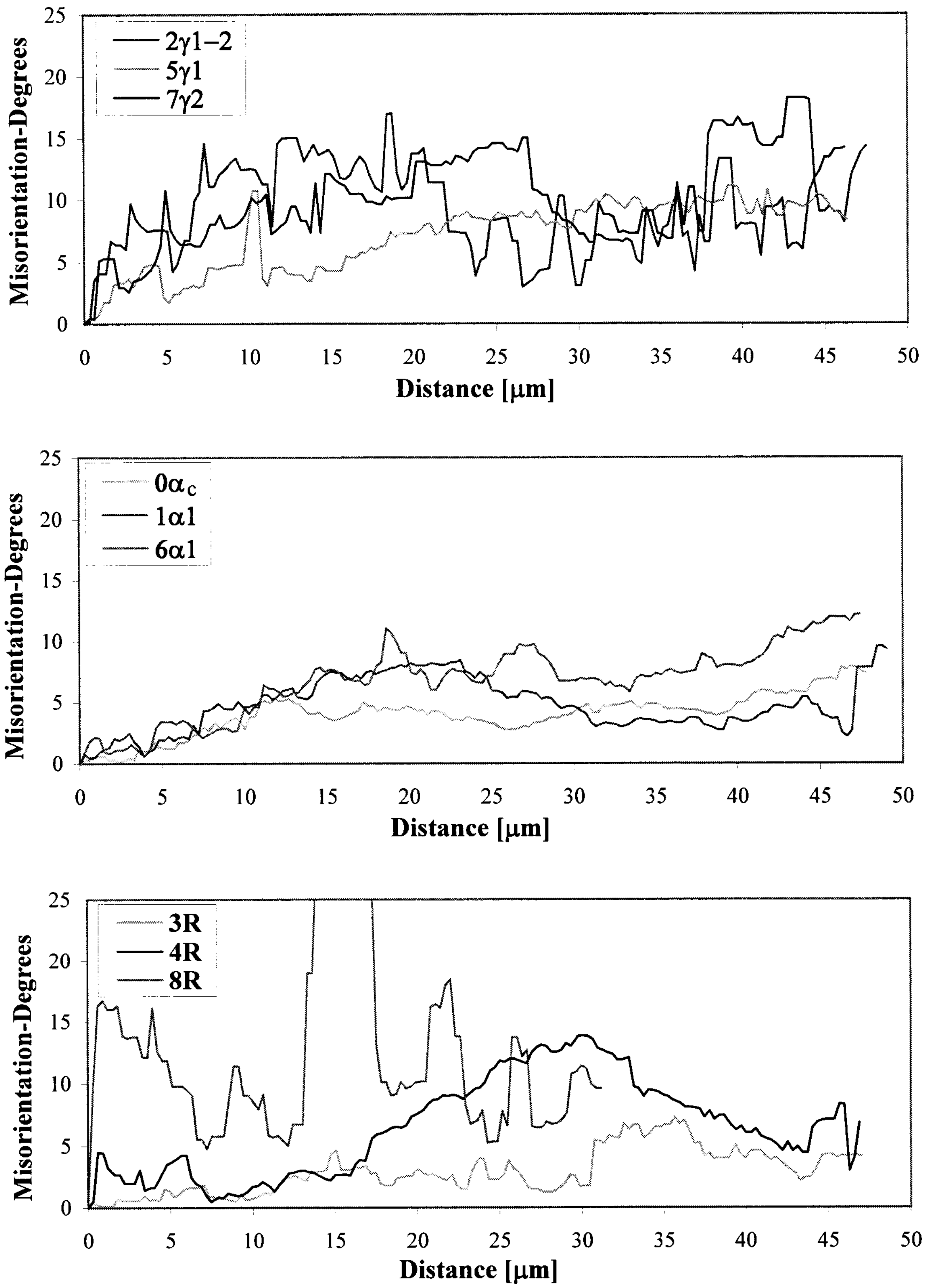

Figure IV.31. Misorientation profiles for the FHGS ELC(Cr) steel WR 65% + CR 40% at 640°C; measured along the marked lines in Fig. IV.24. Point-to-origin data.

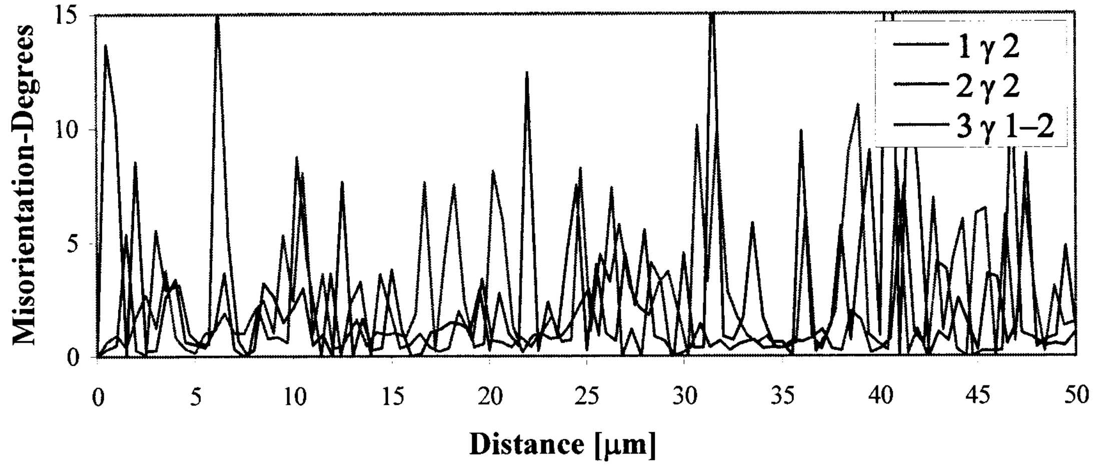

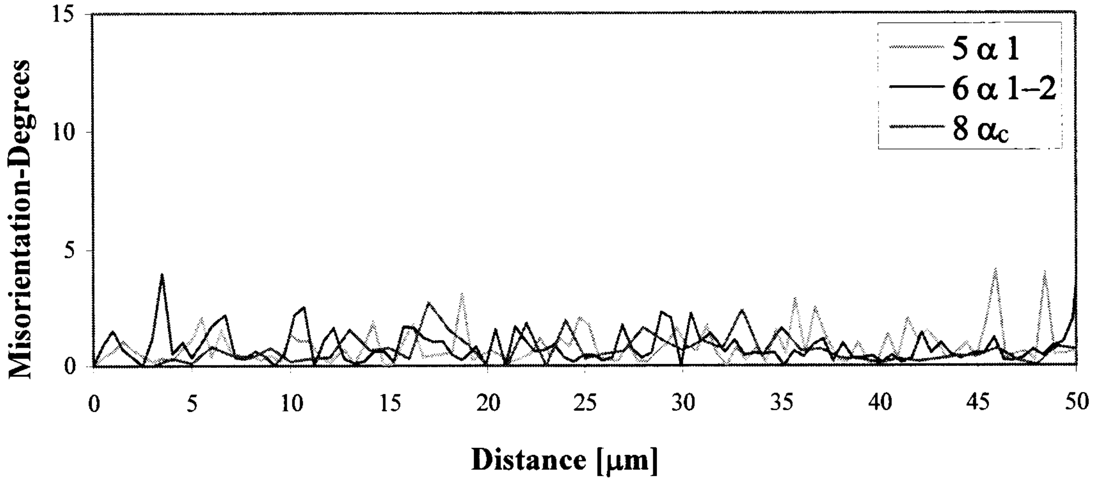

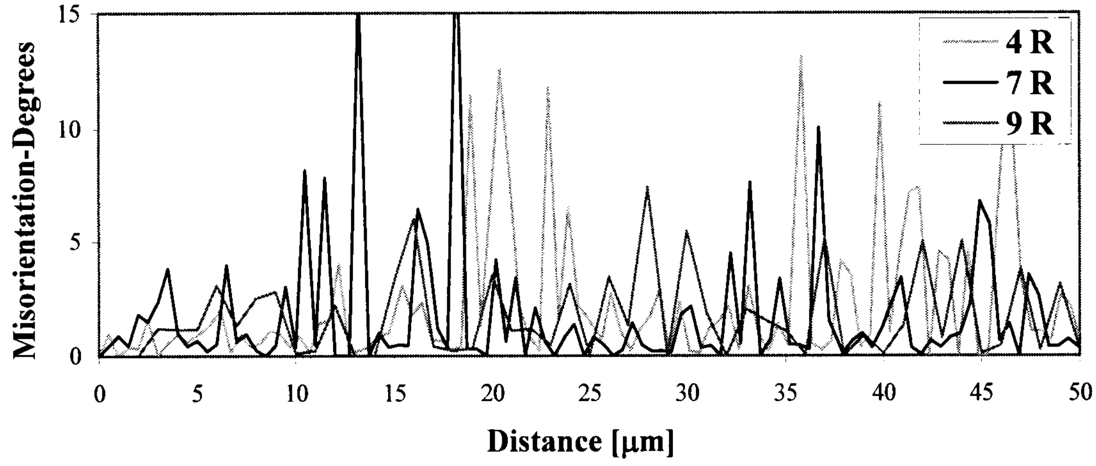

Figure IV.32. Misorientation profiles for the IF steel WR 65% at 640°C; measured along the marked lines in Fig. IV.25. Point-to-point data.

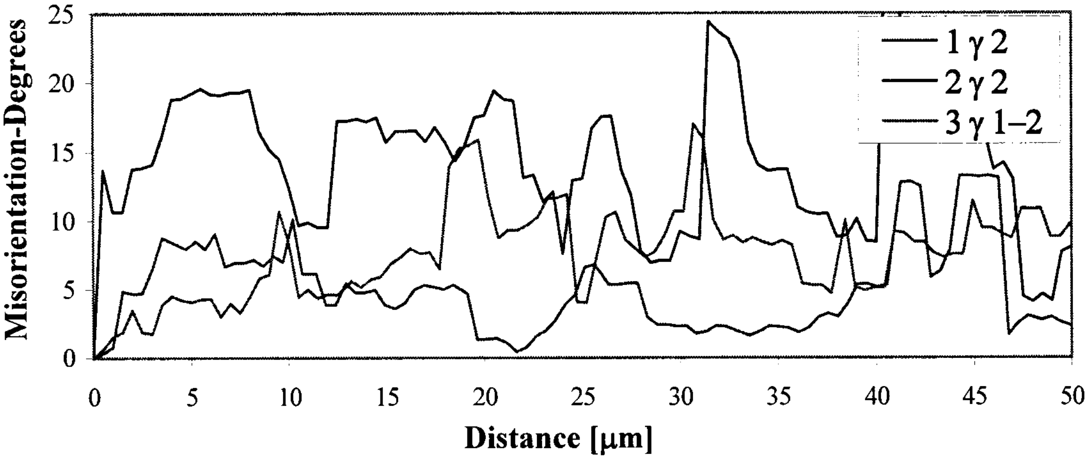

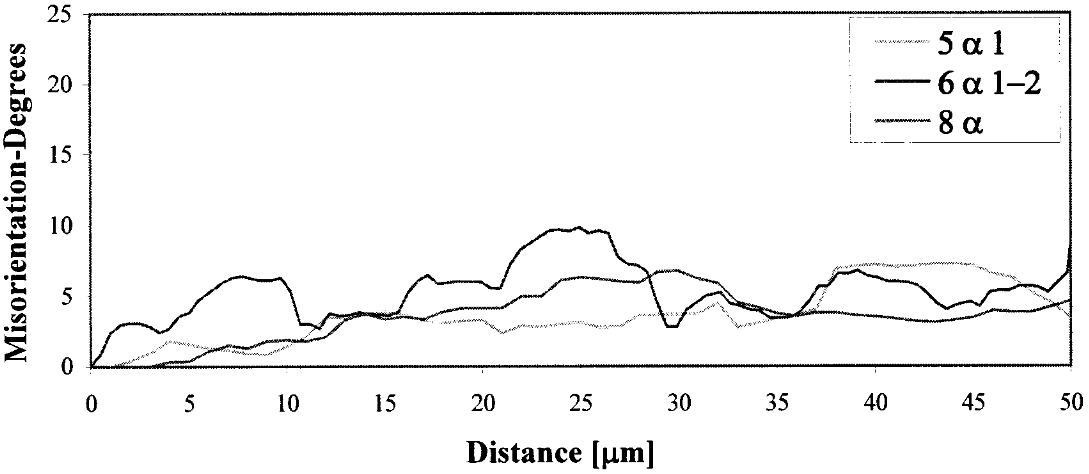

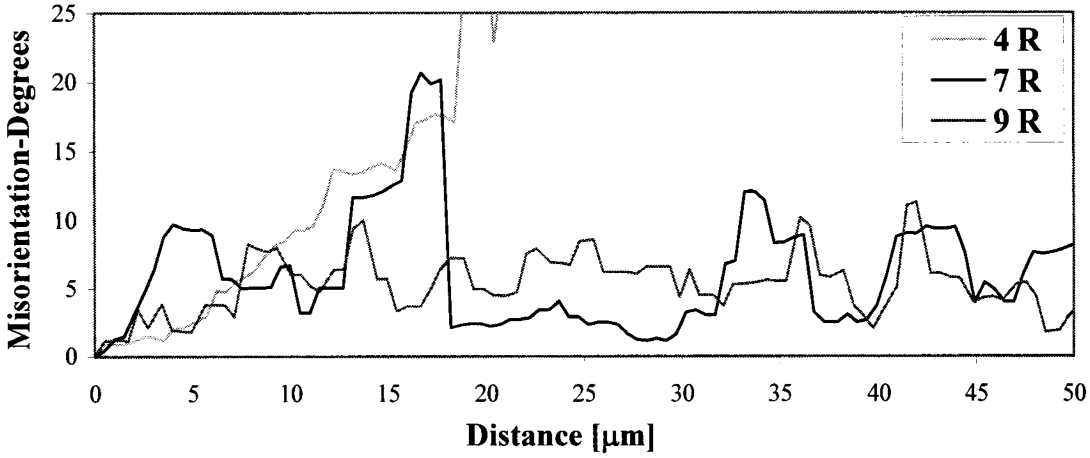

Figure IV.33. Misorientation profiles for the IF steel WR 65% at 640°C; measured along the marked lines in Fig. IV.25. Point-to-origin data.

IV.8.2 Nucleation

A part of the scanned area of the 65%WR-FHGS sample is illustrated in Fig. IV.34. In this figure, a colour code is used to distinguish the α , γ and randomly oriented (R) grains. This figure provides examples of shear band and grain boundary nucleation, which are labelled here as SBN and GBN. It is of interest to note that γ grains have nucleated and grown in the interiors of the γ-type grains as well as at their boundaries. The latter observation also applies to the random nuclei; furthermore, some of these grains grow into and consume the deformed γ grains. The quantities and locations of each type of nucleus are presented next.

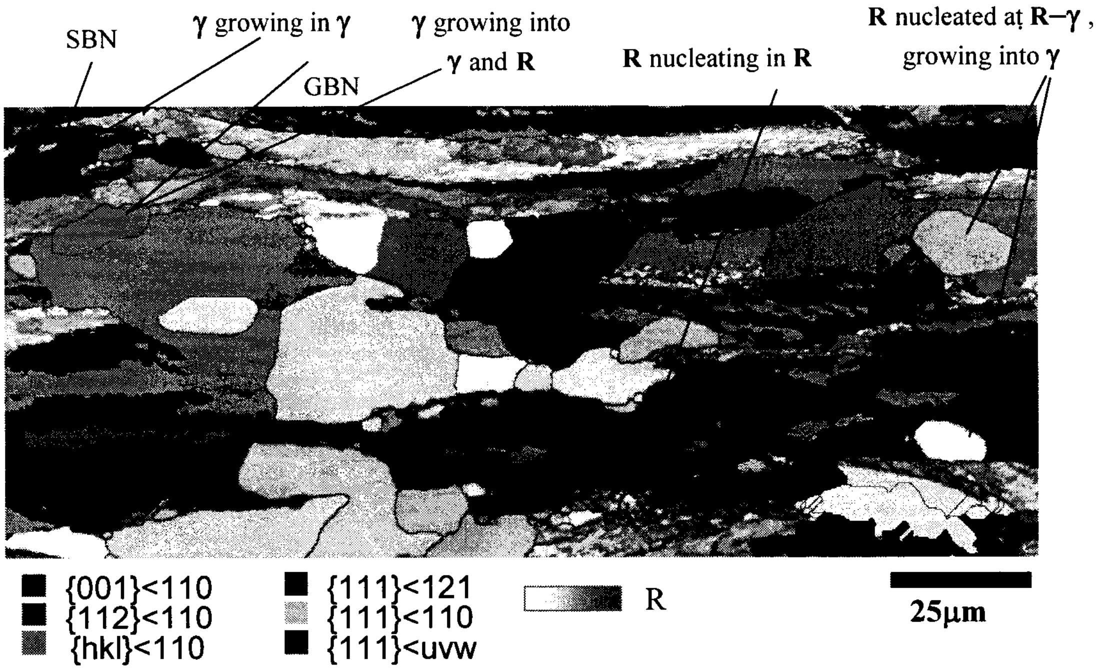

Figure IV.34. Nucleation map for the α-fibre, γ-fibre and random orientations. 18μm HBGS sample; the orientation spread for each orientation is 15°.

The distribution of grain boundary (GBN) and grain interior (GIN) nucleation sites in samples in the early stages of recrystallization listed in Table IV.3 is illustrated in Fig. IV.35.

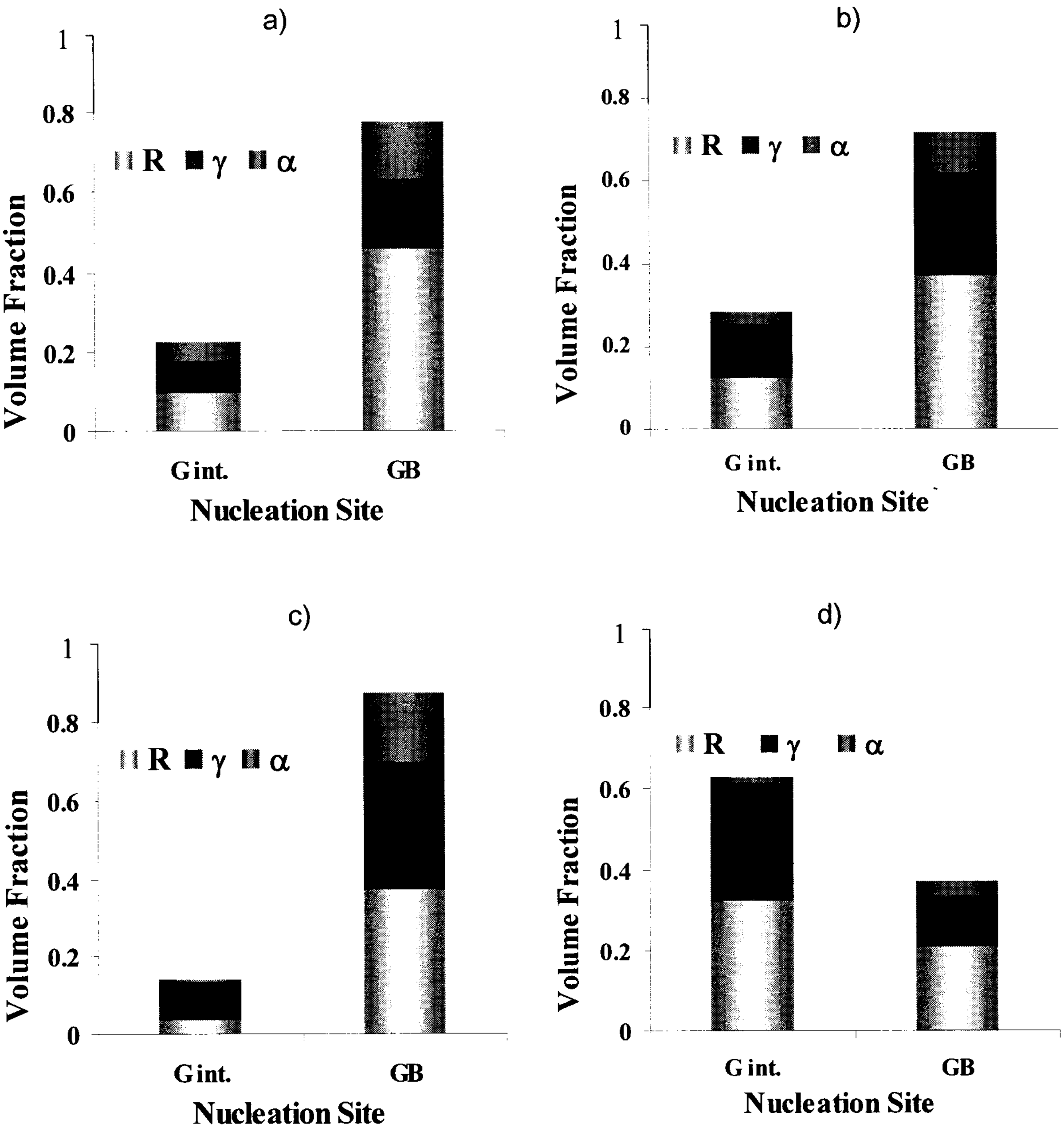

Figure IV.35. Nucleation site distributions for the α, γ and random orientations, calculated from EBSD measurements made on materials in the early stages of recrystallization and presented in Figures IV.22 to IV.25: a) 65%WR-CHGS, b) 65%WR-FHGS, c) 65%WR+40%CR-FHGS and d) IF-steel.

The 65%WR-CHGS sample exhibited a predominance of GBN nucleation with up to 75% of the nuclei found at this location, Fig. IV.35a. When the hot band grain size (HBGS) is refined as for the 65%WR-FHGS specimen in Fig. IV.35b, a slightly increase in GIN nucleation is observed (which may not be statistically significant). On the other hand, the most important change concerned the volume fraction of the γ component, which increased in both the GBN and GIN categories.

The further cold rolling of the initially warm rolled sample, which is the case of the 65%WR+40%CR-FHGS material presented in Fig. IV.35c, favours GBN nucleation, raising it to approximately 90%. By contrast, nucleation of the α component was totally inhibited at the GIN sites. However, it increased at the GBN sites, as well as at the γ orientations, both at the expense of the randomly oriented grains.

The behaviour of the IF steel differed totally from that of the ELC(Cr) material. In this case, as illustrated in Fig. IV.35d, GIN nucleation played the major role, yielding a volume fraction of 0.65 and a larger γ/R ratio. Another important characteristic to note was the small amount of α at both types of nucleation site.

IV.8.2.1 Nucleation at grain boundaries

The distribution of α, γ, and R nuclei at boundaries of the deformed grains is presented in Fig. IV.36. Results for the 65%WR-CHGS sample illustrated in Fig. IV.36a indicate that γ grains can nucleate at all types of boundary except at α–α. On the other hand, the R grains nucleated mostly at R-R, but also at γ–γ, γ–α and γ-R. A minor presence was noted for the α components, which also appear at all but α–α boundaries. What is clear from these results is the high volume fraction of R orientations and their ability to nucleate at most types of grain boundary.

The effect of a refinement in the HBGS is displayed in Fig. IV.36b, which corresponds to a 65%WR-FHGS sample. Here, a redistribution of nucleation preferences is observed. It can be seen that the γ orientations increased their volume fractions at the γ-

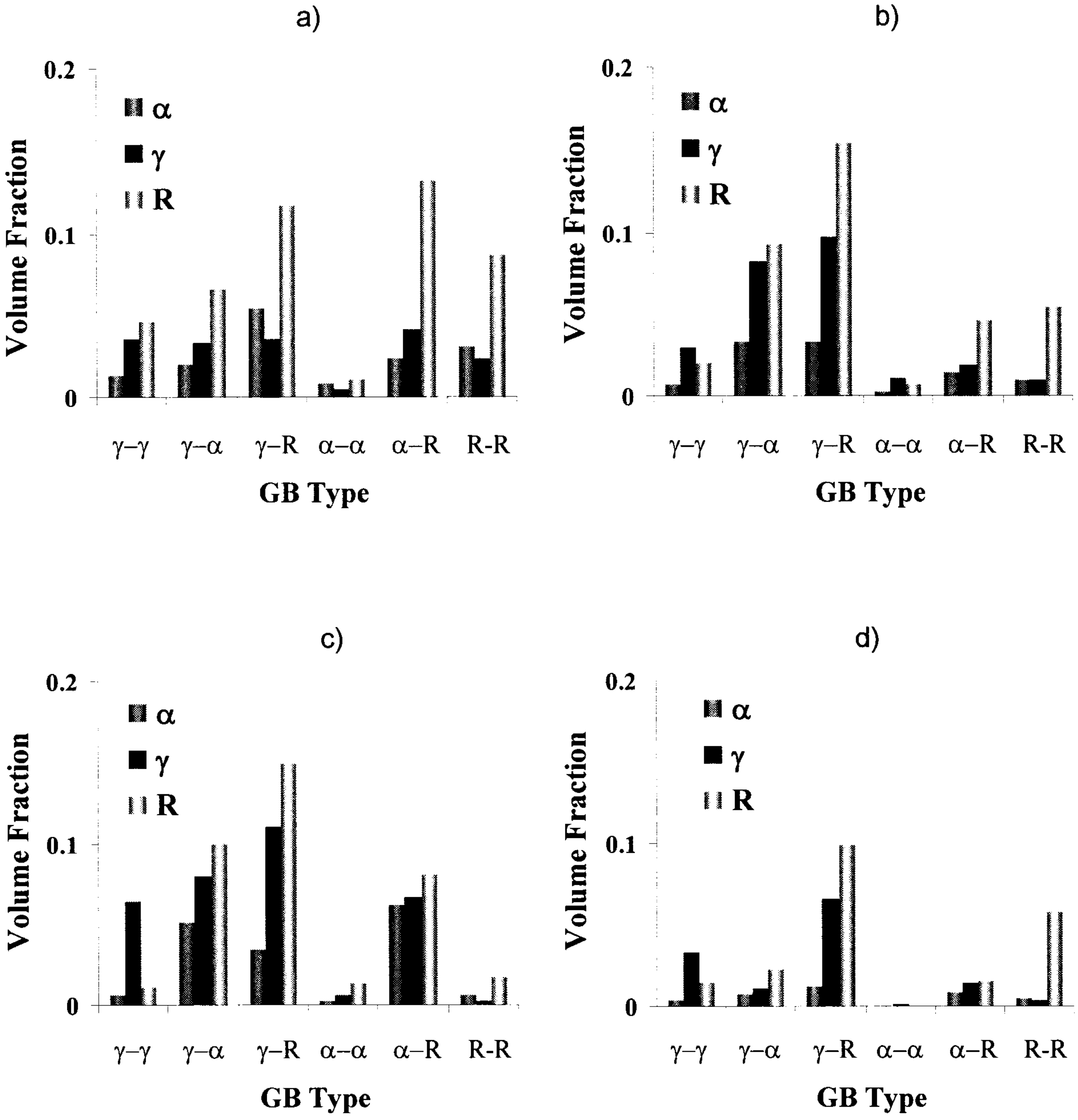

Figure IV.36. Distribution of α, γ and R nuclei formed at various types of grain boundary; calculated from EBSD measurements carried out on materials in the early stages of recrystallization and presented in Figures IV.22 to IV.25: a) 65%WR-CHGS, b) 65%WR-FHGS, c) 65%WR+40%CR-FHGS, and d) IF-steel.

γ, γ-α and γ-R type boundaries. A similar but less significant change was displayed by the R nuclei, while the α grains experienced a decrease in their overall volume fraction.

Fig. IV.36c illustrates the increase in the volume fraction of γ at γ-type boundaries as an effect of the additional cold rolling. α nucleation was also favoured at γ-α, γ-R and α–α boundaries. In the case of the R orientations, there was a decrease in the volume fraction at R-R and an increase at α-R, the latter most likely due to the increase in stored energy in the deformed α grains.

The IF steel, Fig. IV.36d, contained less grain boundary nuclei than any of the three experimental steels. Most of the GB γ nucleation occurred at the γ–γ and γ-R boundaries. In a similar manner, R nucleation occurred at the γ-R and R-R boundaries. This confirmed that γ-type boundaries promote γ nucleation.

Nucleation at GBs was also analyzed in detail for the main γ fibre orientations. These are represented here by {111}<110>, {111}<112> and γ_3, which comprises all the other γ orientations. For the 65%WR-CHGS sample, Fig. IV.37a, not one of these components was favoured, while in the case of the 65%WR-FHGS material, the {111}<112> orientation was twice as common as the {111}<110>, see Fig. IV.37b. In the case of the specimen subjected to additional cold rolling, 65%WR+40%CR-FHGS, the volume fraction of {111}<110> and {111}<112> increased with respect to γ_3. Nevertheless, {111}<112> was higher again, Fig IV.37c. Compared to the ELC(Cr) material, the volume fraction of γ components nucleated at GBN sites is much lower for the IF steel, Fig. IV.37d, and no significant preference was observed between the three types of site.

In the above, the importance of the γ grain boundaries for the nucleation of γ grains was particularly clear, as up to 75% of the γ nuclei were formed at γ–γ, γ-R and γ–α boundaries.

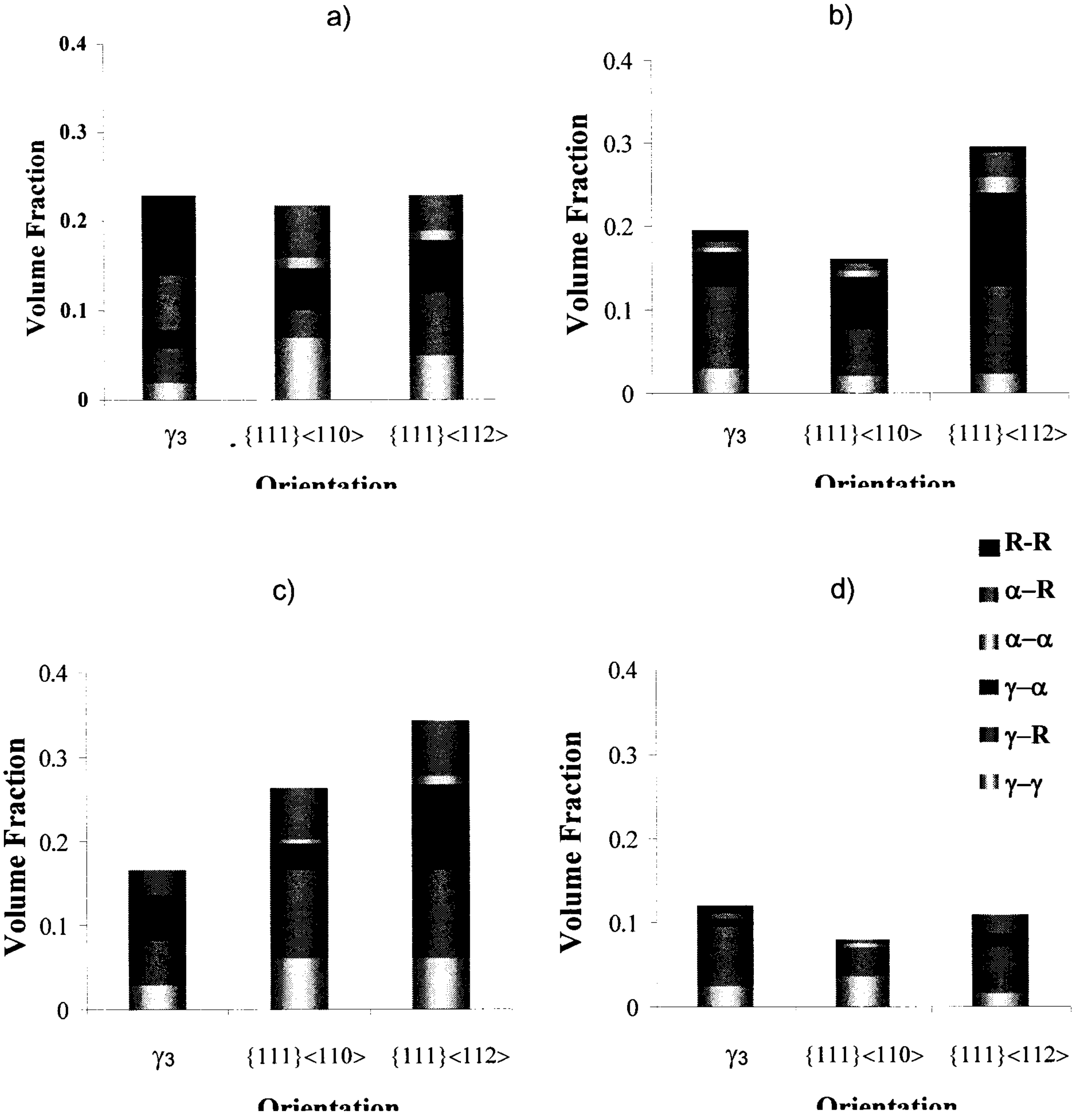

Figure IV.37. Distribution of the {111}<110>, {111}<112> and γ3 nuclei formed at various types of grain boundary. The volume fractions were calculated from EBSD measurements carried out on materials in the early stages of recrystallization and presented in Figures IV.22 to IV.25: a) 65%WR-CHGS, b) 65%WR-FHGS, c) 65%WR+40%CR-FHGS and d) IF-steel.

IV.8.2.2 In-grain nucleation

The nucleation behaviours in the interiors of the deformed grains of the ELC(Cr) material were similar for the three sets of processing conditions, Fig. IV.38a-c. It was observed that the γ and R components were the principal orientations nucleating in the grain interiors. It was also seen that deformed γ grains lead principally to γ nuclei, but also to some R nuclei. Furthermore, the deformed R grains lead principally to R nuclei.

The number of γ components nucleating in deformed γ grains increased when the HBGS was refined. Conversely, the fraction of R grains nucleating in γ decreased while it increased within the deformed R grains. When additional cold rolling was provided, the volume fraction of *in-grain* nucleation as a whole decreased. Nevertheless, the ratio of the γ fibre to all the other orientations increased.

The results for the IF steel, presented in Fig. IV.38d, followed the same behaviour with γ and R orientations nucleating within the deformed γ grains. In a similar manner, the R orientations led to R nuclei. On the other hand, the volume fractions of the γ components were higher.

The results for the separate nucleation of {111}<110> and {111}<112> are illustrated in Fig. IV.39. It can be seen that the in-grain nucleation of the three γ components took place mainly within deformed γ grains. When the HBGS was refined, the volume fraction of {111}<112> was increased. On the other hand, additional cold rolling caused a decrease in all the in-grain orientations. In the case of the IF steel, the behaviour is in sharp contrast to that of the ELC(Cr) steel: up to 65% of all the γ orientations nucleate *within* deformed γ grains. It was also observed that the {111}<112> appeared twice as frequently as the {111}<110> and that the volume fraction of the γ_3 components was as high as that of the former.

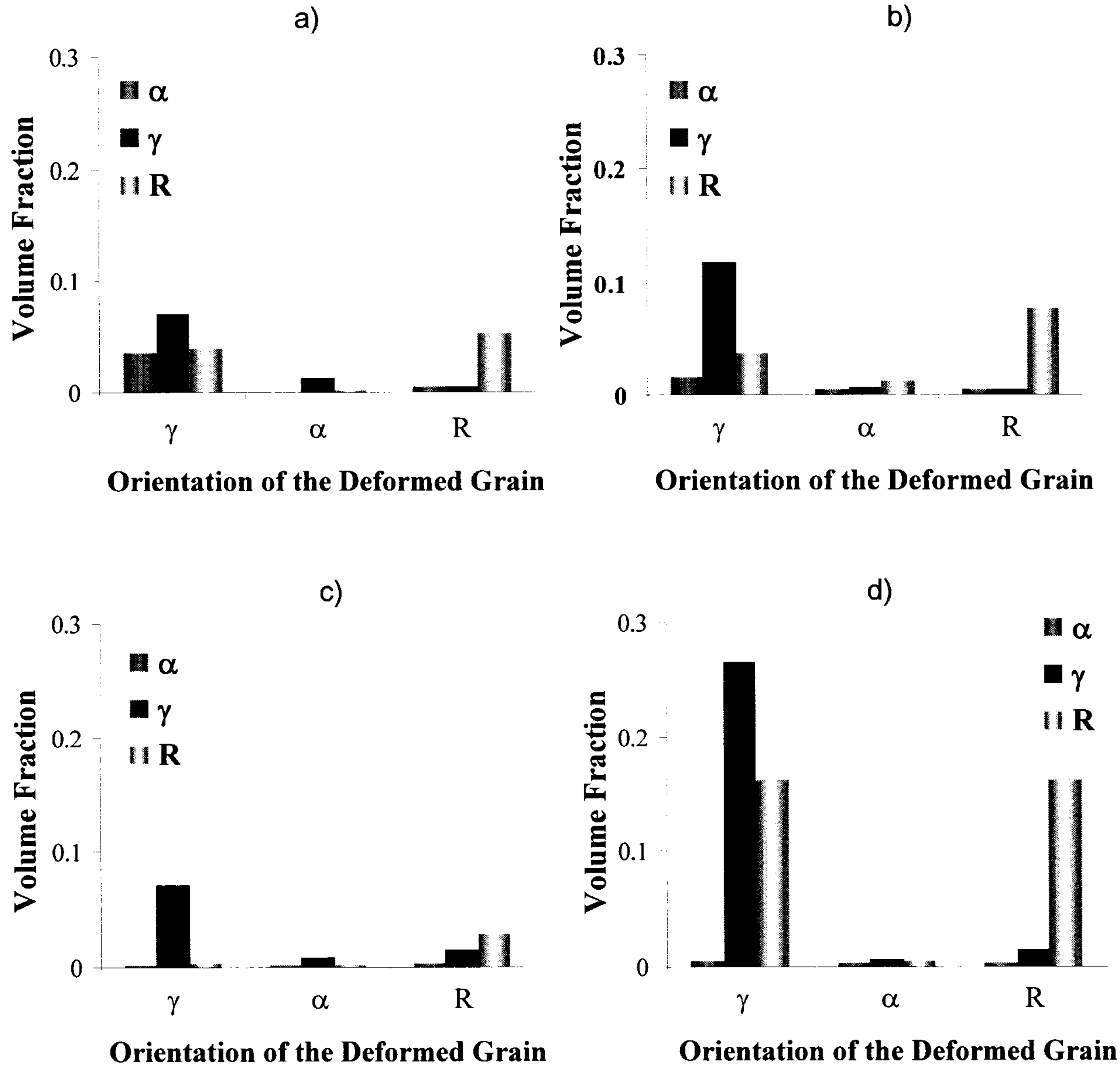

Figure IV.38. Distribution of α, γ and R nuclei within deformed grains. The volume fractions were calculated from EBSD measurements of the materials in the early stages of recrystallization and presented in Figures IV.22 to IV.25: a) 65%WR-CHGS, b) 65%WR-FHGS, c) 65%WR+40%CR-FHGS and d) IF-steel.

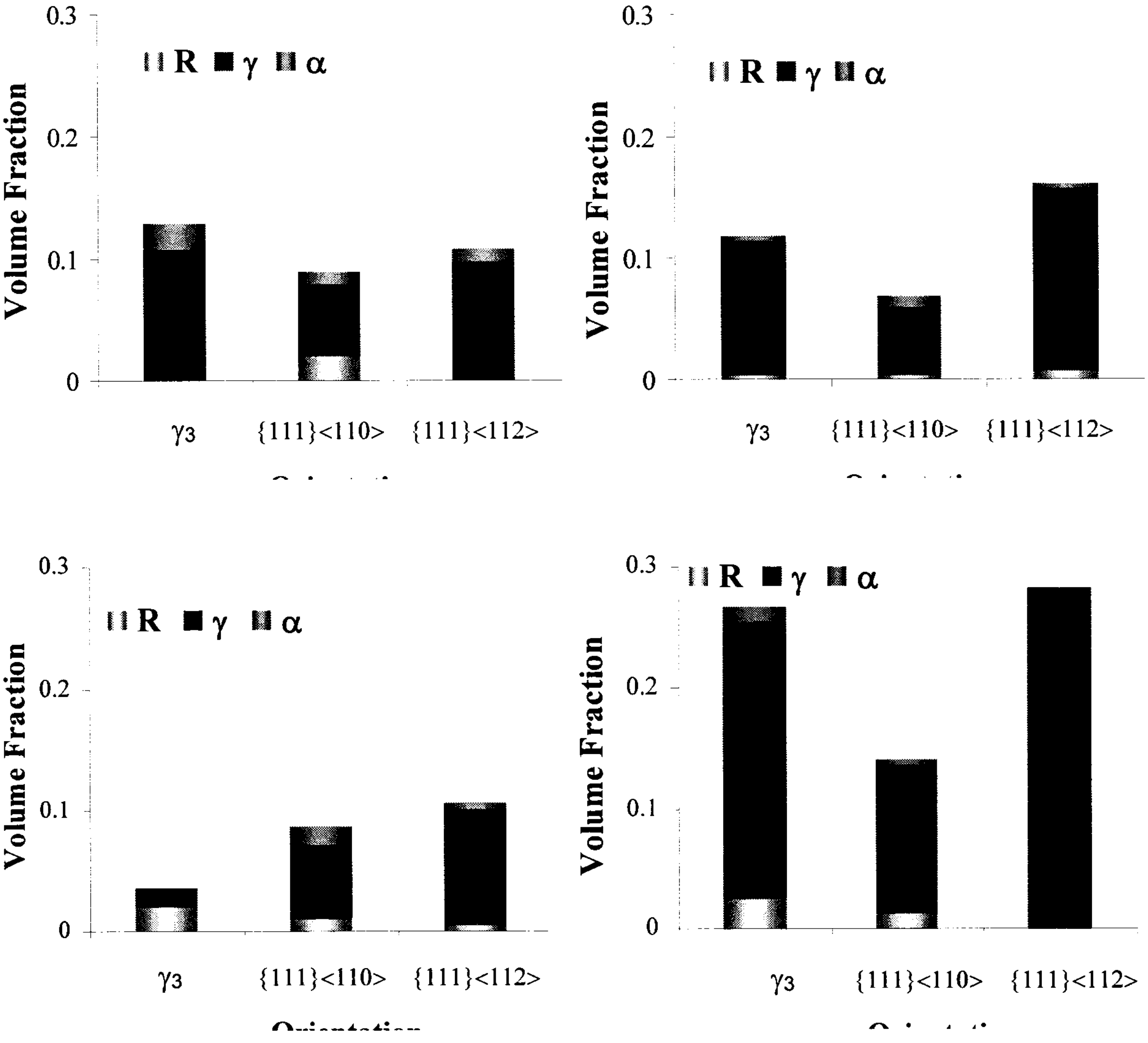

Figure IV.39. Distribution of the {111}<110>, {111}<112> and γ3 nuclei formed within deformed grains. The volume fractions were calculated from EBSD measurements carried out on materials in the early stages of recrystallization and presented in Figures IV.22 to IV.25: a) 65%WR-CHGS, b) 65%WR-FHGS, c) 65%WR+40%CR-FHGS and d) IF-steel.

IV.8.3 Evolution of the texture during recrystallization

The change of texture during recrystallization is presented according to three approaches: evolution of i) the total texture, ii) only the deformed grains, and iii) only the recrystallized grains.

In Fig. IV.40, the textures of the 65%WR-CHGS sample indicate that the intensities of the deformed {111}<hkl> orientations decrease at a faster rate than those of the α-fibre; this signifies that the former were the first to recrystallize. The presence of the α-fibre in the ODF for the deformed grains at 80% recrystallization clearly illustrates that these components were the last to recrystallize. It should be noted that the ODF for the recrystallized grains is not truly representative due to their coarse size, which prevents the sample from being statistically significant.

During annealing of the 65%WR-FHGS specimen, Fig. IV.41, the first orientations to recrystallize were principally the {111}<hkl>. As recrystallization progressed, the intensities of the deformed {111}<hkl> gradually decreased and the deformed α-fibre was, once again, the last to recrystallize and be replaced. The texture of the recrystallized grains when recrystallization was almost 80% complete consisted of an incomplete α fibre with a maximum at {112}<110> and a γ fibre displaying some curvature towards the {554}<225>. In the case of the 65%WR+40%CR-FHGS material, Fig. IV.42, the texture changes were similar to those of the solely WR specimens. However, the intensities at {113}<471> and {554}<225>, which are characterized by <110>26° misorientations with respect to {112}<110>, were increased as a result of the additional cold deformation. Once again, the α fibre was the last to recrystallize.

Fig. IV.43 presents the texture evolution in the IF steel. Due to the high statistical weight of the γ-fibre, it dominated the whole process, being the one principally present in the bulk, deformation and recrystallization textures. However, the {112}<110> is detectably present in the deformation texture at 65% recrystallization, suggesting that the reason why it did not appear more clearly was because of the *masking* effect of the dominant γ-fibre.

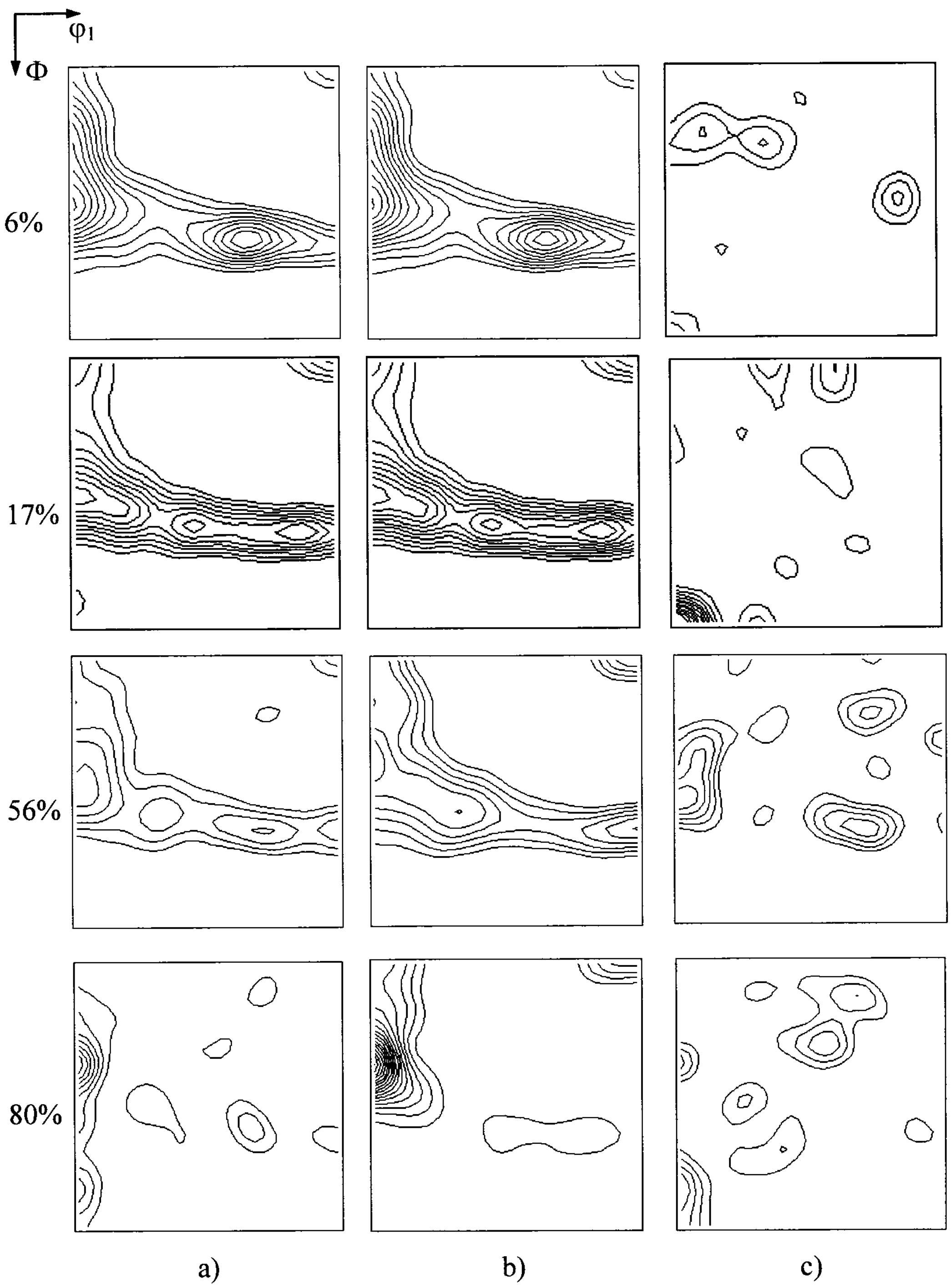

Figure IV.40 Evolution of the texture in the 65%WR-CHGS sample at various percentages of recrystallization: a) bulk texture, b) deformed grains, and c) recrystallized grains. Levels: 2,3,4,.......

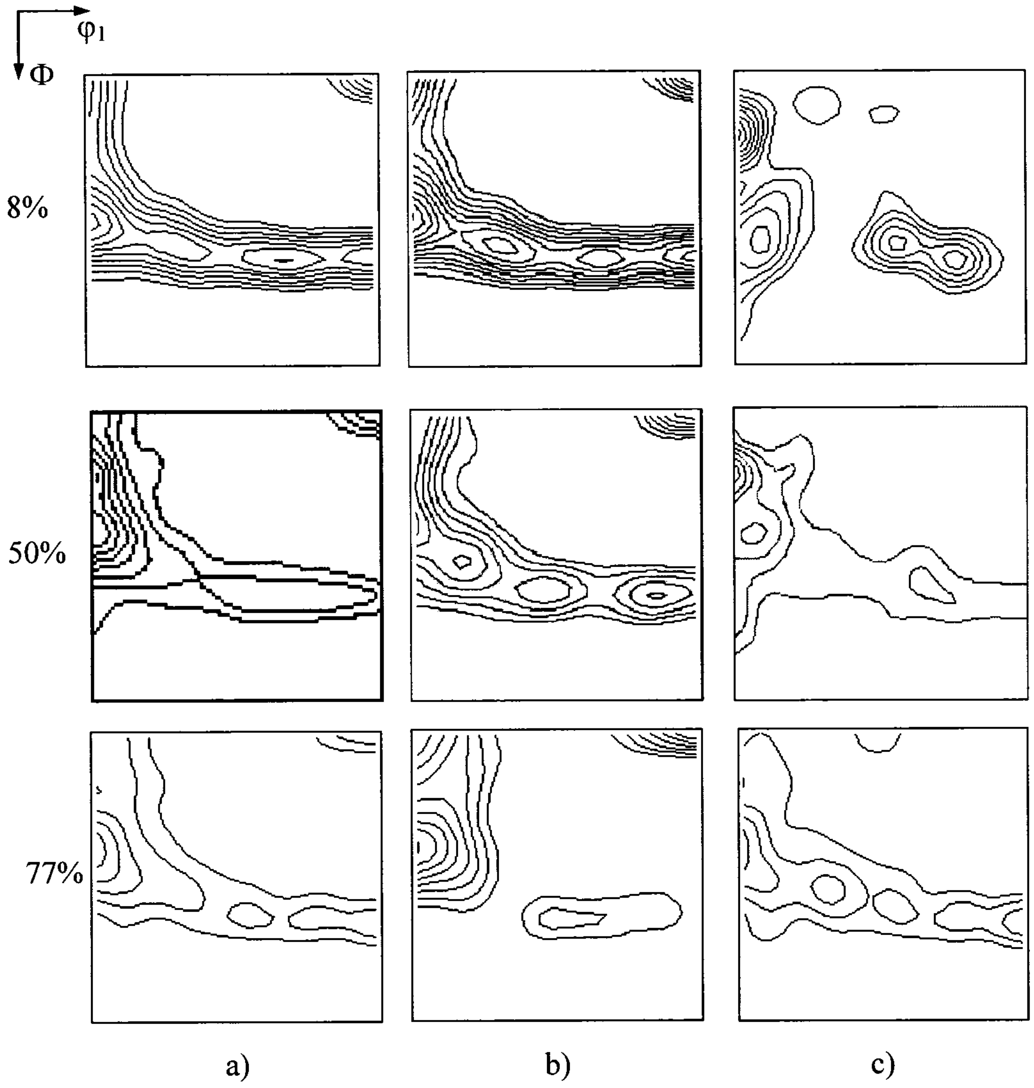

Figure IV.41. Evolution of the texture in the 65%WR-FHGS sample at various percentages of recrystallization: a) bulk texture, b) deformed grains, and c) recrystallized grains. Levels: 2,3,4,.......

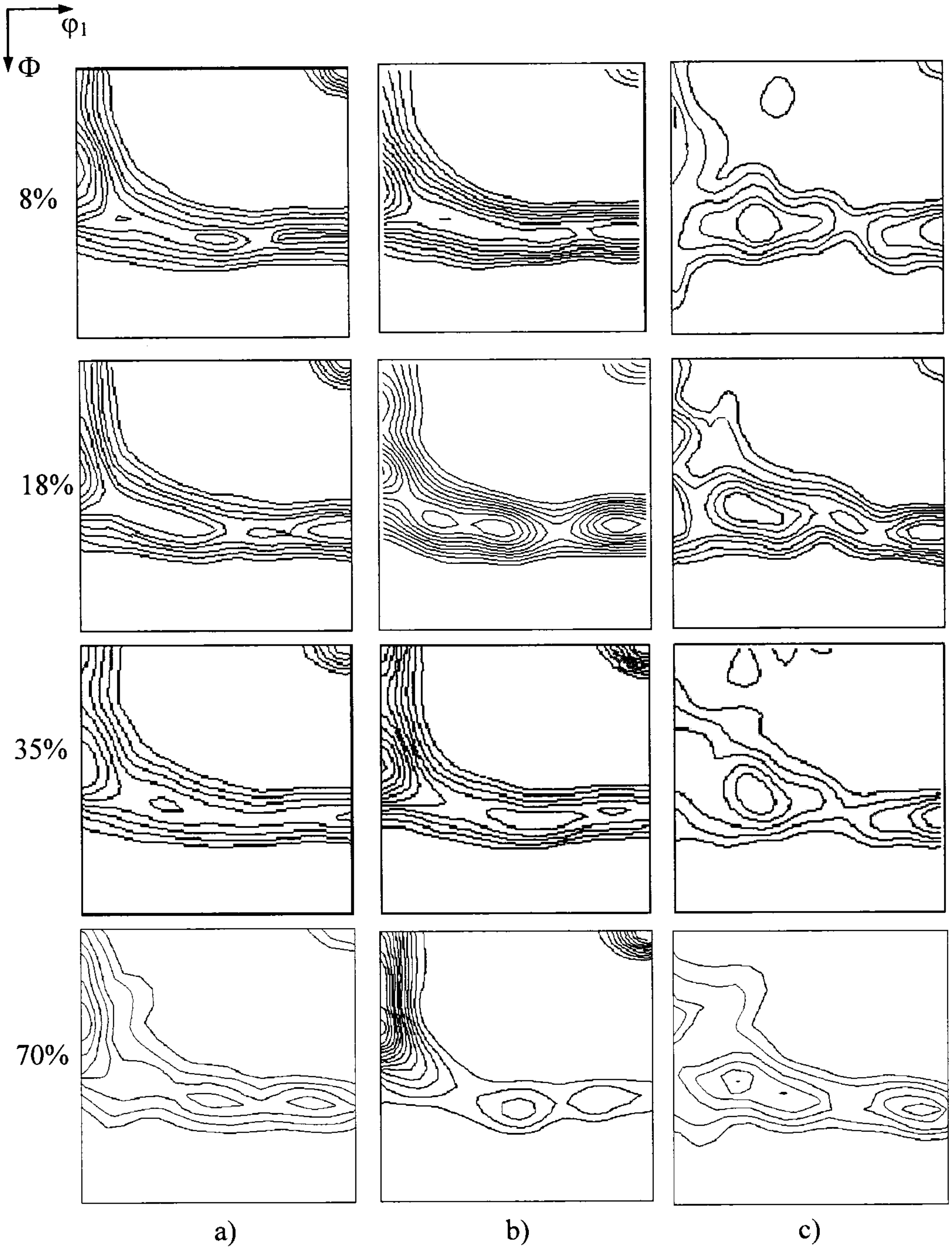

Figure IV.42. Evolution of the texture in the 65%WR+40%CR-FHGS sample at various percentages of recrystallization: a) bulk texture b) deformed grains, and c) recrystallized grains. Levels: 2,3,4,...

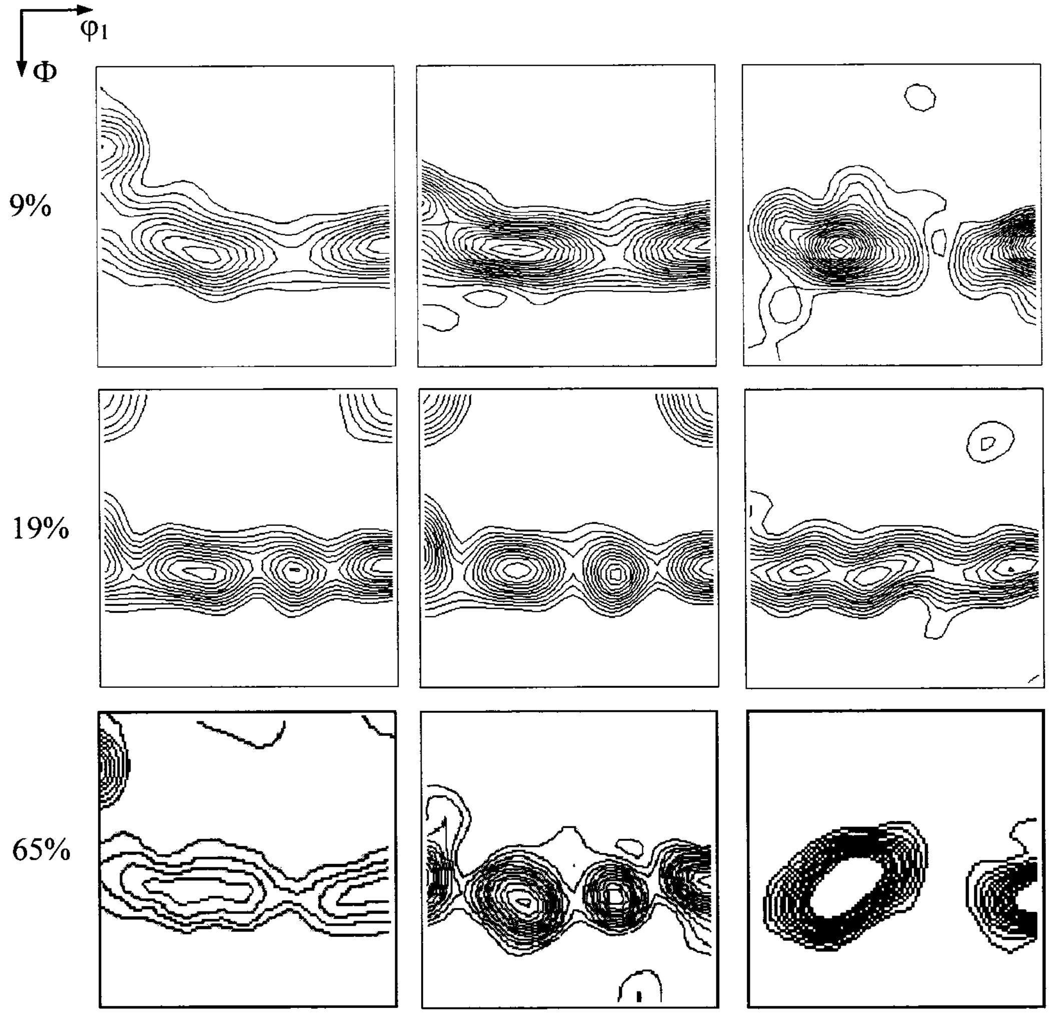

a) b) c)

Figure IV.43. Evolution of the texture in the IF steel sample at various percentages of recrystallization: a) bulk texture, b) deformed grains, and c) recrystallized grains. Levels: 2,3,4,.......

IV.8.4 Microtexture changes

The changes in the volume fractions of the main orientations, α, γ and random, during recrystallization are illustrated in Fig. IV.44 for the three selected experimental conditions and for the IF steel. Many of the differences between the samples can be ascribed to differences in their thermomechanical processing histories. Nevertheless, it is of interest that the volume fractions of the various components do not change much during recrystallization.

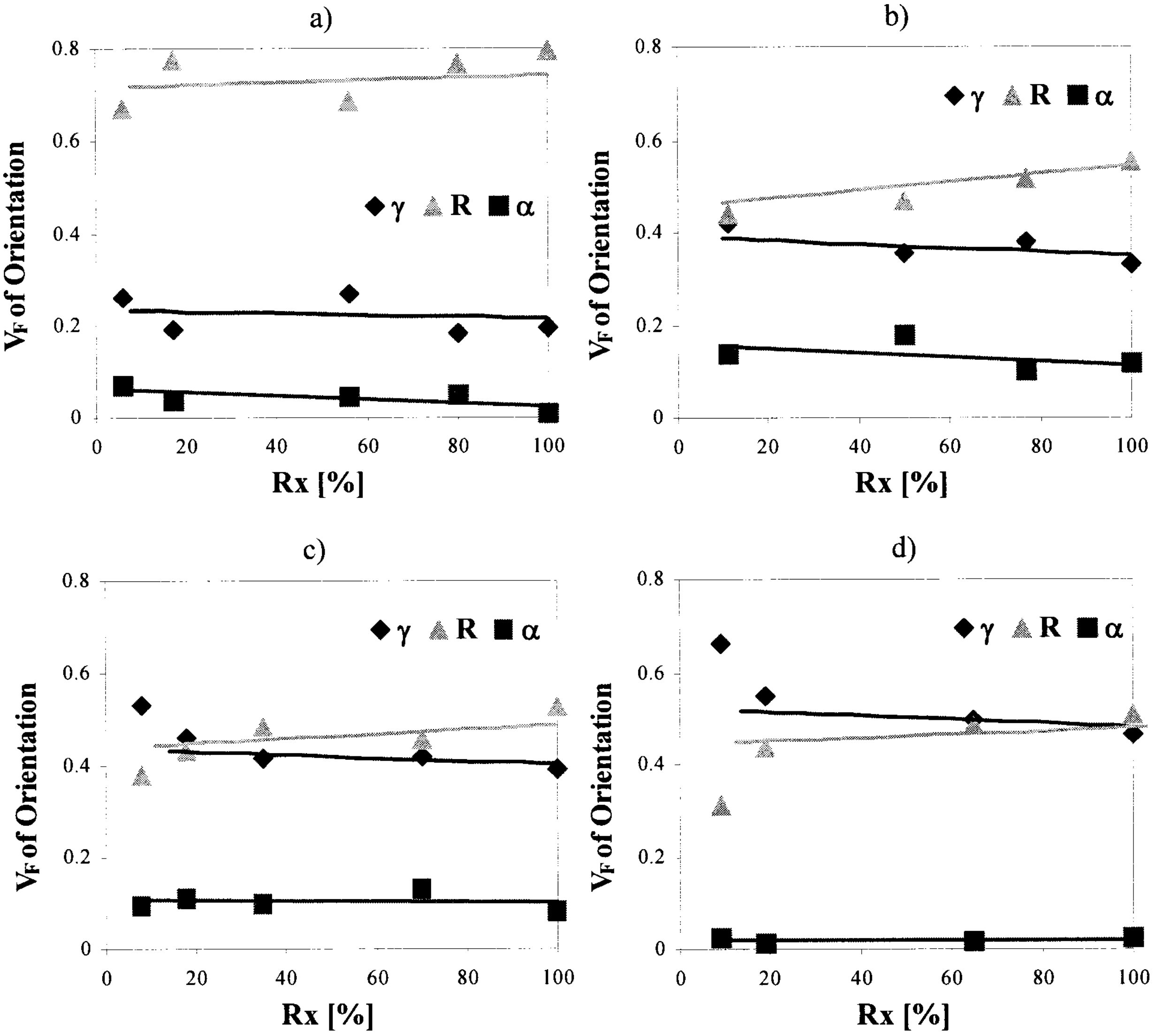

Figure IV.44. Evolution of the volume fractions of the main orientations during recrystallization: a) 65%WR-CHGS, b) 65%WR-FHGS, c) 65%WR+40%CR-FHGS and d) IF-steel.

IV.9 Growth

IV.9.1 Grain size

The boundary line between a nucleus and a full fledged grain can be taken as 2 to 6 μm depending on the material and the author involved [107]. The resolution of the EBSD measurements is very important in determining this limit. In the present work, the 0.3μm step size employed made the limit proposed below an acceptable one. According to the EBSD data, the point at which the continuous grain size distribution graph showed a significant slope change was around 2 μm. Thus, all "grains" less than 2μm in diameter are considered here as nuclei.

The grain size distributions for the α, γ and R components at the various stages of recrystallization listed in Table IV.3 are presented in Figs. IV.45 to IV.47 for the three experimental conditions. Before continuing, it should be noted that different scales and group sizes are used for each condition, in order to be able to appreciate the small changes that affected each distribution.

The number of nuclei pertaining to each sample depended on the deformation conditions. For instance, samples 65%WR-CHGS, Fig. IV.45, and 65%WR-FHGS, Fig. IV.46, contained between 1500 and 2000 nuclei; the 65%WR+40%CR-FHGS material, Fig. IV.47, on the other hand involved up to 8000. The higher number was principally related to the greater amount of deformation. In general, the three specimens displayed similar distributions in the sense that the profiles associated with the α, γ and R orientations were similar. Differences in the *levels* of the distributions can clearly be ascribed to differences in the initial number of nuclei.

There were also differences in the distributions of these nuclei. It can be seen that in Fig. IV.45, most of the nuclei pertain to random orientations. When the HBGS was refined, Fig. IV.46, the number of randomly oriented grains decreased, which translated directly into an increase in the number of γ nuclei. In the case of the 65%WR+40%CR-

FHGS material, Fig. IV.47, the number of γ nuclei was further increased. However, the α orientations were also favoured.

If only grains greater than 6-10 microns in size are considered in Figs. IV.45 to IV.47, a clearer pattern of the grain size distribution and of growth can be established. Such a pattern correlates well with the changes in average grain size of each component during recrystallization presented in Fig. IV.48. Once again, different scales are used for each material for representation of the data, otherwise it would not be possible to detect the differences between the conditions.

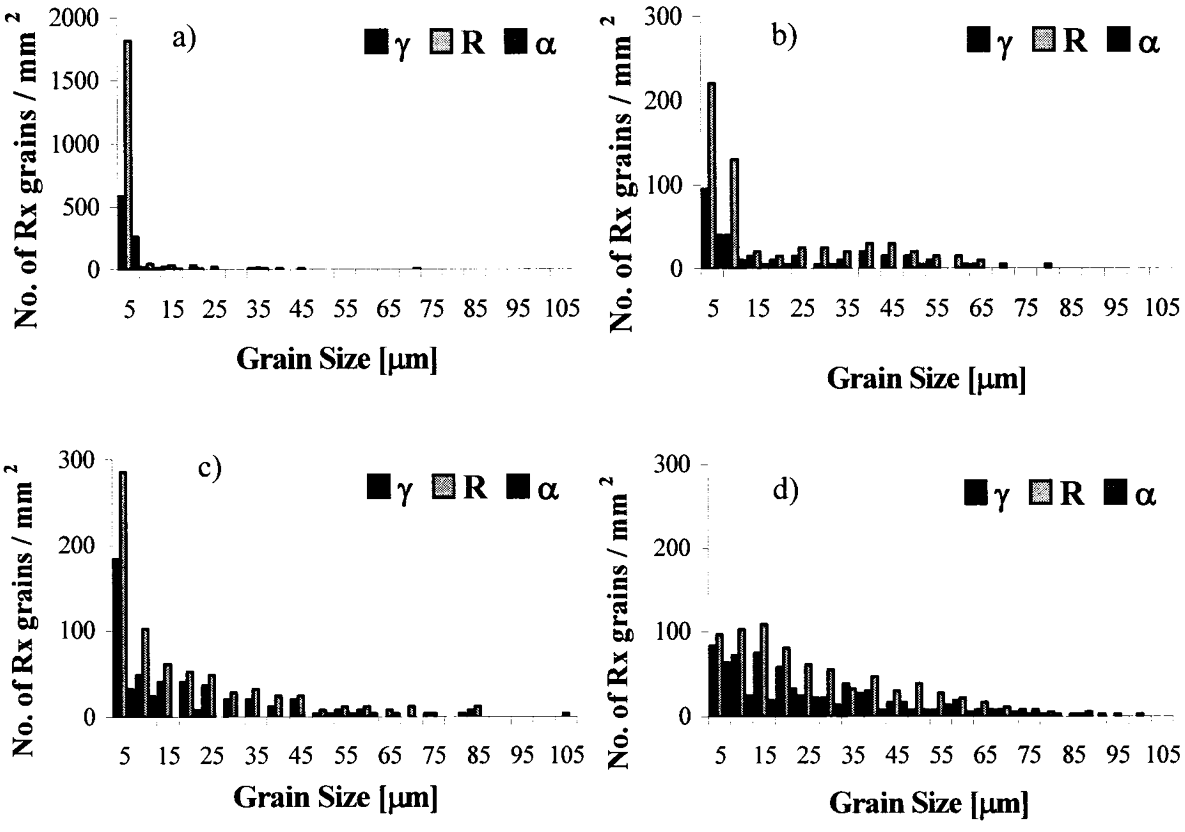

Figure IV.45. Size distributions of the main orientations at various stages of recrystallization for the 65%WR-CHGS material: a) 6%, b) 17%, c) 56% and d) 80% recrystallized.

Two characteristics are clear from the graphs in Fig. IV.45: one concerns the differences in the average grain sizes, during recrystallization and after grain growth, associated with the various processing conditions. These involved both refining the HBGS and increasing the level of reduction. The other characteristic of interest is the common growth pattern followed by the three main crystallographic orientations.

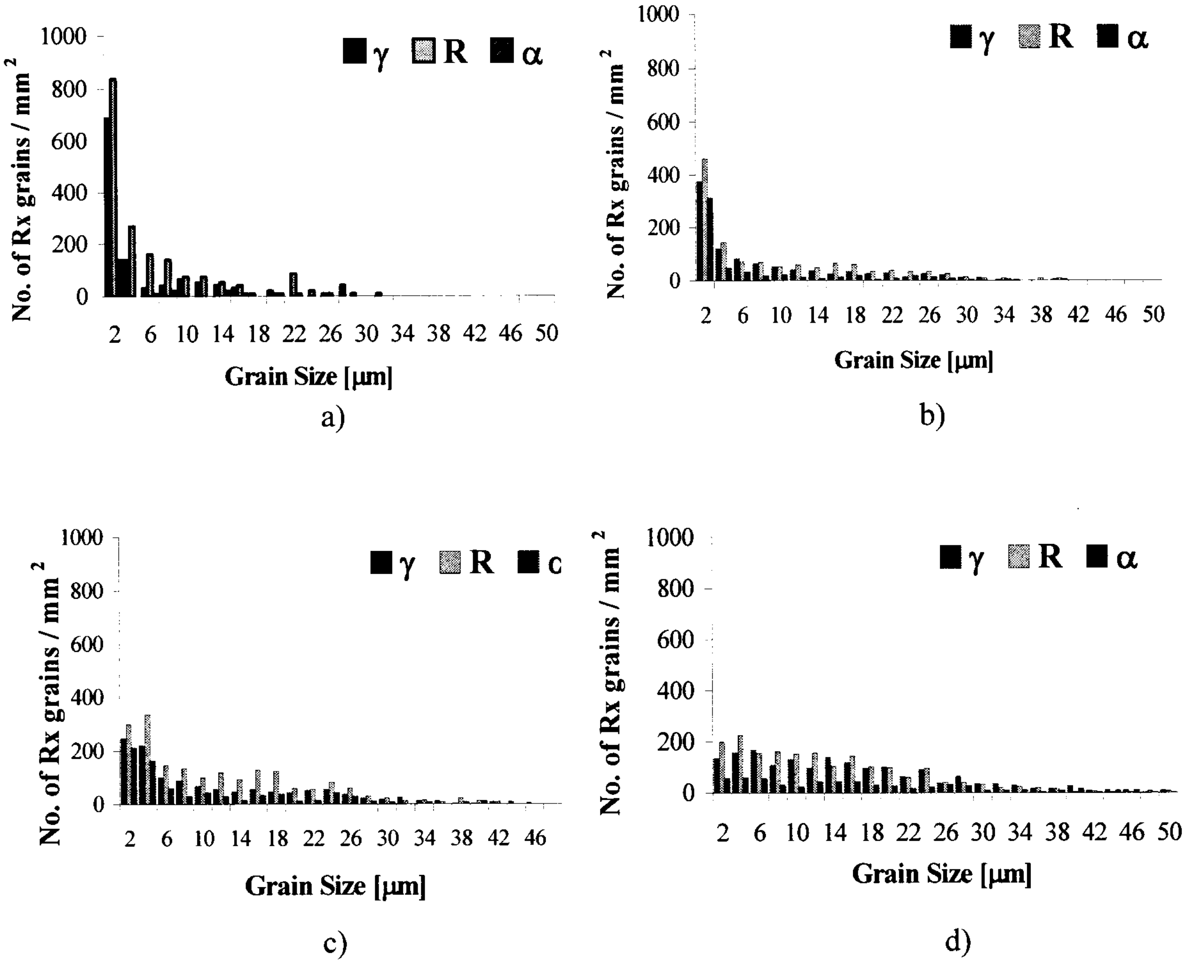

a) b)

c) d)

Figure IV.46. Size distributions of the main orientations at various stages of recrystallization for the 65%WR-FHGS material: a) 8%, b) 24%, c) 50% and d) 77% recrystallized.

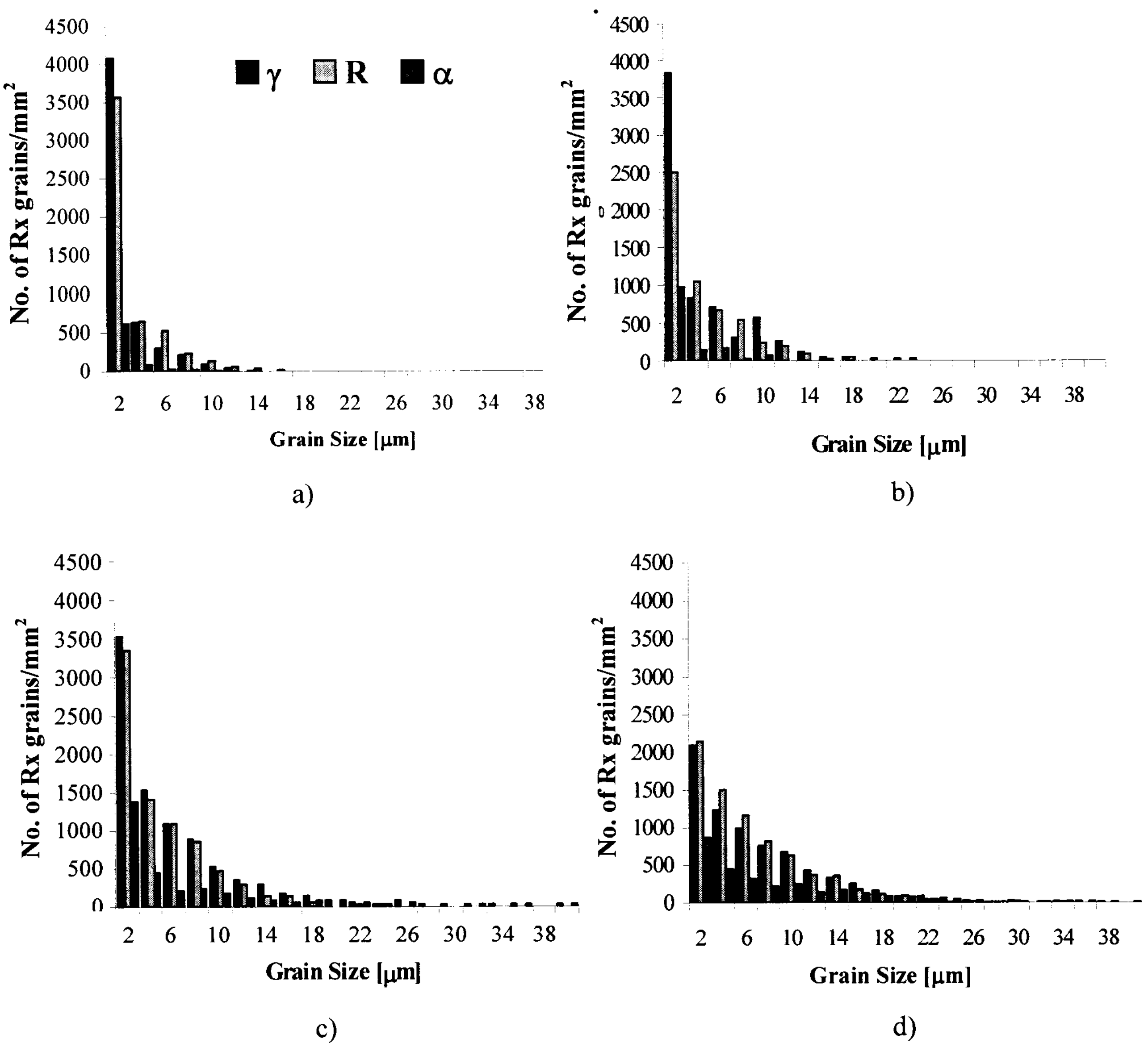

Figure IV.47. Size distributions of the main orientations at various stages of recrystallization for the 65%WR+40%CR-FHGS material: a) 8%, b) 18%, c) 35% and d) 70% recrystallized.

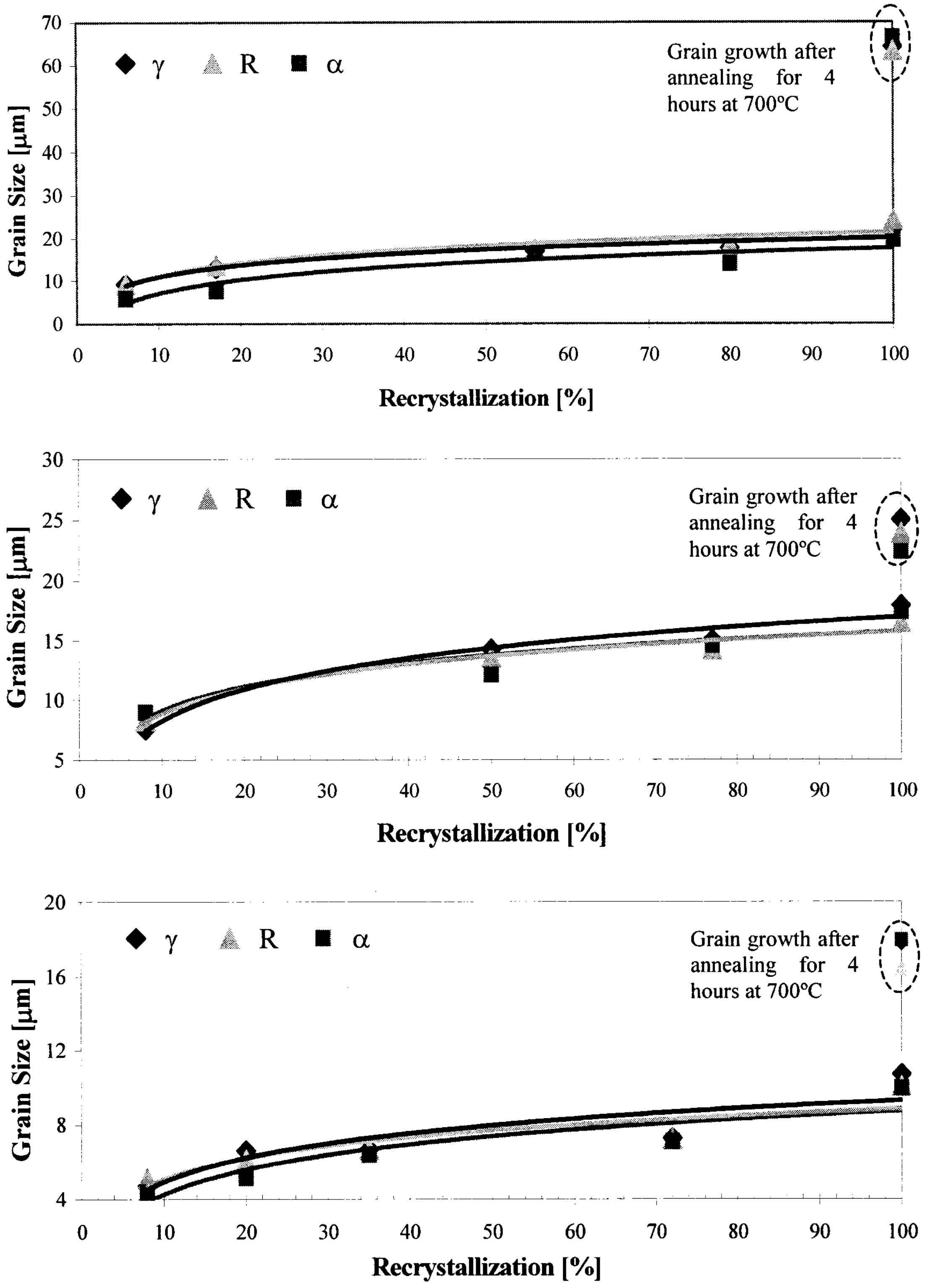

Figure IV.48. Average grain sizes of the main components during recrystallization and grain growth: a) 65%WR-CHGS, b) 65%WR-FHGS, and c) 65%WR+40%CR-FHGS.

IV.9.2 Growth rates

In order to predict the final texture or microstructure, it is necessary to know the growth kinetics, which can be calculated for each component using the Cahn-Hagel method, as extended by Juul Jensen [108, 109] to include crystallographic orientations.

$$G_i = \frac{\mathbf{1}}{\mathbf{Sv_i}} \cdot \frac{dXv_i}{dt} \qquad 13)$$

Here G is the growth rate, Sv_i is the interfacial area per unit volume separating recrystallized and deformed grains, and dXv_i/dt the slope of the isothermal recrystallization curve for a given crystallographic component ***i*** within a given angular range. For this purpose, Sv_i was defined in the normal way using the number of grain boundary intercepts per unit length as given by:

$$Sv = 2\frac{I_i}{L} \qquad 14)$$

Here I_i is the number of grain boundary intercepts between deformed and recrystallized grains of the i^{th} component and L is the total length of gridded test lines. In the present work, the method was applied separately to the volume fractions of the α, γ and R components; these were defined as falling within a spread of 15° for each orientation, as shown in Fig. IV.21. In the case of α, the {001}<110>, {112}<110> and other {hkl}<110> orientations were chosen, while the {111}<110>, {111}<112> and {111}<hkl> orientations were defined as pertaining to the γ fibre. Orientations excluded from these two fibres were considered as part of the random orientations R, see Fig. IV.21. The interfacial areas were measured for each of the three components using the orientation maps produced by EBSD.

The change in recrystallized fraction with time of each component, dXv_i/dt, was obtained by fitting the recrystallization kinetics data points using the JMAK equation [53].

$$\mathrm{Xv} = 1 - \exp(-\beta \cdot t^{n}) \qquad 16)$$

In the previous work [110], G was calculated according to Eq. 17 below.

$$G_i = -\frac{\mathbf{1}}{\mathbf{Sv}_i} \cdot (\mathbf{1} - \mathbf{Xv}_i)\,\mathbf{ln}(\mathbf{1} - \mathbf{Xv}_i) \cdot n \cdot t^{-1} \qquad 17)$$

In the present work, as annealing was carried out under *non-isothermal* conditions, a true growth rate could not be deduced. Nevertheless, it was possible to calculate the *apparent* growth rate [107] by taking into account the heating rate employed during annealing.

$$\frac{dXv}{dt} = \frac{dXv}{dT} \cdot \frac{dT}{dt} \qquad 18)$$

The calculated apparent growth rates for the three experimental conditions are shown in Fig. IV.49. It is clear that the γ and R components followed similar growth rates. Note that the high apparent growth rate of the α component arises from the very low value of Sv_α in Eq. (13) and not from a high value of dXv_α/dt. On the other hand, the values of the interfacial area, presented in Fig. IV.50, are the smallest for this component.

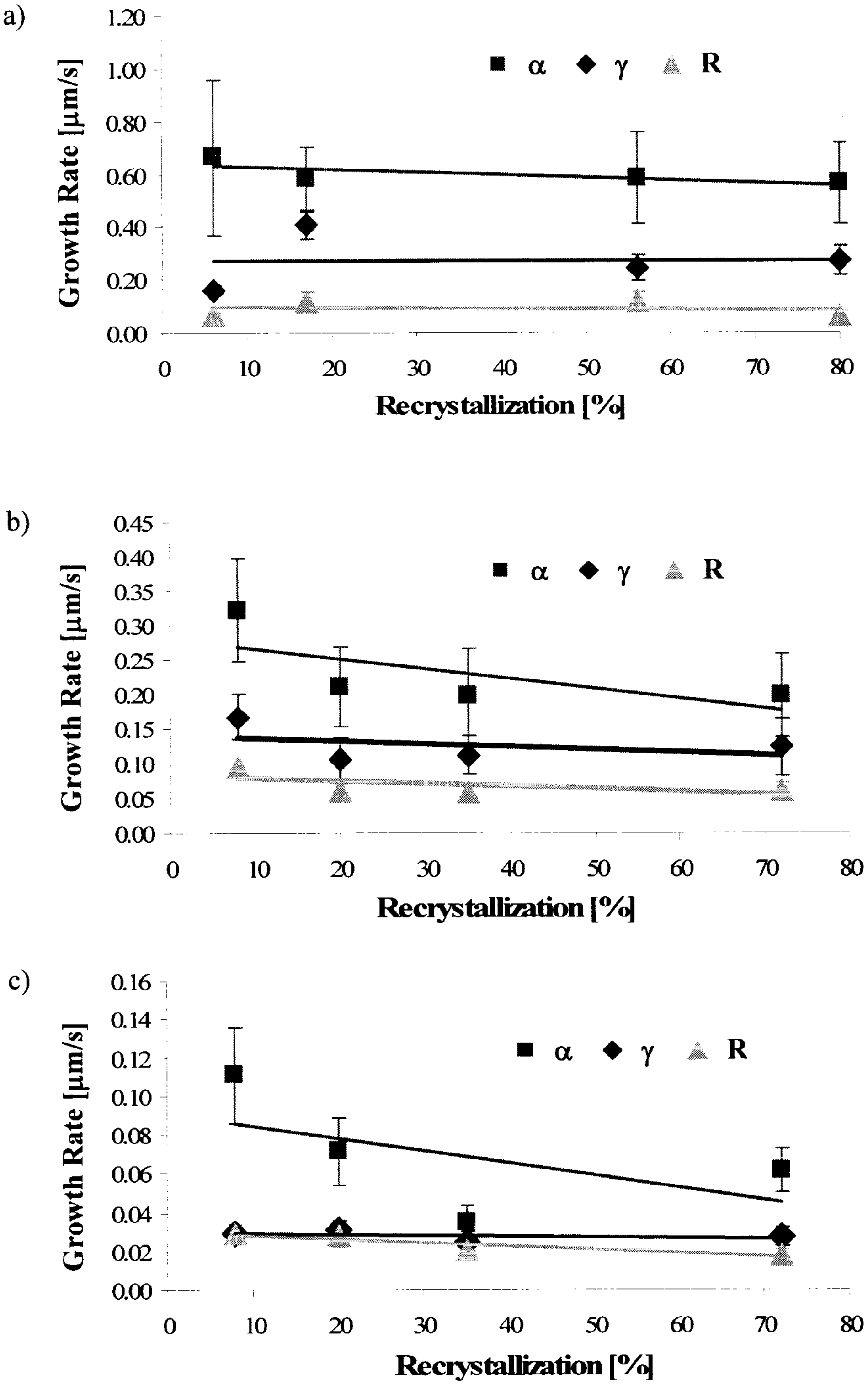

Figure IV.49. Apparent growth rates calculated for a heating rate of 2.5°C/s: a) 65%WR-CHGS, b) 65%WR-FHGS, and c) 65%WR+40%CR-FHGS materials.

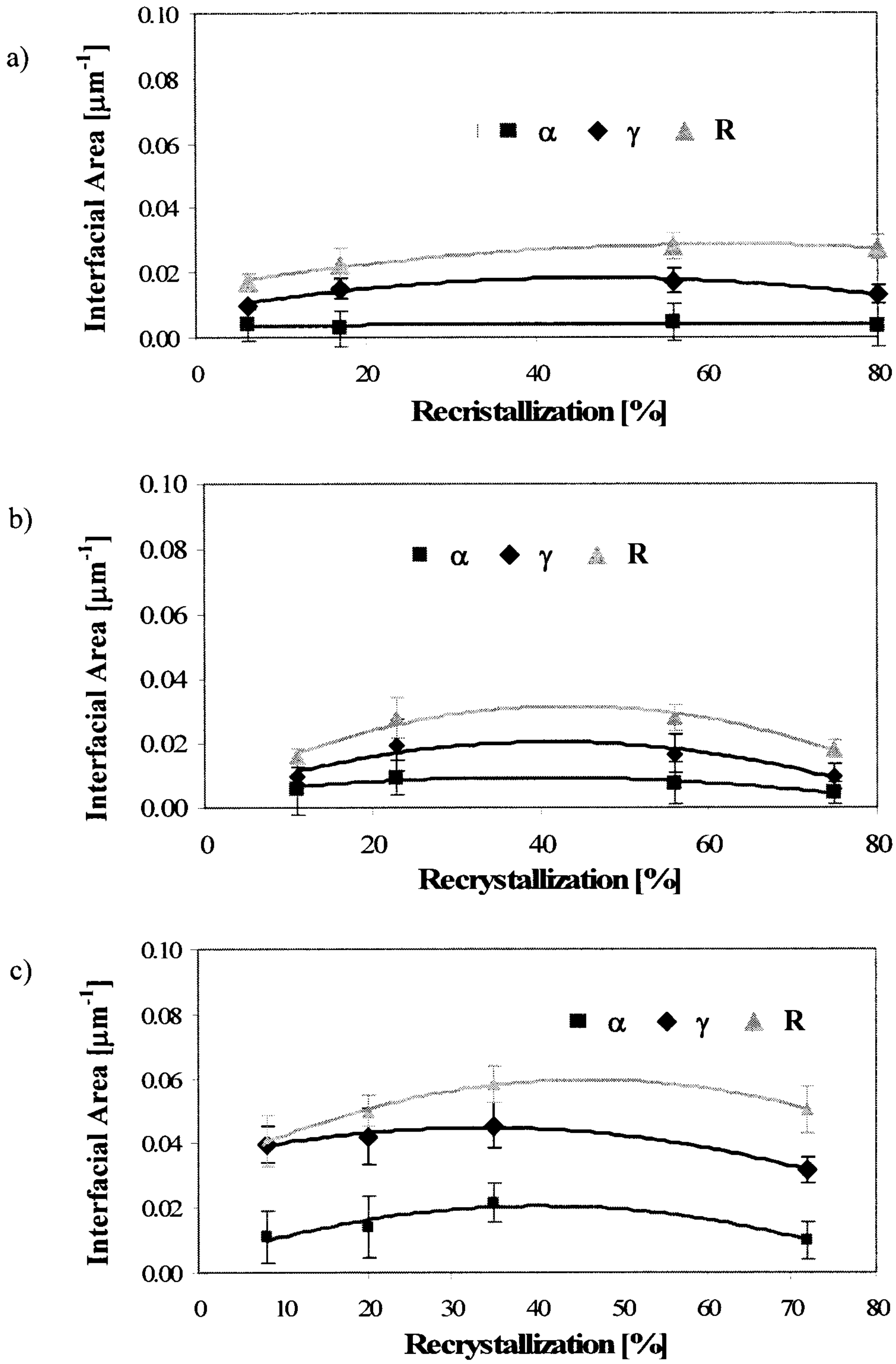

Figure IV.50. Interfacial areas between deformed and recrystallized grains in: a) 65%WR-CHGS, b) 65%WR-FHGS, and c) 65%WR+40%CR-FHGS materials.

CHAPTER V

V DISCUSSION

V.1 Deformed State

In this section, an analysis is presented of the characteristics associated with the deformed state of the low carbon steels studied in the present work. The effects of chemical composition, the hot and warm rolling conditions, and the deformation textures resulting from the above are considered here.

V.1.1 Effect of chromium

The addition of chromium reduces the amount of free carbon available in the ferrite at relatively low temperatures. It does this by increasing the amount of pearlite formed [4], by enhancing the formation of carbides of the $Cr_{23}C_6$ and Cr_3C_2 type [66], and perhaps by the formation of Cr-C complexes. The precipitation of C in the form of coarse carbides at the lower temperatures affects the DSA behaviour at warm rolling temperatures. This was reflected in Fig. IV.3 by the extension of dynamic strain hardening range by 350°C above the temperature at which the flow stress maximum occurs in plain LC steels [81]. This plateau is caused by the addition of 0.8%Cr and the presence of solute C in the warm rolling temperature range.

A similar result was obtained by Glen [84] for Cr contents of 1.35%. Glen also showed that the extension of the DSA peak was significantly reduced when chromium additions of less than 0.66% were made. However, these values correspond to a steel containing 0.12%C. In the case of the present materials, these Cr ranges are equivalent to 0.2-0.45%Cr and 0.11-0.22%Cr for the ELC(Cr) and LC(Cr) grades, respectively (based on simple proportionality). This implies that "excess" chromium was added to the current experimental steels. On the other hand, when a comparison is made with the results obtained by Humphreys et al. [13] for an addition of 0.52%Cr to a similar steel containing 0.037%C, and with those found by Romani [105] for additions of 0.8%Cr and 0.0045%B, it can be seen that the present addition of 0.8% Cr produces a much broader flow stress peak, with continued DSA hardening at temperatures up to 80°C above that obtained by the former workers.

These observations, together with the strain rate sensitivities obtained for the LC(Cr) and ELC(Cr) steels and displayed in Fig. IV.4, suggest that the optimal content of chromium required to extend the DSA behaviour is around 0.8%.

V.1.2 Shear bands

The number and morphologies of the shear bands contained in the deformed microstructures were affected by the hot band grain size. This was around 30µm for the CHGS and 18µm for the FHGS materials. The deformation temperature and amount of reduction also played a role.

In the case of the CHGS material, the number of shear bands increased and their morphology became more continuous and intense at the lower deformation temperatures and higher reductions. This was illustrated in Figs. IV.6 and IV.2, respectively. Here, it is clear that a further cold rolling reduction of 40% has an important effect on the increase. These results can be explained in terms of the occurrence of DSA. At the higher warm rolling temperatures where DSA has no effect, the mobility of solute carbon increases considerably, reducing its interaction with mobile dislocations. Consequently, the degree of work hardening is reduced and the rate sensitivity is increased. The latter translates into a decrease in the number and intensity of shear bands. On the other hand, such interactions are strengthened at lower temperatures, causing more flow localization, and raising the number and intensity of the bands.

The refinement of the hot band grain size, from 30 to 18µm, caused a reduction in the fraction of grains containing shear bands after warm rolling under all deformation conditions. This is mainly due to the opposition to flow localization introduced by the higher density of GBs, which promotes more homogeneous deformation [51]. However, as will be presented later, this small change had an important effect on the total number and distribution of the recrystallization nuclei.

Compared to the volume fraction of grains containing shear bands in the LC steels studied in the previous investigations [13], the number of bands increased in both the LC(Cr) and ELC(Cr) steels by up to 100% at deformation temperatures of 640 and 700°C. This reveals the effect of Cr on extending the DSA range.

In the case of the boron additions made previously, the shear band density was similar to those observed in the current experimental materials at 640°C. However, this was maintained up to a rolling temperature of 700°C, while for the present LC(Cr) and ELC(Cr) materials, there was a decrease of about 20%. The addition of boron, which appears to reduce the extent of the DSA range by approximately 40°C, Fig. IV.3, should therefore be considered as deleterious for decreasing the rate sensitivity in Fig. IV.4. Although the behaviour of the B-containing materials is close to that of an ideal material, perhaps because of the scavenging of interstitials [111-113], it is not clear at the moment why such B-modified grades do not mimic the behaviour of IF steels.

According first to Barnett [65] and later to Toroghinejad et al. [14], shear bands of moderate intensity serve as sites for the nucleation of {111} textures or of the <111>//ND fibre. An increase in the number of such bands should therefore lead to a higher number of nucleation sites for these orientations. This expectation will be reviewed in the nucleation section.

V.1.3 Dislocation density

The relations between the dislocation density and the deformation temperature and amount of reduction, displayed in Fig. IV.9, bear some similarity to the case of shear bands. An increase in the deformation temperature reduces the dislocation density. Although this is not visible for reductions of 80% at 700 and 750°C, it can clearly be seen at 640°C. Here, the density is the same as in the former cases, but for a lower reduction of 65%. The effect of deformation temperature is further corroborated when a 40%CR reduction is added to the 65%WR step. Here, the dislocation density was raised by a factor of 3 times. It is convenient to emphasize that this additional cold rolling step only represents an increase of 0.6 in true strain, while that for 65%WR embodies a true strain of 1.2. This means that one-third of the total true strain accounts for 75% of the dislocations generated. The higher content of dislocations increases the number of nucleation sites, an aspect that will be discussed in later sections.

The refinement of the HBGS, illustrated in Fig. IV.10, slightly increased the dislocation density. However, this small increase raised the number of recrystallization nuclei significantly. The higher dislocation content can be attributed to the restrictions introduced by the larger density of grain boundaries.

What is clear from these results is that the amount of reduction is a very important variable in the warm rolling process. The dislocation density associated with the WR+CR material is 4 times higher than that of the sample solely WR 80% at 700°C. Nevertheless, the additional CR deformation causes increase of about 0.2 in the mean r-value. It is clear then that WR reductions higher than the 65-80% employed in the present work will not make a significant contribution to the formability. The large differences between warm and cold deformation can be attributed to: i) the decreased importance of solute carbon-dislocation interaction at the lower temperatures [97], and ii) the possible occurrence of dynamic recovery at the two higher WR temperatures [114, 115].

V.1.4 Deformation texture

The deformation textures consisted principally of the α-fibre running from {001}<110> to {110}<110> and the γ–fibre running from {111}//<110> to {111}<112>. As the deformation temperature was increased, the intensity of the α-fibre was significantly enhanced by up to 8 random units; concurrently, that for the γ–fibre was reduced by about 2 random units. This can be seen in Figs. V.1 and V.2. These trends affect the recrystallization textures negatively, as the latter are highly influenced by the deformation texture. The sharpening of the deformation textures at the higher deformation temperatures is related to a decrease in the level of fragmentation of the deformed microstructure. This is driven by a reduction in the volume fraction of grains containing shear bands [65], which in turn is caused by the increase in the rate sensitivity. No significant differences can be detected between the LC(Cr) and ELC (Cr) experimental materials. However, it seems that the lower C content in the ELC(Cr) steel can account for less intense α and γ fibres at 700°C.

The refinement of the HBGS further raises the intensity of the deformation texture, as presented in Fig. IV.12, but it does not cause any change in the *nature* of the texture. The former is a result of the increase in grain boundary density, which promotes a larger number of interactions between dislocations and grain boundaries. The dislocation multiplication that results is reflected in Fig. IV.10 by the minor but perceptible increase in the dislocation density by comparison with the CHGS case exhibited in Fig. IV.9.

The additional cold rolling reduction raised the intensities of the fibres of the two materials by approximately 2 random units. It also created a maximum at {112}<110> for the α-fibre and shifted the maximum on the γ-fibre. The latter was originally at {554}<225> and then moved towards {111}<112>. These minor changes indicate that the texture distribution is primarily established by the prior warm rolling reduction. This conjecture will be further supported in the anisotropy section.

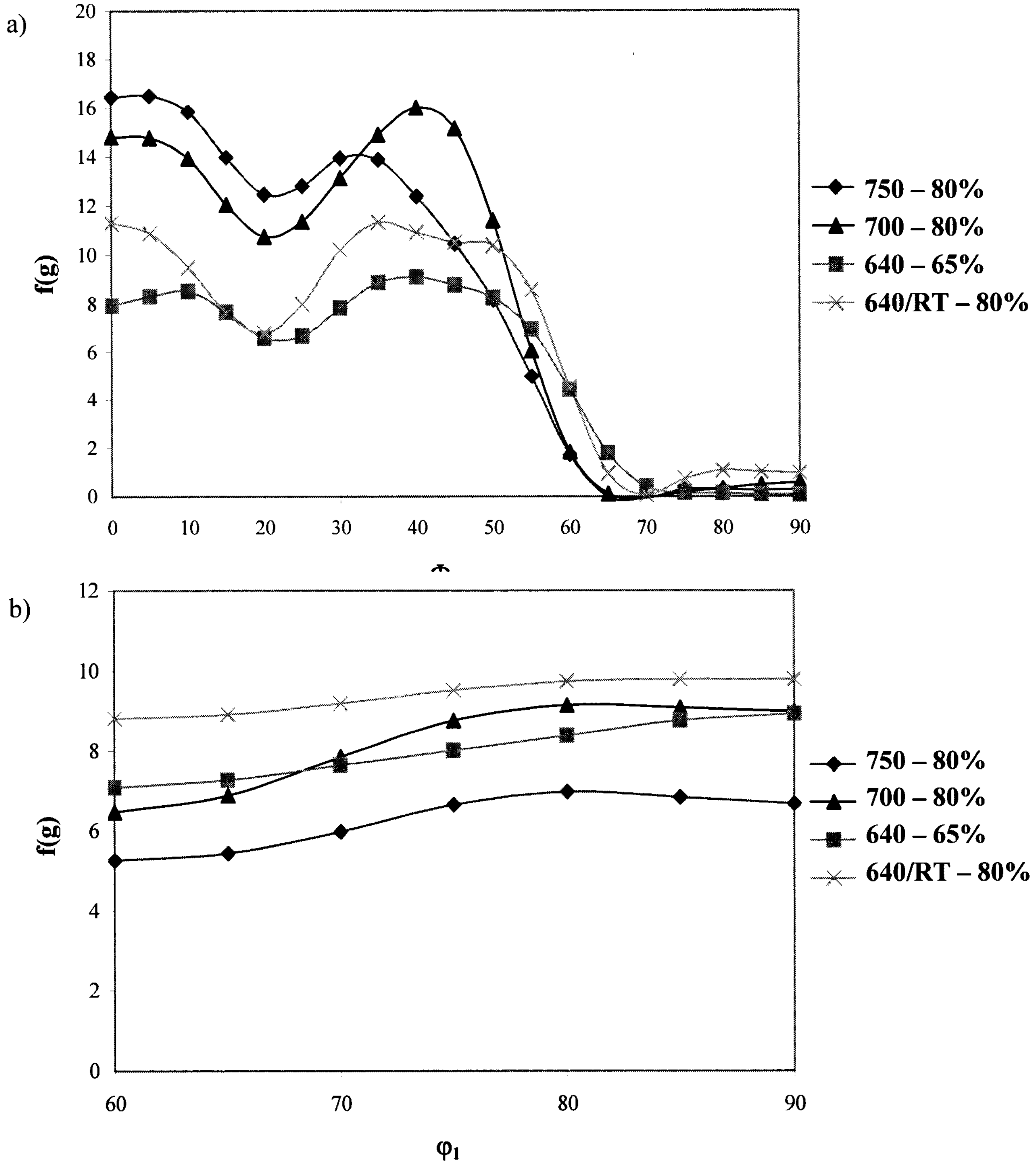

Figure V.1. a) RD and b) ND skeleton lines pertaining to the textures presented in Fig. IV.11. The influence of deformation temperature and rolling reduction on the main deformation texture components can be readily seen. LC(Cr) steel in the CHGS condition.

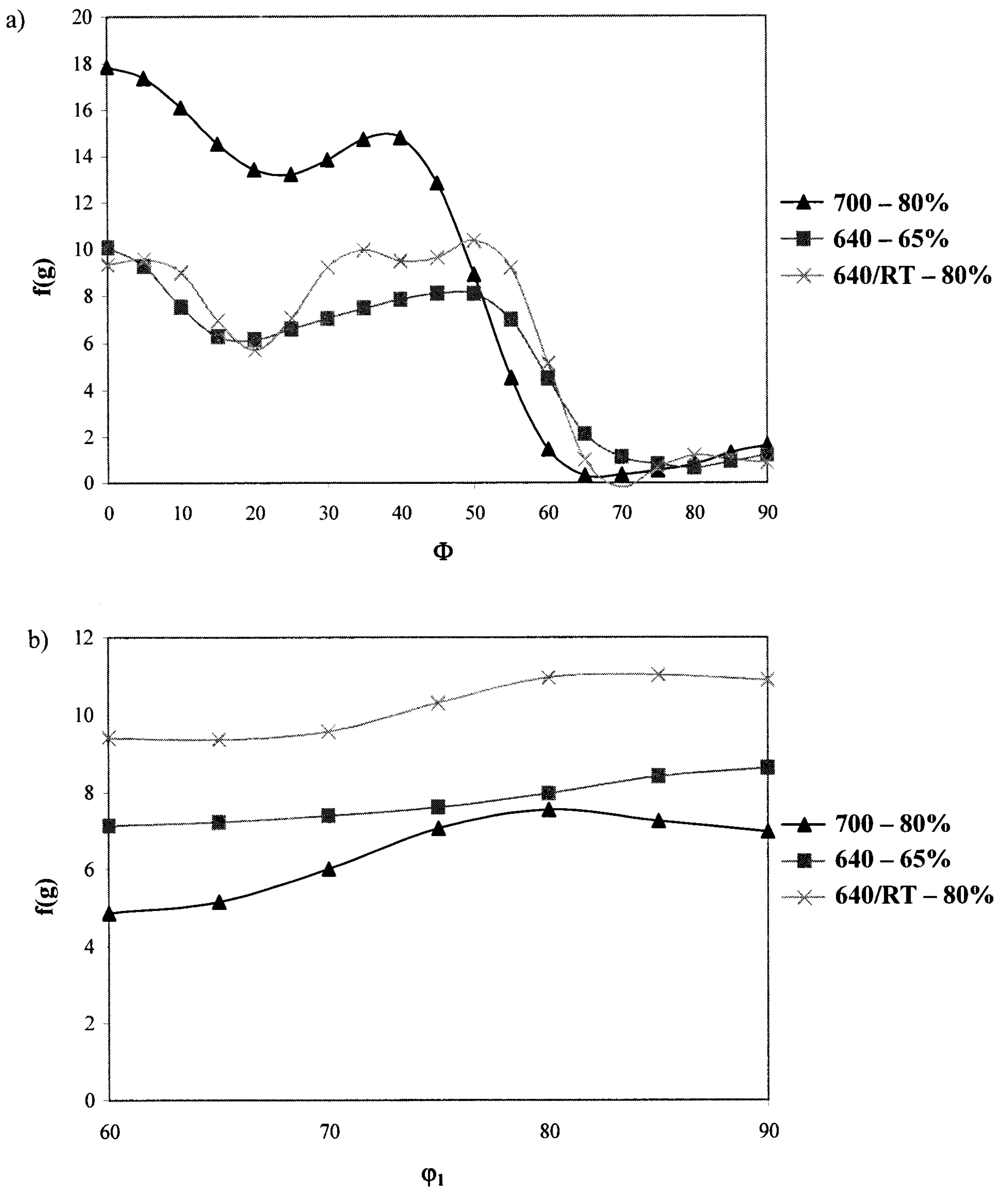

Figure V.2. a) RD and b) ND skeleton lines pertaining to the textures presented in Fig. IV.11. The influence of deformation temperature and rolling reduction on the main deformation texture components can be readily seen. ELC(Cr) steel in the CHGS condition.

V.2 Recrystallized State

V.2.1 Recrystallization kinetics

The deformation temperature has a great effect on the recrystallization kinetics, as shown in Fig. IV.13. According to these results, the time for 50% recrystallization was reduced from 300 to 20 seconds when the materials were further cold rolled 40%. On the other hand, specimens processed only by warm rolling exhibited similar behaviours for deformation temperatures of 640 and 750°C, which suggests that the 65% reduction at 640°C has an effect equivalent to that of 80% deformation at 750°C. The two experimental steels displayed similar recrystallization kinetics.

Refinement of the HBGS accelerated the recrystallization kinetics due to the increase in dislocation density. The latter translates into a higher driving force for recrystallization.

V.2.2 Recrystallization textures

In this section, the effects of the thermomechanical process and chemical composition are discussed. The analysis is divided into four main parts: first, the deformation temperature and amount of reduction are considered. Second, the effect of the additional cold rolling is evaluated. Third, the use of different heating rates during annealing is assessed and, finally, the influence of refinement of the HBGS.

The recrystallization textures were affected by the deformation temperature and amount of reduction. However, in contrast to the observations regarding the deformation textures, not only are the intensities of these textures influenced by the parameters, but the distribution is as well. The recrystallization textures presented in Fig.IV.15, revealed a dominant RD fibre for both the LC(Cr) and ELC(Cr) steels. It can be seen from these results that, as the temperature is decreased, the RD fibre experiences a reduction in both intensity and spread. The plot of the RD fibre in Fig. V.3 offers a clearer view of this and shows that the largest reduction in the intensity (in the warm rolled materials) occurred at 640°C. If attention is focused on specific components, such as the {001}<110> and {112}<110>, see Fig. V.4, it is clear that the intensity of the former remains unaffected by the decrease in deformation temperature, while the latter is reduced at temperatures below 700°C.

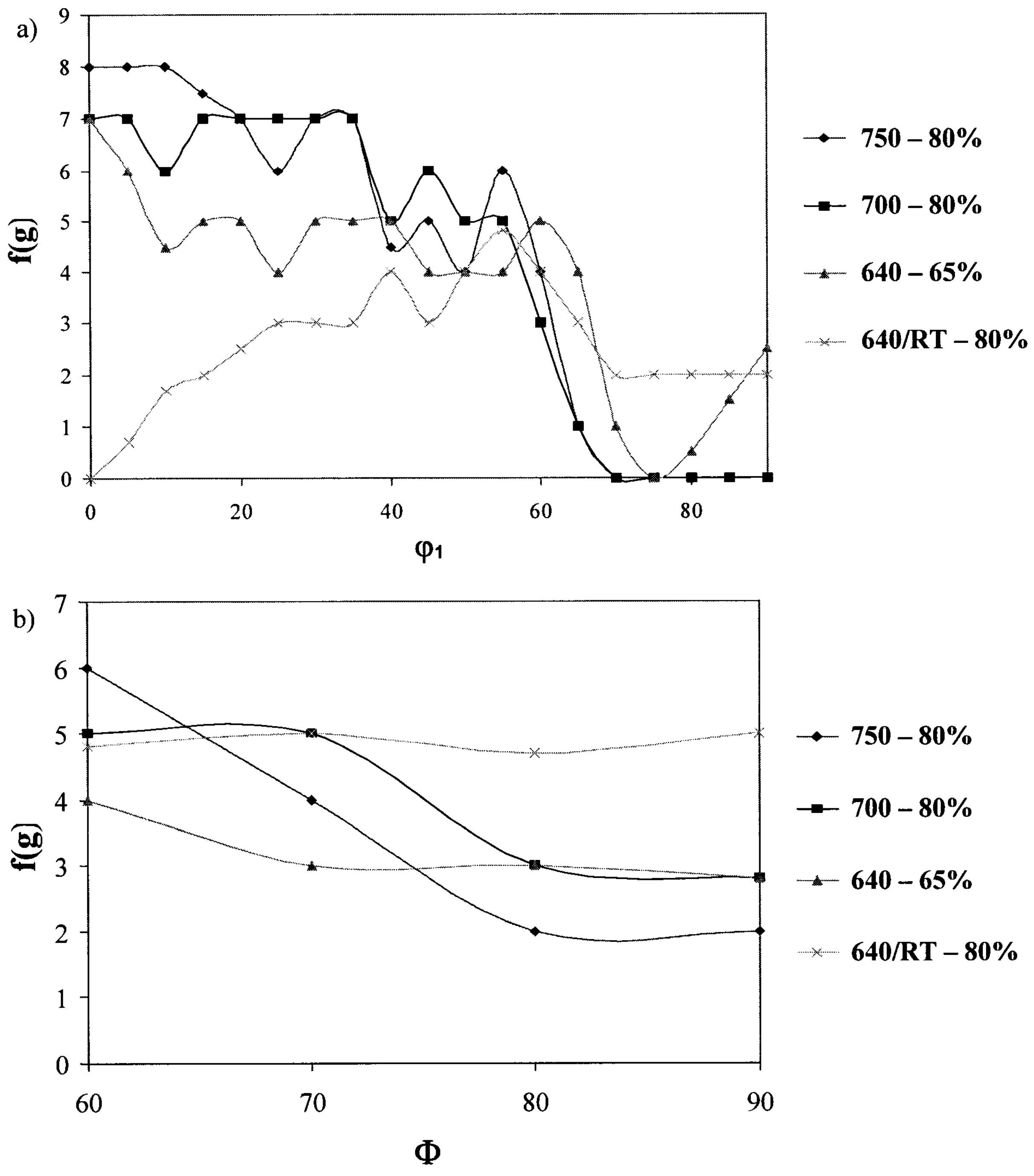

Figure V.3. a) RD and b) ND skeleton lines pertaining to the textures presented in Fig. IV.15. The influence of deformation temperature and rolling reduction on the main recrystallization texture components are shown. ELC(Cr) steel in the CHGS condition. After 4 hours of annealing at 700°C, using a heating rate of 2 K.s^{-1}.

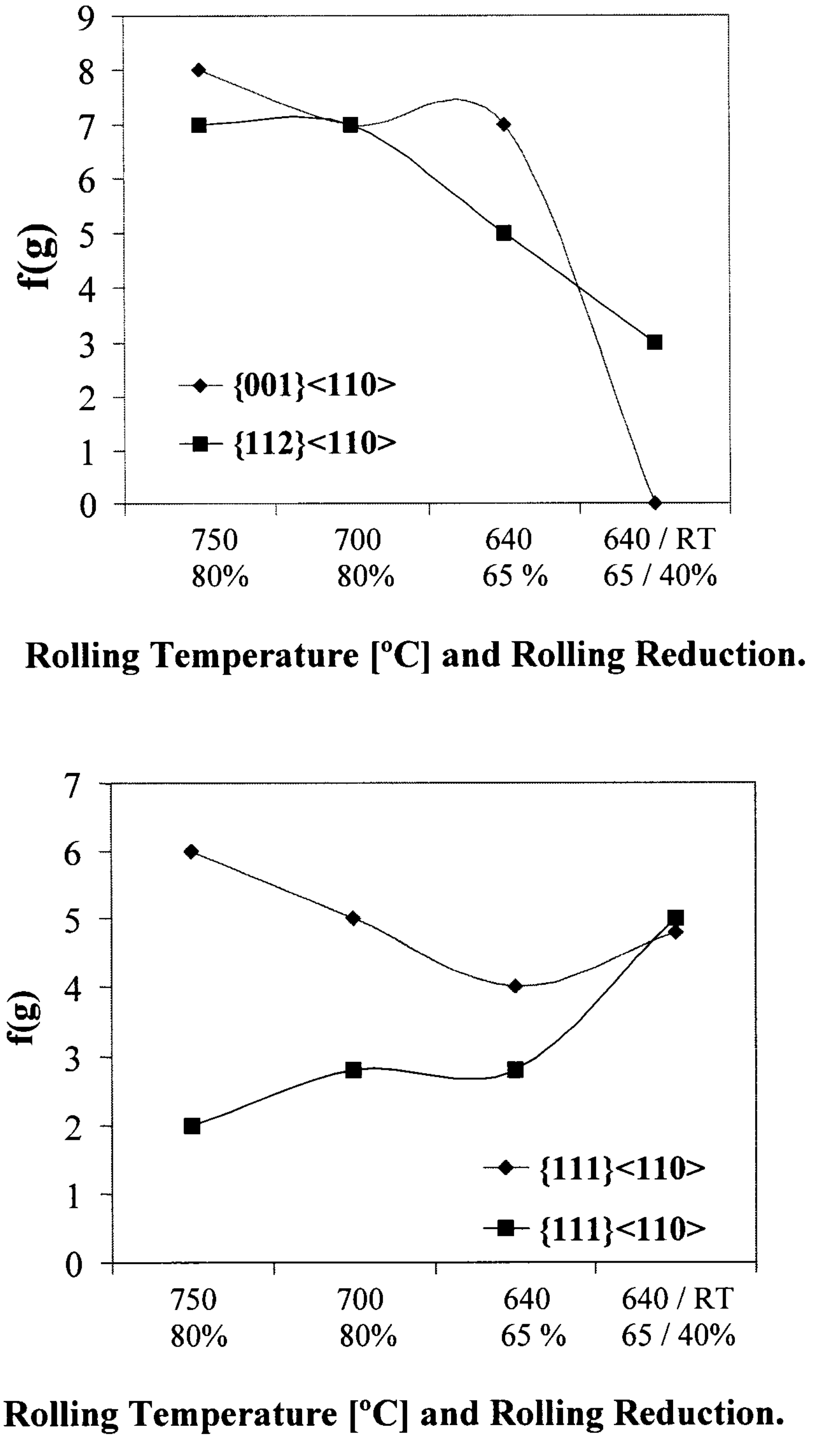

Figure V.4. Effect of rolling temperature on the intensities of the main recrystallization components for steel ELC(Cr) in the CHGS condition. Based on the textures presented in Fig. IV.15. After 4 hours of annealing at 700°C, using a heating rate of 2 K.s^{-1}.

While the ND fibre also experiences a decrease in intensity, the changes in the distribution are not in the spread, but in the increasing continuity of the fibre. This is caused by a progressive shift in the maximum from {111}<110> to {111}<112}, which is illustrated in the ND fibre plot of Fig.V.3. The main orientation graph of Fig. V.4 offers a better view of this.

Compared to the textures of the LC steel [112], the intensity of the ND fibre is higher in the current experimental materials. This is a direct result of the addition of chromium. While boron additions had a similar effect on the ND fibre, they also raised the strength of the entire RD fibre, which remained unchanged as the temperature was decreased [14]. It can therefore be said that the LC(Cr) and ELC(Cr) steels offer better textures. This seems to be related to the chromium reducing the amount of dissolved carbon present before rolling and during annealing. The reduction contributes to the generation of a greater number of shear bands during deformation and a reduction in the retardation of the kinetics of recovery and recrystallization during annealing [12]. The first creates more sites for the nucleation of {111} type grains and the second allows these orientations to nucleate and grow. This explains the more continuous and intense ND fibre obtained for this condition.

The additional 40% cold rolling greatly reduced the intensity of the RD fibre. Furthermore, the rotated cube component, which was not affected by the decrease in the deformation temperature for all the warm rolling samples, was practically eliminated. This can be seen in the skeleton line plots shown in Fig. V.3 and in the main orientation graphs of Fig. V.4. A similar but not as critical effect concerned the {112}<110>, which was not eliminated by the additional cold rolling but substantially reduced. Regarding the ND fibre, it was strengthened by the extra cold rolling, making it more continuous by favouring the {111}<112> over the {111}<110>. The important effects of the changes in both the RD and ND fibres will be presented in the anisotropy section.

The further 40% cold rolling reduction applied to the 65%WR sample was chosen to study the effect of larger deformations, as it is well known that the amount of reduction plays a preponderant role in the improvement of recrystallization textures [7, 42, 116]. It is important to note that this additional cold deformation accounts for an increase of about 4 times in the dislocation density, as presented in Figs. IV.9 and IV.10. The fact that specimens deformed solely at warm rolling temperatures display lower dislocation densities, even when they undergo the same amounts of true strain as the WR+CR material, is explained in terms of the increased mobility of solute carbon at higher temperatures. At the lower temperatures, they pin dislocations leading to additional hardening [81]; at the higher temperatures, there is dynamic recovery during deformation and static recovery during the interpasses.

V.2.2.1 Heating rate

The results presented in the previous section showed that the textures of the current experimental steels were improved with respect to those of the materials in the previous studies. However, they also demonstrate that such improvements are insufficient for the production of materials suitable for deep drawing purposes.

When the heating rate for annealing is reduced from 2 $K.s^{-1}$ to $1.5x10^{-2}$ $K.s^{-1}$, the recrystallization textures of the warm rolled steels are significantly affected. These changes are greater at the lower rolling temperature of 640°C. By contrast, no change was observed in the WR+CR samples, probably because the driving force available for recrystallization associated with this condition, which is represented by the dislocation density, is 4 times higher than that of the WR material. This was presented in Fig.IV.16.

The skeleton lines for the LC(Cr) and ELC(Cr) materials presented in Figs. V.5 and V.6, respectively, and the graphs for the main orientations illustrated in Fig. V.7 offer a clearer view of the effect of lowering the heating rate on the recrystallization texture. In the case of the specimen deformed at 700°C, the intensity of the RD fibre is reduced with respect to the 2 Ks^{-1} heating rate case by about 2 random units. As a result of this change, the rotated cube component almost disappears; at the same time, the continuity of the ND fibre is slightly increased.

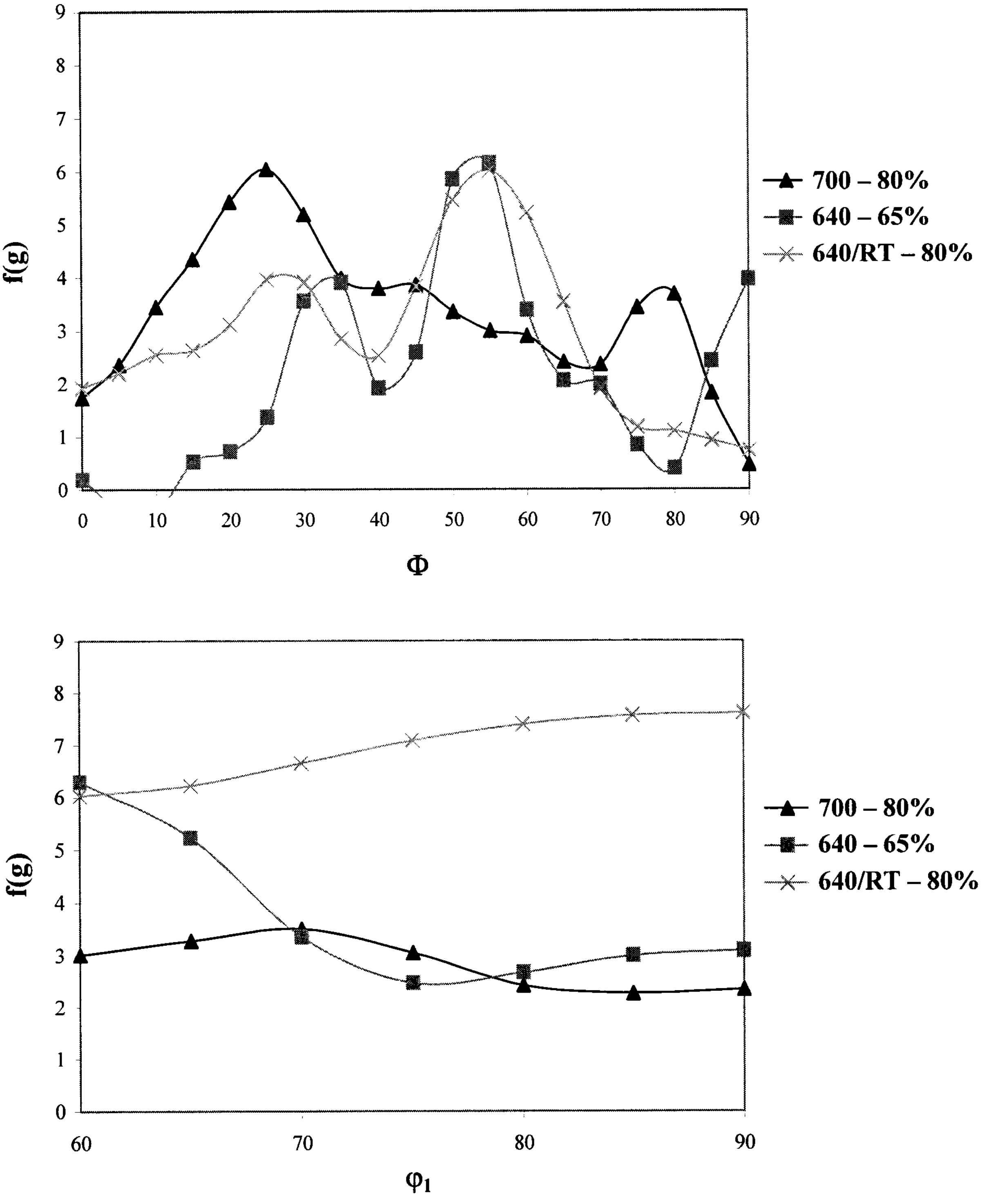

Figure V.5. a) RD and b) ND skeleton lines associated with the textures presented in Fig. IV.16. The influence of deformation temperature and rolling reduction on the main recrystallization texture components of the LC(Cr) steel in the CHGS condition is shown. After 4 hours of annealing at 700°C, using a heating rate of $1.5x10^{-2}$ $K.s^{-1}$.

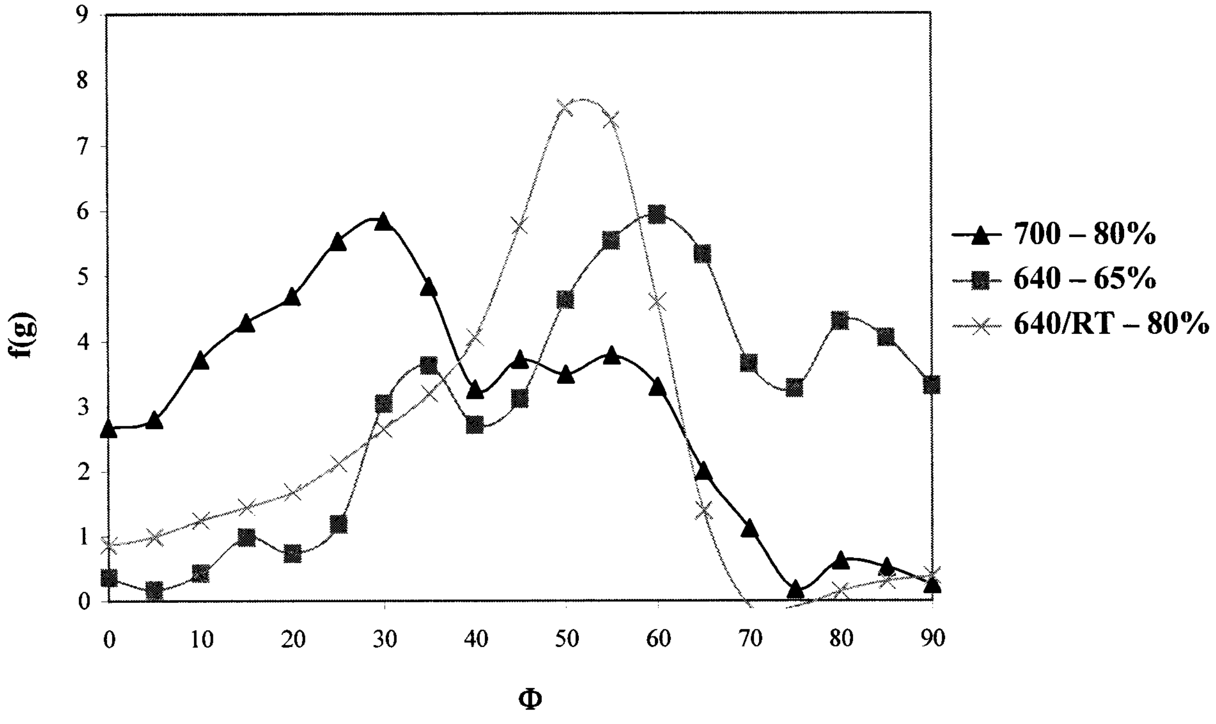

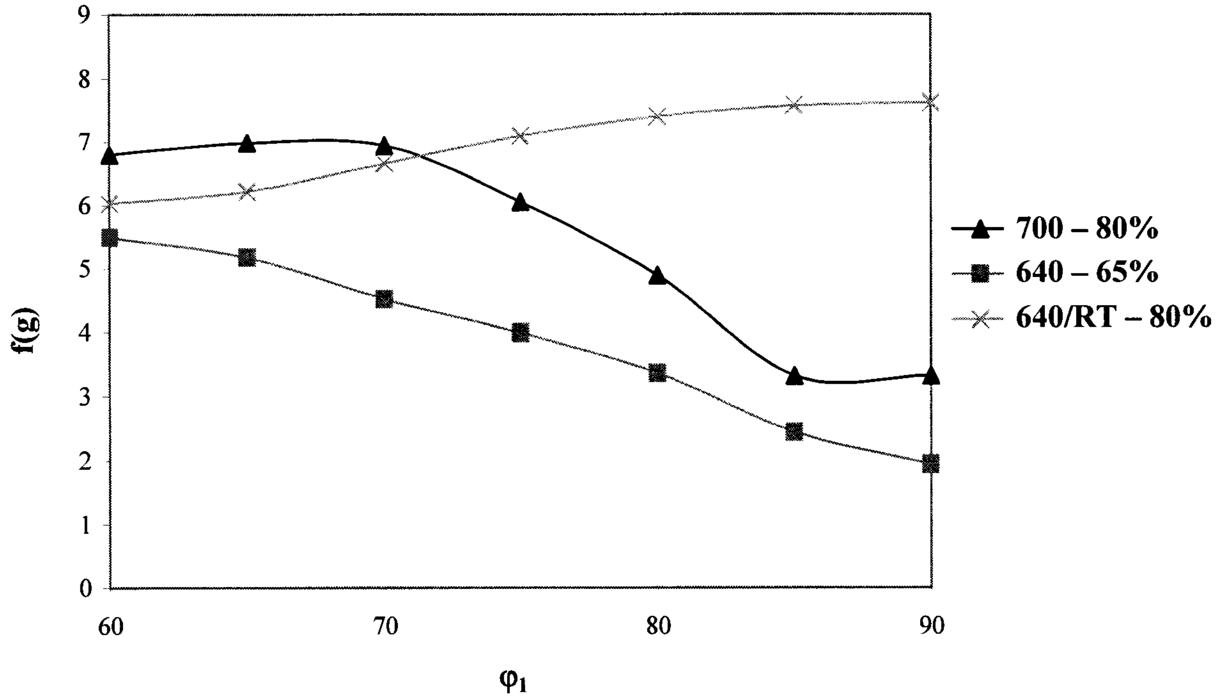

Figure V.6. a) RD and b) ND skeleton lines associated with the textures presented in Fig. IV.16. The influence of deformation temperature and rolling reduction on the main recrystallization texture components of the ELC(Cr) steel in the CHGS condition can be seen. After 4 hours of annealing at 700°C, using a heating rate of 1.5×10^{-2} K.s^{-1}.

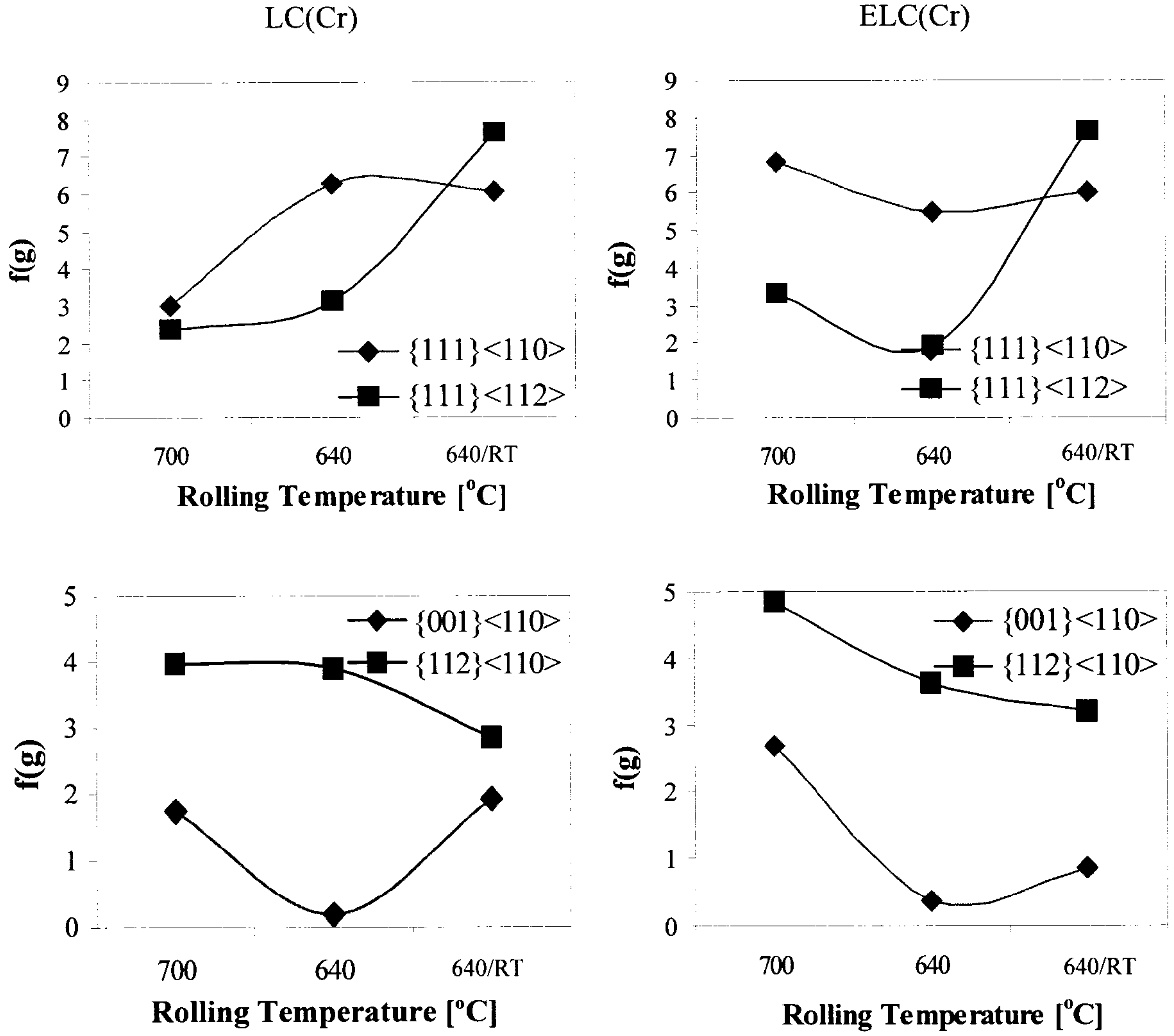

Figure V.7. Effect of rolling temperature on the intensities of the main recrystallization components in the LC(Cr) and ELC(Cr) steels (CHGS condition). After 4 hours of annealing at 700°C, using a heating rate of 1.5x10^{-2} K.s^{-1}. Taken from the textures presented in Fig. IV.16.

When the deformation temperature is reduced to 640°C, the RD fibre and the rotated cube component are virtually eliminated on annealing. However, there is a rotation towards the rotated Goss component {110}<110>, which is detrimental to the formability. The latter is not typical of recrystallization textures, so that its presence was initially thought to be a result of experimental error; but the further measurement of two additional samples confirmed the reliability of this observation. On the other hand, the intensity of the ND fibre is increased, being 2 times higher than that of the unexpected {110}<110>. At this point, it must be emphasized that the improved texture resulting from slow heating is important as it enables the production of materials for drawing applications.

In the case of the WR+CR materials, the recrystallization textures did not display significant intensity changes compared to those produced using the higher heating rate. This could be because the driving force for recrystallization is 4 times higher than in the warm rolled specimens. However, a slight improvement in the continuity of the ND fibre was observed. It is clear that the additional 40% cold rolling reduction has a considerable influence on the recrystallization texture and that the use of a low heating rate is essential to improving the texture.

The use of a slow heating rate provides enough time to allow the precipitation of C and N and the coarsening of such precipitates before the onset of recrystallization. C and N in the form of coarse precipitates will not interfere with the nucleation and growth of {111} grains and will not make an important contribution to the volume fraction of random orientations nucleating on them. Furthermore, the reduced amount of solute carbon during annealing prevents its interaction with manganese, with which it forms complexes that inhibit recovery by retarding the climb rate of dislocations (a solute drag effect) [12]. This prolongs the incubation period for recrystallization and retards the growth rate of recrystallized grains, reducing the initial nucleation advantage of the γ-fibre orientations and thus affecting the formability of the steel [98].

V.2.2.2 Hot band grain size

The beneficial effect of refining the hot band grain size on the final formability has been widely demonstrated in the case of cold rolled and annealed steel sheet [42, 88]. There are also a number of references that relate the amount of in-grain shear bands to the final formability [66, 112, 117]. These two trends are opposed in the sense that shear band frequency normally increases with initial grain size, thus promoting the presence of a larger number of <111>//ND grains. In this way, both coarse and fine HBGS's can be expected to lead to good formability, but in different ways.

The deformation textures in the steels warm rolled at 640°C were similar for the 18 and 30μm HBGS samples, but the texture intensity was 1.5 times higher in the case of the finer HBGS material. This difference can be related to the lower intensity of random orientations in the finer grained material. The intensity difference was maintained during recrystallization, indicating that many deformed γ grains are replaced by recrystallized grains of the same type. In the case of the recrystallization textures, there are few differences in either the intensity or the distribution of the α and γ fibres between the two starting conditions.

Refinement of the HBGS increases the intensity and continuity of the ND fibre and does not cause the rotated Goss component to appear. However, it also increases the intensity of the RD fibre, creating a strong maximum between {113}<110> and {112}<110>. It is possible that the lower solution temperature of 930°C employed before warm rolling affects the distribution and state of the carbon, favouring the presence of a higher density of carbides. A higher number of carbides can interact with dislocations, increasing the driving force for the recrystallization of all fibre orientations. This could reduce the "randomization" of the recrystallization orientations about the RD fibre. In fact, a slight increase in the normalized dislocation density is reflected for this condition in comparison with the CHGS steel. Another possible explanation is related to the higher density of grain boundaries caused by refinement of the HBGS. This could have an effect similar to that of the higher density of carbides by restricting dislocation movement during deformation.

After refinement of the HBGS, the recrystallization textures of the WR+CR steels experienced effects similar to those observed in the WR materials. That is, a more intense ND-fibre was displayed, accompanied by a strengthened RD-fibre.

V.2.3 Anisotropy

The calculated r-values determined on the warm rolled materials after annealing at the medium heating rate of $2Ks^{-1}$ were all below 1. Nevertheless, the current experimental steels displayed higher values than those of the previous investigations [9, 14, 112]. Additional cold rolling increased the r-value to 1.1 in the case of the WR+CR material. It is clear from these results that the r-value increases as the deformation temperature is lowered and the amount of reduction is increased.

The formability was further increased when a lower heating rate of $1.5x10^{-2}K.s^{-1}$ was utilized. R-values of 1.2 and 1.3, respectively, were obtained for samples i) warm rolled at 640°C; and ii) warm rolled at 640°C and then cold rolled 40%. This illustrates once more the desirable effect of a low heating rate and of additional cold rolling reductions. The fact that an r-value of 1.3 can be produced in a warm rolled low carbon steel with only 40% additional cold rolling is important. However, an r-value of 1.2 obtained solely by warm rolling is even more important, as it opens the possibility for the industrial production of warm rolled low carbon steel with good formability.

Finally, when the effect of the HBGS is considered, it can be seen that there is no important difference in terms of r-value between the CHGS and FHGS materials. Samples that were warm rolled 65% at 640°C and annealed at 700°C using the lower heating rate had calculated r-values of 1.2, which is acceptable for a steel of commercial quality. Moreover, the achievement of low planar anisotropy in the finer HBGS steel is important as uniform deformation can be achieved in combination with acceptable formability. The similar r-values associated with the two conditions seem to be due to the presence of the retained α-fibre in the FHGS material and of the unbalanced γ-fibre in the CHGS steel. Concurrently, the planar anisotropy, represented by a lower Δr, was significantly better in the finer HBGS sample.

The effect of HBGS on anisotropy was confirmed in the WR samples that had been subjected to additional CR. The further cold rolling improved the mean r-value to 1.3, again for both initial grain sizes, and made the distribution of the Lankford coefficient more homogeneous. Nevertheless, the distribution established by warm rolling was maintained, as was shown in Fig. IV.20. Finally, it should be added that the effect of HBGSs finer than those employed in this work should be studied to explore their effects on the normal anisotropy.

V.3 Microtexture Analysis

The present section is intended to establish the texture formation mechanism that controls evolution of the recrystallization texture during the production of WR and WR+CR materials. The order of this analysis is as follows: first, the characteristics of the substructure produced by the different sets of deformation conditions are presented; then the characteristics of nucleation, including the number, location and type of nuclei, are considered. Finally, the evolution of the texture is reviewed in terms of changes in the intensities of the individual components of the γ and α fibres and of the remaining R component during recrystallization.

V.3.1 Substructure

The misorientation profiles displayed in Figs. IV.26 to IV.33 showed that the order of increasing misorientation is $\gamma > R > \alpha$ for all conditions. These observations are summarized in Table V.1, where the average values of these misorientations are presented.

Table V.1. Average misorientation values.

Condition	γ	R	α
65%WR@640°C-CHGS	1.0	0.7	0.4
65%WR@640°C-FHGS	1.1	0.7	0.5
65%WR@640°C-FHGS + 40%CR	1.6	1.4	0.6
IF-65%WR@640°C	2.4	2.0	0.8

It can be seen that there are no important differences between the average misorientation values of the 65%WR samples in the CHGS and FHGS conditions. However, Table V.2 shows that the spreads in the data, calculated as a "standard deviation", associated with the α and γ components in the FHGS material are higher than in the former. This means that it has a more developed substructure and consequently contains a larger number of *potential* nucleation sites. The situation is opposite for the R orientation, which exhibits lower values of the above-mentioned statistical attributes. This increase in the degree of misorientation for the α and γ orientations, caused in this case by refinement of the hot band grain size, can be identified by the larger number of high peaks in the point-to-point misorientation profiles.

Table V.2. Standard deviations of the misorientation values.

	Standard Deviation		
Condition	γ	**R**	α
65%WR@640°C-CHGS	1.2	0.9	0.3
65%WR@640°C-FHGS	1.3	0.7	0.5

The further 40% cold rolling reduction in the case of the WR+CR-FHGS material increases the degree of misorientation, principally in the γ and R components; the α components, on the other hand, showed little change.

In the case of the IF steel, the level of misorientation is approximately 1.5 times higher than in the WR+CR specimens and more than 2 times higher than in the WR materials. This difference translates into a larger number of potentially successful nuclei and illustrates the large differences between low carbon and interstitial free steels, even before recrystallization.

V.3.2 Nucleation

The nucleation features illustrated in Figs. IV.35 to IV.39, such as the location, type, and number of α, γ and R nuclei, are described here, focusing on the differences between grain boundary (GBN) and grain interior (GIN) nucleation.

The experimental LC(Cr) and ELC(Cr) materials exhibited predominantly GBN nucleation. Refinement of the hot band grain size increased the amount of GIN nucleation slightly and raised the volume fraction of γ orientations, both at grain boundaries and at grain interiors; the latter was at the expense of the R components. The behaviours of the samples with additional cold rolling were similar; i.e., both the extent of GIN and the volume fraction of γ type nuclei were further increased. By contrast, the nucleation frequency of the α component was reduced by refinement of the HBGS. Furthermore, it was totally inhibited in the grain interiors in the WR+CR material. However, it increased slightly at the grain boundaries. Here it is convenient to emphasize that the current results correspond to the early stages of recrystallization and that the further changes in the density of each component will be considered in section V.3.3.

In the case of the IF steel, the nucleation behaviour differed totally from that of the ELC(Cr) specimens, in both the CHGS and FHGS conditions. In the former steel, the more highly developed substructure offered a larger number of nucleation sites in the interiors of the grains, causing the GIN/GBN ratio to increase from approximately 0.3 in the ELC(Cr) steel to 1.8. Another important characteristic to note was the small amount of α at both types of nucleation site.

The results obtained up to this point confirm that a finer initial grain size reduces the shear band frequency. However, the reduced density of shear bands did not reduce the amount of {111} in-grain nucleation. Instead, the fraction of γ grains nucleating *within* the grains was unexpectedly higher for the finer HBGS material. This observation does not necessarily indicate that shear bands are unimportant, rather it is the *nature* more than the *number* of shear bands that has to be considered when nucleation sites and types of nuclei are being considered. Long shear bands of moderate intensity serve as sites for nucleation of the <111>//ND fibre [14], while intense shear bands contribute to the development of the {110}<001> orientations or Goss component [4, 63, 64]. Concurrently, the second type of shear band results from initially coarse-grained hot bands. A compromise, then, has to be found between grain size and the number and nature of shear bands that improves the final anisotropy.

Another important output from these results is that, even though the volume fraction of grains containing shear bands is only slightly higher in the IF steel [49], the distribution of nucleation sites is totally opposite. One explanation for this has been proposed previously in terms of the morphologies of the shear bands [49]. However, what is changed is the GIN/GBN ratio and the volume fraction of γ grains, not the *number* of nucleation sites. It is the IF steel that has the lower number of nuclei. Considering this, it is suitable to say that shear bands, depending on their number and principally on their *nature*, cause important amounts of flow localization in the interiors of the grains. This produces a large amount of fragmentation, which is reflected in the increase in the level of misorientation and in the more developed substructure exhibited by this material. Nevertheless, the reduction in the number of grain boundary nuclei suggests that such flow localization is shifted from the boundaries to the interiors of the grains. It is clear then that LC(Cr) and ELC(Cr) steels display behaviours that differ markedly from that of the IF material and that special attention has to be paid to the nature of the shear bands.

V.3.2.1 Grain boundary nucleation

The distribution graphs of nucleation at grain boundaries presented in Fig. IV.36 show that γ and R grains nucleate principally at the boundaries of γ and R type deformed grains, respectively, and that α–α boundaries do not contribute in a significant way to the nucleation process. Refinement of the HBGS increases the number of γ nuclei, mainly at γ–γ, γ–α and γ-R boundaries. At this point, it is possible to say that the number of deformed γ grains is extremely important, as their boundaries are the main nucleation sites of grains of the same type. The fact that the last statement also applies in the case of the R orientations makes the former even more important. Further cold deformation of the WR material increases the volume fraction of γ grains after recrystallization. Nevertheless, the distribution of nuclei, initially established by WR, is maintained after CR.

When the main components of the γ fibre are considered individually, it can be seen that {111}<112> is favoured by refinement of the HBGS. However, the main increase occurs at γ–α boundaries. This might be related to the increase in the driving force for recrystallization caused by the increase in dislocation density. The latter raises the energy of the α components to a level at which they participate more actively in the nucleation process. Note that the additional cold deformation favours the {111}<110> and the {111}<112> orientations over the γ_3, as shown in Fig. IV.37.

V.3.2.2 In-grain nucleation

The distribution of nuclei in the interiors of the deformed grains was similar for the WR and WR+CR experimental conditions. The degree of substructure developed within the different components has a clear influence on in-grain nucleation. The γ and R components, which display higher average misorientation values, are the principal orientations nucleating within the grains. Here the nucleation behaviour is similar to that observed at the grain boundaries: deformed γ grains are the principal sites of γ nuclei and deformed R grains are the sites for the R components.

Refinement of the HBGS increases the number of γ and R nuclei in deformed γ and R grains, respectively. Again, this is related to a more developed substructure. When additional cold rolling is employed, the volume fraction of total *in-grain* nucleation decreases. Nevertheless, the ratio of the γ fibre with respect to all the other orientations increased. This was explained above in terms of the nature of the shear bands and its implications on the level of fragmentation.

When the in-grain nucleation of {111}<110> and {111}<112> was considered, it was clear that deformed γ orientations were the preferential sites for the nucleation of γ grains. These results were illustrated in Fig. IV.39. When the HBGS was refined, the volume fraction of {111}<112> increased. On the other hand, in the case of the 65%WR+40%CR-FHGS samples, additional cold rolling caused a decrease in all the in-grain orientations, as additional deformation favours grain boundary nucleation. Nevertheless, the {111}<112> still displayed the higher volume fraction. Regarding the IF steel, the contrast with respect to the low carbon steels was enormous, as up to 65% of the total γ orientations were nucleated principally *within* the deformed γ grains, compared to the approximately 25 to 30% observed in the experimental steels. In the former case, the {111}<112> was twice as intense as the {111}<110>. Furthermore, the volume fraction of the γ_3 components was as high as that of the former, indicating that γ orientations near the {111}<112> were also favoured.

The measured orientations in the samples in the early stages of recrystallization contained γ grains that had nucleated and grown both in the interiors and at the boundaries of γ-fibre grains. This observation confirms the importance of deformed γ-fibre grains in the nucleation and growth of new, strain-free γ grains.

V.3.3 Texture evolution

As mentioned in the above section, the numbers of nuclei of each orientation are closely linked to the previous deformation microstructure. This implies that, if no other texture formation mechanism takes part during recrystallization, the final texture will be determined by the way in which the various orientations were nucleated initially, i.e., by oriented nucleation.

The textures of the warm rolled specimens (65%WR-CHGS and 65%WR-FHGS) and those cold rolled an additional 40% (65%WR+40%CR-FHGS), shown in Fig. IV.11, displayed intensities that are similar to those illustrated in Fig. 1 of Ref. [47] for a cold rolled ULC steel subjected to reductions of 70 and 95%, respectively. These textures were reproduced in Fig. II.8. As the texture formation mechanism associated with the latter (i.e. 95% reduction) was suggested to be selective growth, it is tempting to consider the possibility that the same mechanism plays a role in the development of the current 65% WR and 80% WR+CR recrystallization textures.

However, the close resemblance between the early and final recrystallization textures in Figs. IV.41 and IV.42 and the presence from the early stages of recrystallization of the {113}<471> and {554}<225> orientations indicates that oriented growth is not the principal mechanism that controls texture formation. Although the strong α fibre with a maximum at {112}<110> could in principle take part in selective growth, there is not much difference between the texture of the recrystallized grains in the

77% recrystallized sample shown in Fig. IV.41c and the fully annealed texture of the same material. This statement also applies to the recrystallized grains in the 70% recrystallized WR+CR material in Fig. IV.42c and the fully annealed texture. Thus, it is apparent that reductions of 65% and 80%, particularly when applied in part by warm rolling, are insufficient for bringing about selective growth. This is consistent with the conclusions of the authors of Ref. [47], who said that reductions as high as 95% were required.

Due to the late recrystallization of the α-fibre, it is possible that selective growth can contribute to the formation of texture at the *end* of the recrystallization process. This is confirmed in Figs. IV.41 and IV.42, where the φ_2=45° sections of the ODF show that the unrecrystallized component in an approximately 70% recrystallized sample is mainly composed of the {112}<110> and rotated cube orientations, while the recrystallized component is composed of a fibre running from {112}<110> to {554}<225>.

As mentioned earlier, during selective growth, some grains grow more quickly than others. In the case of steel, interfaces characterised by <110>26.5° misorientations have such enhanced mobilities. Although overall measurements of the number of such boundaries have been carried out previously [118, 119], little information is available for particular nucleus orientations. Consequently, some attention was paid in this work to the possible contribution of high mobility boundaries to the final texture. For this purpose, the <110>26.5° boundaries were identified on various orientation maps, such as the one shown in Fig. V.8 pertaining to the later stages of recrystallization.

It can be seen that grains of {111}<112> orientations are consuming {112}<110> oriented deformed grains. However, the number of such grains is not particularly large, as there is little change in the recrystallization texture between the approximately 70% recrystallized and fully annealed conditions. Additionally, Fig. V.8 shows that other γ fibre and random orientations are also consuming the deformed {112}<110> grains. Furthermore, a given {112}<110> grain can even be consumed by existing {112}<110> recrystallized grains or by grain coalescence.

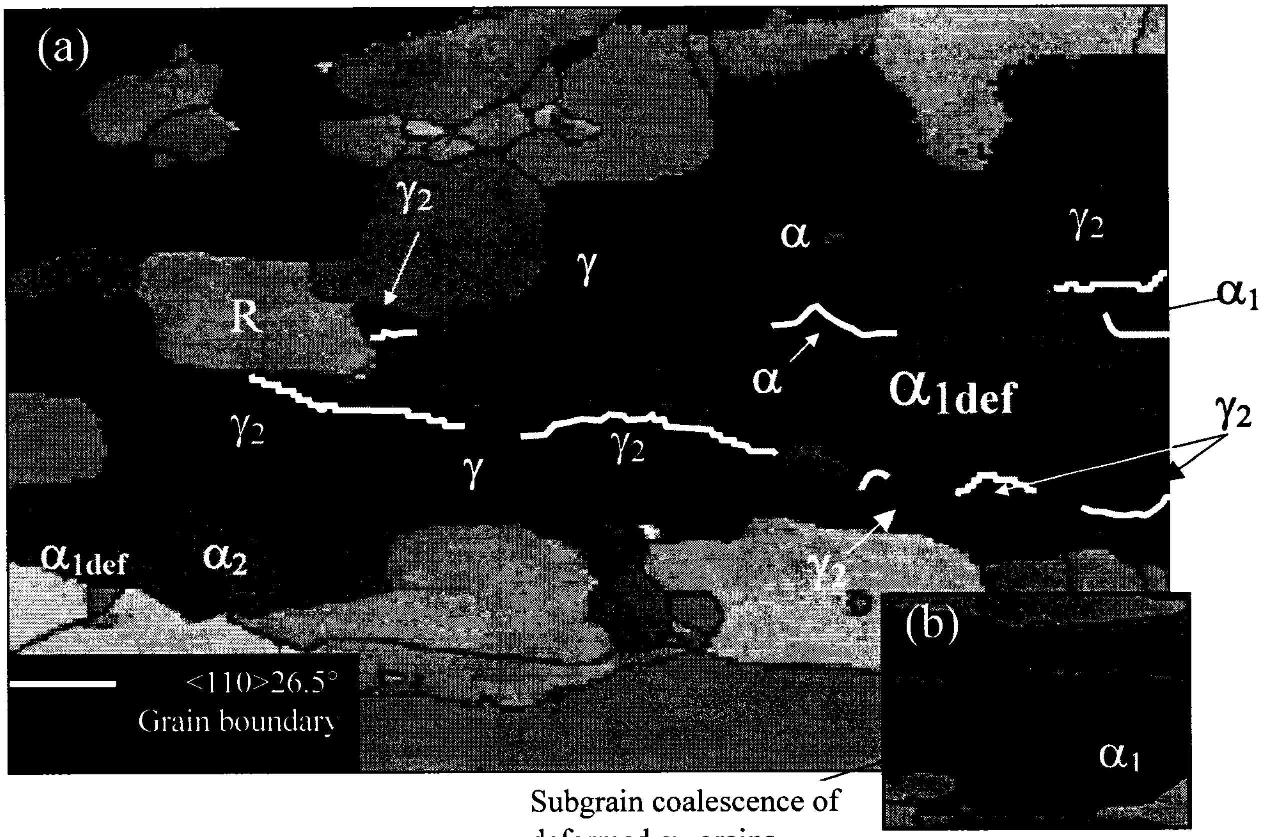

Subgrain coalescence of deformed α_1 grains

Figure. V.8. Orientation map for the 70% recrystallized WR+CR sample. a) <110>26.5° boundaries, in white, separate growing grains of the following orientations: $\alpha = \{100\}\langle 110\rangle$, $\alpha_2 = \{hkl\}\langle 110\rangle$, $\gamma_2 = \{111\}\langle 112\rangle$, $\gamma = \{111\}\langle hkl\rangle$, and R = random from deformed $\alpha_1 = \{112\}\langle 110\rangle$ grains, which are being consumed. The <110>26.5° misorientation was calculated using deviations of up to 15° for the axis and 5° for the angle, respectively. b) deformed $\alpha_1 = \{112\}\langle 110\rangle$ grain being consumed by subgrain coalescence. High angle grain boundaries (>10°) are in black and all lower angle boundaries are in grey.

The textures corresponding to the point at which recrystallization is just complete, Fig. V.9, confirm that selective growth is not the mechanism controlling the evolution of texture. Here it is shown that no changes in the texture distribution occur between the just recrystallized and fully recrystallized textures presented in Figs. IV.16 and IV.17. The ODF of the WR+CR material (Fig. V.9c) illustrates the positions of the {113}<471> and {554}<225> components. Some questions could arise with respect to the WR samples because of the detectable differences between the just recrystallized and fully annealed textures. However, these differences can be justified in terms of the small number of grains surveyed by EBSD at 100% recrystallization, 210-250 grains, in contrast to the 1700 grains covered in the WR+CR sample. The number of recrystallized grains depends on the initial number of nuclei, which is significantly affected by the amount of deformation undergone by each sample. Fig. V.10 shows how refinement of the HBGS raises the number of nuclei by a factor of 2. It also illustrates that the application of an additional CR reduction of 40% increases the number of nuclei by a factor of 7.

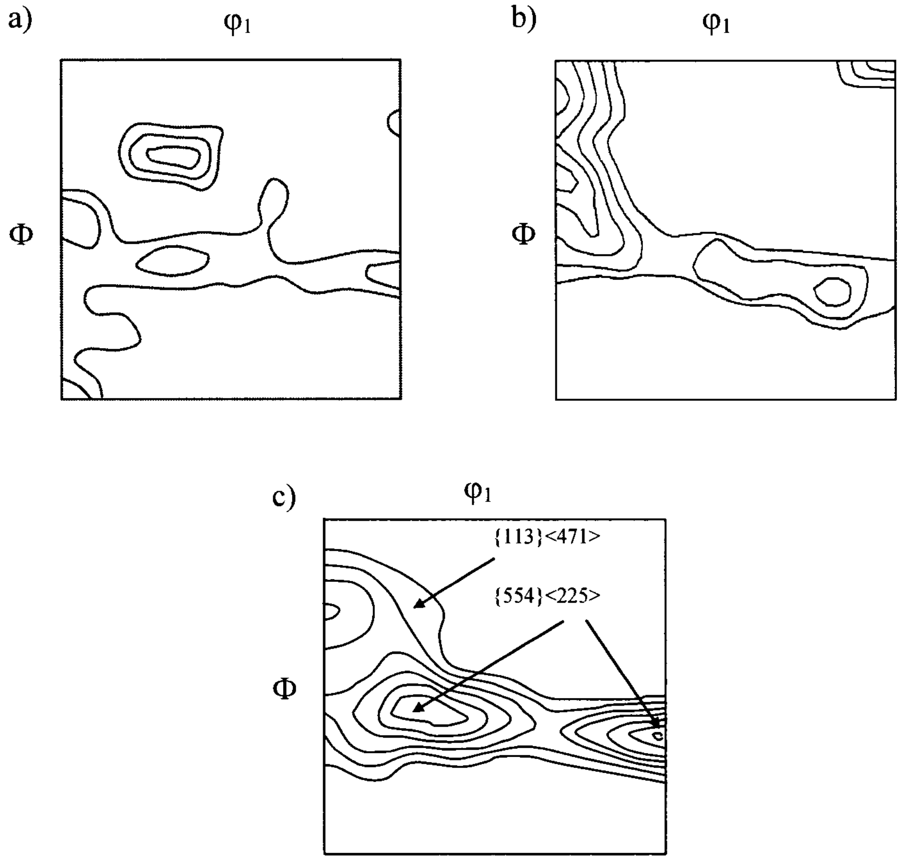

Figure V.9 Textures corresponding to the point at which recrystallization is just complete: a) 65%WR-CHGS, b) 65%WR-FHGS and c) 65%WR+40%CR-FHGS. Levels: 2,3,4,.......

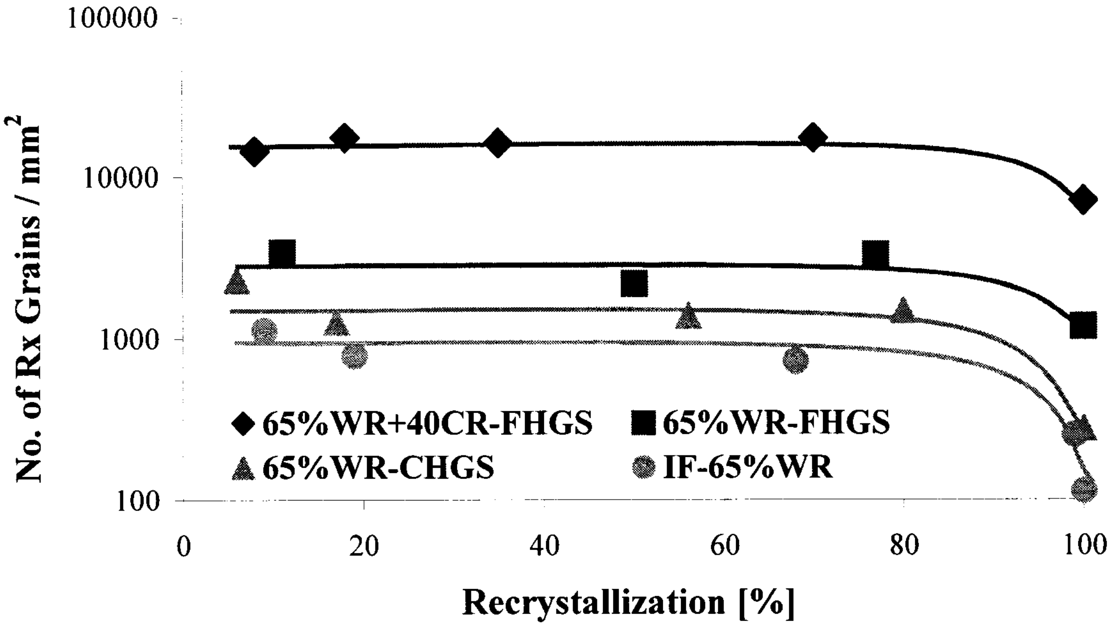

Figure. V.10. Number of recrystallized grains per unit area in the WR, WR+CR, and IF samples at different stages of recrystallization.

Refinement of the HBGS increases the number of initial nuclei and the final number of recrystallized grains. On the other hand, the fraction of successful nuclei that become recrystallized grains seems to be independent of the amount of deformation. For example, in the case of the FHGS materials, the WR and WR+CR samples display nucleus conversion efficiencies of about 40% if site saturation nucleation is assumed, Fig. V.10.

V.3.3.1 Microtexture changes

The volume fraction of γ fibre and of randomly oriented grains was higher than of α fibre grains during the entire recrystallization process for the three selected experimental conditions. This indicates that the former orientations have a nucleation advantage over the latter one, see Figs. IV.44 a, b and c. Refinement of the HBGS reduces the volume fraction of the R component and increases that of the γ and α orientations, which is consistent with the changes observed in the average misorientation values. On the other hand, the application of 40% additional cold deformation causes a slight increase in the γ at the expense of the R and α orientations. Finally, when the volume fractions of the γ and R components are compared for the WR+CR samples and the IF steel there is little difference, although there is less α in the latter. This accounts for the better formability properties of the interstitial free material. The kinds of random orientations present also make important contributions to the improved formability.

As illustrated in the 3D ODF's of Fig. V.11, the R components surround the γ fibre in the case of the IF steel, Fig. V.11d, and their intensities are low compared with those of the fibre, while there is much more spread in the WR textures, Figs. V.11a and b. Even though such spread is reduced by the increased deformation (WR+CR), Fig. V.11c, the strong α fibre prevents the formability from being improved.

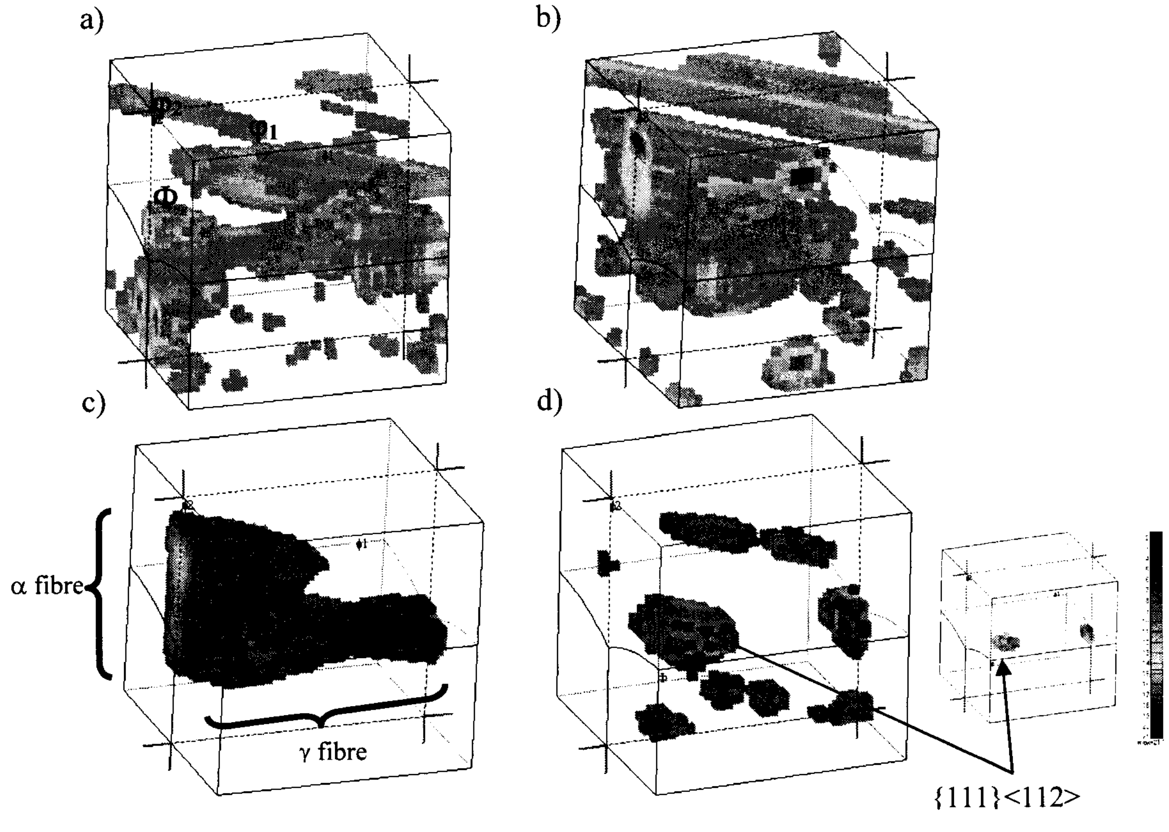

Figure.V.11. 3D ODF's of fully recrystallized samples: a) 65%WR-CHGS, b) 65%WR-FHGS, c) 65%WR+40%CR-FHGS and d) IF steel.

According to the present results, the initial distributions of the volume fractions are maintained throughout recrystallization without important changes for all components and all materials. This again makes clear that the formation of the principal texture components is controlled by oriented nucleation.

V.3.3.2 Grain size

The large difference in the number of nuclei displayed in Figs. IV.45 to IV.47 for the γ and R orientations compared with those for the α fibre is noteworthy. The most significant case is that of the WR+CR material, with a nucleation rate approximately 8 times higher for the γ and random orientations. This clearly demonstrates that a nucleation advantage applies to these two components. Nucleation only takes place in regions with high local misorientations and only nuclei characterized by high misorientation angles with respect to the adjacent deformed material have the necessary mobility to become recrystallized grains [15]. Both the γ and R orientations possess these characteristics. An orientation map for the WR+CR material at 8% recrystallization is illustrated in Fig. V.12, together with a grain boundary map for the same sample. The deformed γ and random orientations display higher substructure contents and consequently higher in-grain misorientations; these can be translated into larger driving forces for recrystallization and privileged conditions for grain growth, respectively. The situation for the α orientations is totally opposite, with only a small amount of in-grain substructure present.

The nucleation advantages of the γ orientations determine their volume fractions in the final recrystallization texture. If these advantages did not exist, then the α fibre would have a similar weight. This can be clearly observed in Fig. V.13, where the grain size distribution at a volume fraction pertaining to the early recrystallization texture was subtracted from that corresponding to 70-80% completion of the same process. In this representation, negative values reflect the number of nuclei that have become grains, in agreement with the current size criterion of 2μm.

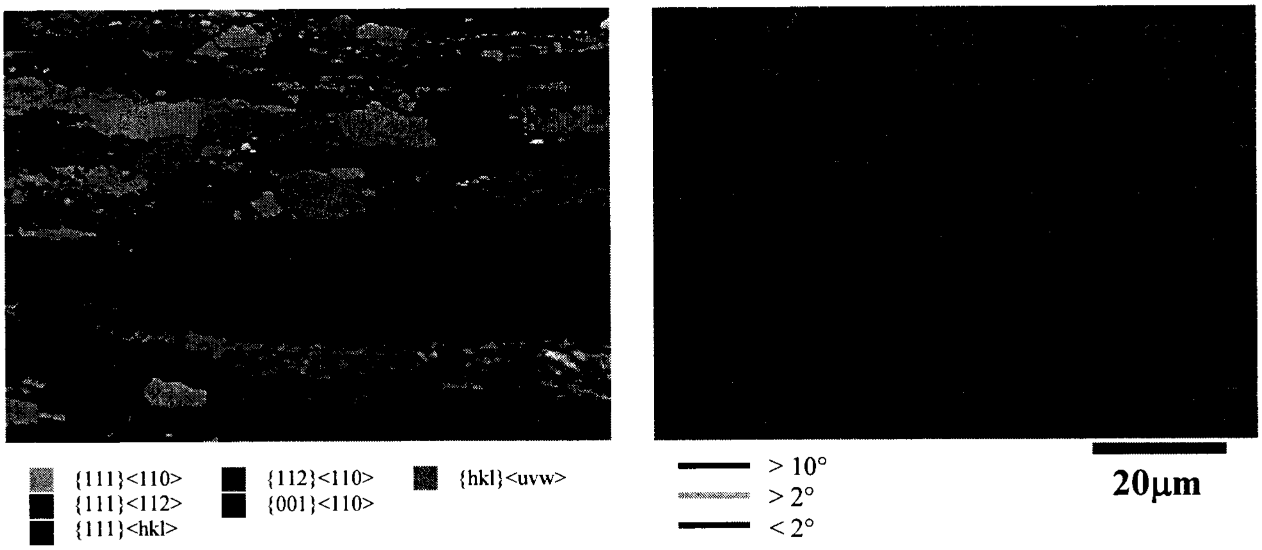

Figure. V.12. Orientation and grain boundary maps showing the differences in density of the in-grain substructure for the main orientations.

The trend lines in Fig. V.13 display the changes in grain size distribution between early and late recrystallization (before the end of recrystallization) for the γ and random orientations. The α fibre can be seen to follow a similar trend but with a lower slope. By contrast, Fig. IV.48 shows that the average grain sizes of the main components are slightly higher for the γ and random orientations throughout recrystallization. This confirms the view [15] that earlier nucleation favours the growth of these two orientations.

V.3.3.3 Growth rates

The growth rates were individually determined for the γ, α and R components by measuring the interfacial areas between the recrystallized and deformed grains of each main orientation.

The growth rate is reduced by refinement of the HBGS for all components. However, a larger reduction is caused by the additional cold rolling. This is closely related to the refinement of the recrystallized grain size.

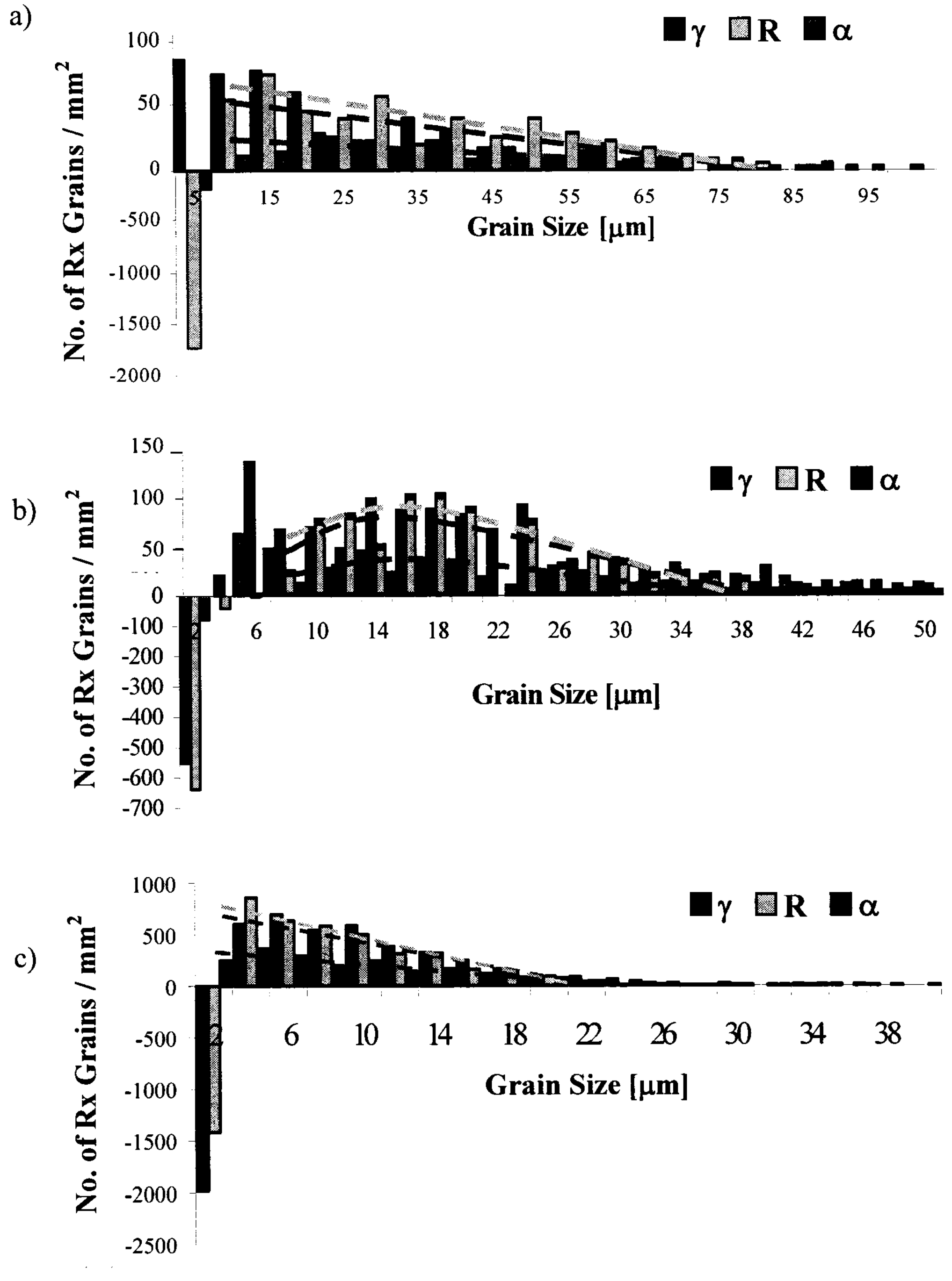

Figure V.13. Grain size distributions of the main orientations in the experimental materials: a) 65%WR-CHGS, b) 65%WR-FHGS and c) 65%WR+40%CR-FHGS.

The similar growth rates for the γ and random components, displayed in Fig. IV.49 for all three experimental conditions, confirm that oriented nucleation was more important than growth selection, as concluded in the previous section. These components exhibited the same growth rates, revealing that not one of these sets of orientations possessed a growth advantage. This further supports the view that texture evolution during the recrystallization of the present materials is primarily influenced by the oriented nucleation mechanism.

CHAPTER VI

VI CONCLUSIONS

1. As suggested by earlier workers, the addition of chromium reduces the magnitude of strain rate hardening, broadening the flow stress/temperature peak by comparison with that for a LC steel. This results in the extension upwards of the dynamic strain aging range by 350°C to temperatures above the normal flow stress peak.

2. The volume fraction of grains containing shear bands increases with a decrease in the deformation temperature and an increase in the amount of reduction. On the other hand, refinement of the HBGS slightly reduces the shear band fraction. A further cold rolling reduction significantly increases the shear band content. Differences between the CHGS and FHGS materials observed in the case of the WR grades are maintained in the WR+CR condition.

3. The dislocation density increases as the deformation temperature is reduced. It is also raised by refinement of the HBGS and particularly by imposing an additional cold rolling reduction of 40%. The latter accounts for an increase of up to 4 times with respect to that produced by WR to similar strain values. Thus, the amount of reduction is of considerable importance in the warm rolling process; nevertheless, it has less

effect than the same amount of cold reduction. The large differences between WR and WR+CR deformation can be attributed to a decrease in the solute carbon-dislocation interaction and the occurrence of dynamic recovery at WR temperatures.

4. Carbon contents in the range from 0.02 and 0.04%, in the case of the present experimental materials, lead to similar deformation and recrystallization textures and consequently to similar expected levels of formability during deep drawing.

5. The textures produced by warm rolling and annealing using a medium heating rate of 2 $K.s^{-1}$ contained a dominant RD fibre in all three steels. When chromium is added, the intensity of the ND fibre is increased. However, it also promotes the presence of a strong rotated cube component. The ND fibre is also increased when the rolling temperature is decreased and is further strengthened when an additional cold rolling reduction of 40% is applied.

6. The use of low heating rates increases the r-value to levels suitable for industrial production; these amounted to about 1.2 for the warm rolled material and 1.3 for the warm rolled plus cold rolled material. The low heating rate may enhance the precipitation and coarsening of C and N compounds before the onset of recrystallization.

7. Additional cold rolling reduction increases the mean r-value and increases the homogeneity of the distribution of the Lankford parameter in the plane of the sheet (i.e. it reduces Δr). However, it does not change the nature of the original distribution established by the previous warm rolling. This means that the initial state of deformation determines the type of final texture, which can be enhanced but not changed by further deformation.

8. Finer HBGS's yield higher numbers of γ grain boundary nuclei, which can be further increased by an additional 40% CR reduction. These remarks also apply to the α grains. Both of the increases occur at the expense of the R oriented grains.

9. The deformed γ and randomly oriented grains display higher substructure contents than the α grains. Consequently, they have higher in-grain misorientations, which translate into larger driving forces for the nucleation of the former two components.

10. The presence of deformed γ grains is important as the grain boundaries between these and other γ, R and α grains, in this order of importance, serve as the nucleation and growth sites for γ-fibre nuclei. The opposite statement is valid for the random orientations; they nucleate at R-type grain boundaries and some of them grow by consuming γ grains.

11. Nucleation in the current experimental LC steels with Cr additions occurs almost totally at grain boundaries, with up to 80% of the nuclei located at these sites. Additional cold rolling raised the grain boundary nucleation ratio to 90%. A considerable difference exists between the experimental steels and a reference IF material, as there was 60% *in-grain* nucleation in the latter.

12. The decrease in the volume fraction of shear bands caused by refinement of the HBGS does not reduce the amount of in-grain nucleation of the γ grains. This suggests that the *nature* and not only the *number* of shear bands determines the density of sites available for this type of nucleation. This observation is supported by the similar numbers of SBs observed in the current experimental steels and in the IF material under similar deformation conditions; such similarities are inconsistent with the differences in the distribution of their nuclei. This indicates that the occurrence of shear banding is not the only factor that has to be considered in attempts to improve warm rolling textures.

13. Refinement of the HBGS doubles the volume fraction of nuclei. On the other hand, a further cold reduction of 40% after a 65% warm rolling reduction increases the number of recrystallization nuclei by a factor of up to 7. However, the ratios of volume fractions of nuclei that succeed in becoming recrystallized grains are independent of

the amount of deformation in samples in the same state of deformation; e.g., the 65%WR-FHGS and the 65%WR+40%CR-FHGS.

14. During the late stages of the recrystallization of warm rolled low carbon steels, growing grains of {111}<112> orientations consume {112}<110> deformed grains. The former maintain <110>26.5° relations with the latter. However, {112}<110> deformed grains are also consumed by other γ fibre grains as well as by randomly oriented ones. A further fraction of the deformed {112}<110> grains is eliminated by the coalescence of {112}<110> subgrains.

15. The growth rates exhibited by the γ and randomly oriented grains are similar and the volume fractions of these components remain approximately constant during recrystallization. These observations confirm that oriented nucleation is the major texture formation mechanism involved in the recrystallization of warm rolled low carbon steels.

16. The recrystallization texture and consequently the formability level is essentially established in the early stages of recrystallization. The thermomechanical process and heating mode before the onset of recrystallization determine the final distribution of the main crystallographic orientations. These can be further enhanced by subsequent grain growth.

CHAPTER VII

VII SUGGESTIONS FOR FUTURE WORK

As was described above, the initial distribution of nuclei determines the recrystallization texture. Thus, all changes aimed at improving these textures have to concern this stage of processing. It is clear that the effects of solute carbon and of fine precipitates have to be minimized during recovery by enhancing the precipitation of the former and the growth of the latter. It was also concluded in this work that the effect of chromium on DSA is optimized at a level of 0.8%Cr and that the amount of deformation has only a limited effect on texture improvement at warm rolling temperatures.

Thus, the most feasible ways of improving the formability of low carbon steels appear to be by extending the DSA range to still higher temperatures and by increasing the dislocation density. Both effects involve the state of the carbon during rolling. Consequently, further attention should be placed on the precipitation kinetics of chromium-carbon particles, with the aim of increasing their interaction with dislocations during deformation.

The precipitation of carbides after warm rolling, should also be encouraged by the very slow cooling of coils.

CHAPTER VIII

VIII STATEMENT OF ORIGINALITY AND CONTRIBUTIONS TO KNOWLEDGE

1. Low heating rates during recrystallization have been shown to improve the formability properties of *warm rolled* low carbon steels.

2. Extensive electron backscattering measurements were carried out to obtain information about nucleation and the evolution of individual orientations in *warm rolled* low carbon steels.

3. The texture formation mechanism during the recrystallization of warm rolled low carbon steels was systematically established, demonstrating that the recrystallization texture is largely determined by the initial distribution of nuclei.

4. The amounts of grain boundary and in-grain nucleation of the α, γ and R orientations were measured in warm rolled LC and IF steels. This allowed the importance of each of these to be established. It also demonstrated that the nucleation characteristics of the two types of materials are substantially different, indicating that factors in addition to the volume fraction of grains containing shear bands are of importance.

5. The effect of HBGS and of additional cold rolling on the volume fraction of grains containing shear bands was measured. Similar observations were also obtained regarding the initial distribution of nuclei, the evolution of individual components, and the final recrystallization texture.

6. The changes in average grain size and the grain size distributions of individual orientations during the recrystallization of warm rolled low carbon steels were measured.

REFERENCES

[1] P.R. Cetlin, S. Yue, J.J. Jonas and T.M. Maccagno. Metallurgical Transactions A 1993; 24A:1543-1554.

[2] A. Najafi-Zadeh, J.J. Jonas and S. Yue. Metallurgical and Materials Transactions A 1992;23A:2607.

[3] L.M. Perera, I.A. Raul, J.D. Boyd and S. Saimoto. In: J.J. Jonas, T.R. Bieler and K.J. Bowman, Advances in Hot Deformation Textures and Microstructures., The MMMS: 1994. p.27.

[4] K. Ushioda, H. Ohsone and M. Abe. In: 6th Int. Conference on Textures of Materials, Japan: 1981. p.829.

[5] W.B. Hutchinson and K. Ushioda. In: 7th Int. Conf. Texture of Materials, Netherlands: 1984. p.409.

[6] T. Suzuki. Transactions ISIJ 1985;25:1237-1243.

[7] T. Nakamura. In: Thermec 88, Tokyo: 1988. p.644.

[8] P.A. Bagshaw and R.J. Kimber. In: T. Chandra and T. Sakai, Thermec'97, Wollongong, Australia: The MM&M Society: 1997. p.147.

[9] M.R. Toroghinezhad, A.O. Humphreys, F. Ashrafizadeh, A. Najafizadeh and J.J. Jonas. In: T. Sakai, Processing and Manufacturing of Advanced Materials, Spain: Trans Tech Publications: 2003. p.3691.

[10] R.K. Ray and A. Haldar. Materials and Manufacturing Processes 2002;17:715.

[11] M.R. Barnett. Materials Technology 2000;71:295-303.

[12] R.K. Ray, J.J. Jonas and R.E. Hook. Int. Mat. Rev. 1994;39:129-172.

[13] A.O. Humphreys, D. Liu, M.R. Toroghinezhad and J.J. Jonas. ISIJ International 2002;42:52-56.

[14] M.R. Toroghinezhad, A.O. Humphreys, E. Essadiqi, F. Ashrafizadeh, A. Najafizadeh and J.J. Jonas. ISIJ International 2003;43:1842.

[15] R.D. Doherty, D.A. Hughes, F.J. Humphreys, J.J. Jonas, D.J. Jensen, M.E. Kassner, W.E. King, et al. Materials Science and Engineering A 1997;238:219-274.

[16] R.D. Doherty, G. Gottstein, J.R. Hirsch, W.B. Hutchinson, K. Lucke, E. Nes and P.J. Wilbrandt. In: J.S. Kallend and G. Gottstein, ICOTOM 8, Warrendale, PA: TMS: 1988. p.369.

[17] F.J. Humphreys. Acta Materialia 1997;45:5031-5039.

[18] K. Verbeken and L. Kestens. Acta Materialia 2003;51:1679-1690.

[19] K. Verbeken, L. Kestens and J.J. Jonas. Scripta Materialia 2003;48:1457-1462.

[20] L. Kestens and J.J. Jonas. Metals and Materials 1999;5:419.

[21] J.L. Bocos, E. Novillo, M.P. Ma, A. Iza-Mendia and I. Gutierrez. Materials Science Forum 2003;426-432:3581.

[22] M.R. Barnett and L. Kestens. ISIJ International 1999;39:923-930.

[23] M.Z. Quadir and B.J. Duggan. Acta Materialia 2004;52:4011-4021.

[24] P.S. Bate and J. Quinta da Fonseca. Materials Science and Engineering A 2004;380:365-377.

[25] W.B. Hutchinson and D. Artymowicz. ISIJ International 2001;41:533.

[26] V. Randle and O. Engler. 2000;385.

[27] H.J. Bunge. Texture Analysis in Materials Science, Academic-Verlag, First, 1982. p.590.

[28] W.T. Lankford, S.C. Snyder and J.A. Bauscher. Trans ASM 1950;42:1197.

[29] ASTM. Standard Test Method for Plastic Strain Ratio r for Sheet Metal, ASTM International, 2000. p.8.

[30] G.J. Davis. J. Sheffield University Metallurgical Society 1975;17.

[31] F. Emren, U.V. Schlippenbach and K. Lücke. Acta Metall. 1986;34:2105.

[32] K. Verbeken. Ph. D Thesis, Universiteit Gent 2004.

[33] B.D. Cullity. Elements of X-ray Diffraction, Addison-Wesley Publishing Company, INC., Second Edition, 1978. p.993.

[34] B.L. Adams. Ultramicroscopy 1997;67:11-17.

[35] J.-J. Fundenberger, A. Morawiec, E. Bouzy and J.S. Lecomte. Ultramicroscopy 2003;96:127-137.

[36] D.P. Field. Ultramicroscopy 1997;67:1-9.

[37] F. Wagner, N. Bozzolo, N. Dewobroto and N. Gey. Materials Science Forum 2002;408-412:143.

[38] F.J. Humphreys. Journal of Materials Science 2001;36:3833-3854.

[39] A.J. Heckler and W.G. Granzow. Metallurgical Transactions 1970;1:2089.

[40] S.R. Goodman. Metallurgical Transactions 1971;2:2051.

[41] W.B. Hutchinson. Int. Met. Rev. 1984;29:25.

[42] W.B. Hutchinson, K.-I. Nilsson and J. Hirsch. In: R. Pradman, Metallurgy of Vacuum-Degassed Steel Products, U.S.: TMS: 1990. p.109.

[43] A. Okamoto and M. Takahashi. In: 6th Int. Conf. Texture of Materials, Tokio, Japan, 1981. p.739.

[44] U.V. Schlippenbach, F. Emren and K. Lucke. Acta Metall. 1986;34:1289-1301.

[45] R.K. Ray, J.J. Jonas, M.P. Butron-Guillen and J. Savoie. ISIJ International 1994;34:927.

[46] M.P. Butrón-Guillen and J.J. Jonas. ISIJ International 1996;36:68-73.

[47] L. Kestens and Y. Houbaert. In: S. Yue and E. Es-sadiqi, J.J. Jonas Symposium, Thermomechanical Processing of Steel, Canada: Met Soc: 2000. p.411.

[48] M.R. Barnett and J.J. Jonas. ISIJ International 1997;37:697-705.

[49] M.R. Toroghinejad, A.O. Humphreys, D. Liu, F. Ashrafizadeh, A. Najafizadeh and J.J. Jonas. Metallurgical and Materials Transactions A 2003;34A:1163.

[50] R.E. Hook, A.J. Heckler and J.A. Elias. Metallurgical Transactions 1975;6A:1975.

[51] W.B. Hutchinson. In: Material Science Forum, Switzerland: Trans. Tech: 1994. p.1917.

[52] M.R. Barnett and J.J. Jonas. ISIJ International 1997;37:706-714.

[53] F.J. Humphreys and M. Hatherly. Recrystallization and Related Annealing Phenomena, Elsevier Science Ltd., Oxford, UK, 1996. p.173-220.

[54] M.R. Barnett. Ph.D. Thesis, McGill University 1996.

[55] M.R. Barnett, J.J. Jonas and P.D. Hodgson. Iron Steelmaker 1996;39-46.

[56] H. Inagaki. ISIJ International 1994;34:313.

[57] T. Haratani, W.B. Hutchinson, I.L. Dillamore and P. Bate. Metal Science 1984;18:57-65.

[58] L. Kestens, J.J. Jonas, P. Van Houtte and E. Aernoudt. In Situ Reactions for Synthesis of Composites, Ceramics, and Intermetallics; Metallurgical and Materials Transactions A: Physical Metallurgy and Materials Science 1996;27A:2347-2358.

[59] T. Urabe and J.J. Jonas. ISIJ International 1994;34:435.

[60] S.-H. Choi and Y.-S. Jin. Materials Science and Engineering A 2004;371:149-159.

[61] L. Kestens and J.J. Jonas. Metallurgical and Materials Transactions A 1996;27:155.

[62] K. Ushioda and W.B. Hutchinson. ISIJ International 1989;29:862.

[63] M.D. Nave and M.R. Barnett. Materials Science Forum 2002;408-412:907.

[64] J.J. Jonas. In: W. Bleck, Modern LC and ULC Sheet Steels for Cold Forming: Processing and Properties, Aachen: Verlag Mainz: 1998. p.73.

[65] M.R. Barnett. ISIJ International 1998;38:78-85.

[66] I.B. Timokhina, A.I. Nosenkov, A.O. Humphreys, J.J. Jonas and E.V. Pereloma. ISIJ International 2004;44:717.

[67] H. Hu. Trans. Metall. Soc. A.I.M.E. 1962;224:75.

[68] P.A. Beck and P.R. Sperry. J. Appl. Phys 1950;21:150.

[69] A. Bodin, J. Sietsma and S.V.D. Zwaag. Metallurgical and Materials Transactions A 2002;33A:1589-1603.

[70] S.W. Cheong, E.J. Hilinski and A.D. Rollett. Met. and Mat. Trans. 2003;34A:1311.

[71] D.N. Lee. Scripta Metallurgica et Materialia 1995;32:1689-1694.

[72] Y.B. Park, D.N. Lee and G. Gottstein. Acta Materialia 1998;46:3371-3379.

[73] Y. Hayakawa and J.A. Szpunar. Acta Materialia 1997;45:3721-3730.

[74] Y. Hayakawa and J.A. Szpunar. Acta Materialia 1997;45:1285-1295.

[75] Y.B. Park, L. Kestens and J.J. Jonas. In: T. Sakai and H.G. Susuki, Recrystallization and Related Phenomena, Japan: The Japan Institute of Metals: 1999. p.751.

[76] J.H. Choi, S.Y. Kang and D.N. Lee. J. Mat. Sci. 2000;35:4055.

[77] G. Glover and C.M. Sellars. Metallurgical Transactions 1972;3:2271-2281.

[78] R. El-Koussy and V.P. Polukhin. Journal of Mechanical Working Technology 1978;2:145-160.

[79] D.N. Hawkins and A.A. Shuttleworth. Journal of Mechanical Working Technology 1979;2:333.

[80] G.E. Dieter. "Mechanical Metallurgy", McGraw Hill, 3rd, 1988. p.751.

[81] M.R. Barnett and J.J. Jonas. ISIJ International 1999;39:856-873.

[82] L.K. Tung and B.J. Duggan. Materials Science Forum 2002;408-412:1221.

[83] J.-T. Park and J.A. Szpunar. Acta Materialia 2003;51:3037.

[84] J. Glen. J. Iron Steel Inst. 1957;

[85] S.L. Semiatin and J.J. Jonas. In: Formability and Workability of Metals-Plastic Instability and Flow Localization, Park, Ohio: ASM, Metals: 1984. p.43.

[86] G.H. Akbari, C.M. Sellars and J. Whiteman. Acta Materialia 1997;45:5047-5058.

[87] G.E. Liu and B.J. Duggan. Metallurgical and Materials Transactions A 2001;32A:125.

[88] I. Tsukatani. ISIJ International 1998;38:625.

[89] T. Senuma and N. Hashimoto. Textures and Microstructures 1997;30:97.

[90] N. Hashimoto, N. Yoshinaga and T. Senuma. ISIJ International 1998;38:617.

[91] K. Eloot, K. Okuda, K. Sakata and T. Obara. ISIJ International 1998;38:602.

[92] M.Z. Quadir and B.J. Duggan. Materials Science Forum 2002;408-412:1227.

[93] Y.Y. Tse. Materials Science Forum 2002;408-412:1233.

[94] A. Tomitz and R. Kaspar. Steel Research 2000;71:504.

[95] T. Senuma and K. Kawasaki. ISIJ International 1994;34:51.

[96] B.J. Duggan, K.T. Lam and M.Z. Quadir. In: T. Chandra, J.M. Torralba and T. Sakai, Thermec'2003, Spain: Transtech Publications: 2003. p.3745.

[97] A.S. Keh, Y. Nakada and W.C. Leslie. In: A.R. Rosenfield, Dislocation Dynamics, 1967. p.381.

[98] K. Ushioda, N. Yoshinaga and O. Akisue. ISIJ International 1994;34:85.

[99] R.F. Knight and G.P. Contractor. Journal of Metals 1971;23:45.

[100] B.H. Cao, J.J. Jonas, P.R. Hastings and N. Nickoletopoulos. Materials Science Forum 1998;284-286:543.

[101] N. Takahashi, M. Shibata, Y. Furuno, H. Hayakawa and K. Kakuta. In: R. Pradhman, Metallurgy of Countinuous Annealed Sheet Steel, TMS: 1982. p.133.

[102] J. Haga, N. Mitzui, T. Nagamichi and A. Okamoto. ISIJ International 1998;38:580.

[103] ASTM. Standard Test Methods for Determining Average Grain Size, ASTM International, 2000. p.22.

[104] A.O. Humphreys, D. Liu, M.R. Toroghinejad, E. Essadiqi and J.J. Jonas. Materials Science and Technology 2003;19:709.

[105] N.D. Romani. M.Eng. Thesis, McGill University 2003.

[106] M. Dahms and H.J. Bunge. J. Appl. Crystall. 1989;439.

[107] J.L. Bocos, E. Novillo, M.M. Petite, A. Iza-Mendia and I. Gutierrez. Metallurgical and Materials Transactions A 2003;34A:827.

[108] D.J. Jensen. Scripta Metallurgica et Materialia 1992;27:533-538.

[109] D.J. Jensen. Acta Metallurgica et Materialia 1995;43:4117-4129.

[110] H. Magnusson, D. Juul Jensen and W.B. Hutchinson. Scripta Materialia 2001;44:435-441.

[111] K.A. Taylor. Metallurgical Transactions A 1992;23A:107.

[112] M.R. Toroghinejad, A.O. Humphreys, F. Ashrafizadeh, A. Najafizadeh and J.J. Jonas. In: T. Chandra, J.M. Torralba and T. Sakai, THERMEC'2003, Madrid, Spain: Trans Tech publications: 2003. p.3691.

[113] Y. Hoshoda and Y. Nagataki. In: 37th MWSP Conf.Proc, U.S.: 1996. p.915.

[114] G. Glover and C.M. Sellars. Metallurgical Transactions 1973;4:765-776.

[115] G.H. Akbari, C.M. Sellars and J.A. Whiteman. Materials Science and Technology 2000;16:47-54.

[116] T. Sakai, Y. Saito and K. Kato. Trans. ISIJ 1988;28:1036-1042.

[117] B.J. Duggan, Y.Y. Tse, H. Ning and M.Z. Quadir. Materials Science Forum 2002;408-412:1151.

[118] G. Ibe and K. Lücke. Archiv für das Eisenhüttenwesen 1968;39:693.

[119] K. Verbeken, L. Kestens and M.D. Nave. Acta Materialia 2005;53:2675.

[120] ASTM. Standard Test Method for Tension Testing of Metallic Materials [Metric], ASTM International, 2001. p.8.

APPENDIX

A. Correlation between calculated and measured r-values.

The accuracy of the r-values calculated on the basis of the texture data using the relaxed constraint method of crystal plasticity affects the reliability of the final conclusions. R-values were therefore measured experimentally using tensile tests. These values were then compared with the predictions to establish the level of confidence in the latter.

Tensile specimens were machined from the steel sheet following ASTM standard E8M-01 [120], with their longitudinal axes inclined at 0, 45 and 90 degrees to the rolling direction. After full annealing, the specimens were pulled to a strain of 16%, then unloaded. Each r-value was calculated according to ASTM standard E 517-00 [29].

The r-value was calculated as follows:

$$r = \frac{\varepsilon_W}{\varepsilon_T} \qquad 1)$$

where the subscripts W and T refer to the width and thickness, respectively, $\varepsilon_W = \ln(W_f/W_o)$, and $\varepsilon_T = \ln(T_f/T_o)$. Assuming that the volume remains constant:

$$\varepsilon_T = \ln(L_o W_o / L_f W_f) \qquad 2)$$

Then r is calculated as:

$$r = \frac{\ln(W_o/W_f)}{\ln(L_f W_f / L_o W_o)} \qquad 3)$$

Finally, the mean r-value or normal anisotropy is obtained as follows:

$$r_m = (r_0 + 2r_{45} + r_{90})/4 \qquad 4)$$

Additionally, the earing tendency or planar anisotropy was determined as:

$$\Delta r = (r_0 + r_{90} - 2r_{45})/2 \qquad 5)$$

The measurements were carried out on samples prepared by the 3 different processing conditions, with 3 samples cut for each direction, 0, 45 and 90°, for each sample. This led to a total of 27 samples. The results from one of these conditions were further compared with those from an additional set of samples. The measured values and those calculated for the three experimental conditions by the relaxed constraint method are presented in Figure A.1.

The good correlation evident between the two procedures indicates that the calculation of r-values is reliable.

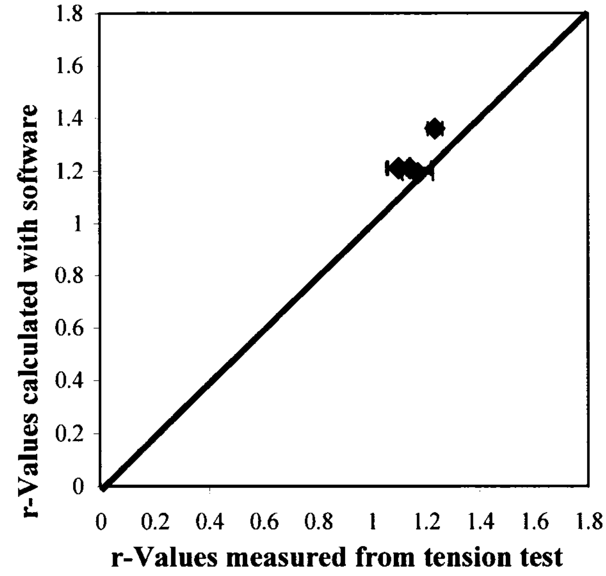

Figure A.1. Correlation between measured and calculated r-values.